Master thesis and internship[BR]- Master's thesis : Detection analysis of a Mid-Wave InfraRed camera for small satellite missions.[BR]- Integration Internship

Auteur : Barros Farres, Oriol
Promoteur(s) : Habraken, Serge
Faculté : Faculté des Sciences appliquées
Diplôme : Cours supplémentaires destinés aux étudiants d'échange (Erasmus, ...)
Année académique : 2020-2021
URI/URL : http://hdl.handle.net/2268.2/11322

Master's degree Aerospace engineering
Academic Year 2020-2021

Master's thesis carried out to obtain the degree of Master of Science in Aerospace Engineering

Detection analysis of a Mid-Wave InfraRed camera for small satellite missions

Author: **Oriol Barros Farrés**

Academic Advisor:
Serge Habraken
Assistant:
Jesús Vilaboa Pérez

University of Liège - School of Engineering and Computer Science

June 2021

[This page intentionally left blank.]

Abstract

The Mid-Wave Infrared is a region in the infrared spectrum, which has not been deeply in use in satellite development, in part because the Long-Wave Infrared offers at first appearance a wider range of applications and performance. Therefore, the extense of LWIR leaves a big gap in which a MWIR detector can be useful and gather information the other infrared spectrums can not.Furthermore, high spatial resolution applications in spacecraft missions in the thermal infrared have not been exploited too much, especially in nanosatellites.

What this means is as already stated that there are a lot of situations which a MWIR can cover, just as, for example, high temperature applications such as volcanos or wildfires. Additionally, it offers a better performance in thermal resolution. The purpose of this Thesis is to discuss and trade-off in which situations and for which characteristics, it is a feasible nanosatellite mission in the MWIR. It will be studied also which detector in the market is more suitable depending on the requirements for each mission scenario, computing key values such as the temperature resolution, size, and signal-to-noise ratio.

Keywords: MWIR, Photon detector, Thermal detector, CubeSat, SNR, NETD.

Acknowledgements

First of all, I want to thank Prof. Serge Habraken for the unique opportunity to carry out my Master Thesis with the Centre Spatial de Liège and discover a topic which I was not very familiar with but that I found that is very interesting. I am really thankful for all the dedication and support I have received during these months from Prof. Serge Habraken and especially from Jesús Vilaboa whose advice were always very useful and because he helped me every time I needed it.

I am grateful also for all people who have carried me during the Master's Degree and during these last months in Belgium during my Erasmus exchange. Thanks to Alvaro, who has given me a hand whenever I had some technical issues. Finally, to my family and Lidia, to whom I owe my most deep gratitude for supporting me every time I failed or I got lost.

Contents

List of Figures

List of Tables

List of Acronyms

ADCS Attitude Determination and Control System.

AMS Agricultural Monitoring Satellite.

CCD Charged-Coupled Device.

CERES Clouds and the Earth's Radiant Energy System.

CIRAS CubeSat Infrared Atmospheric Sounder.

CMOS Complementary Metal-Oxide-Semiconductor.

ECOSTRESS ECOsystem Spaceborne Thermal Radiometer Experiment on Space Station.

EFL Effective Focal Length.

EMI Ernst-Mach-Institut.

EOS Earth Observing System.

ERNST Experimental Spacecraft based on Nanosatellite Technology.

ERSIS European Remote Sensing Information Service.

FoV Field of View.

FPA Focal Plane Array.

FPGA Field-Programmable Gate Array.

GSD Ground Sample Distance.

HOT-BIRD High Operating Temperature Barrier Infrared Detector.

IDCA Integrated Dewar Cooler Assembly.

iFoV Instantaneous Field of View.

IGBP International Geosphere Biosphere Programme.

INMS Ion and Neutral Mass Spectrometer.

IR InfraRed.

LSTM Land Surface Temperature Monitoring.

LunIR Lunar InfraRed Imaging.

MISTIGRI Micro Satellite for Thermal Infrared Ground Surface Imaging.

MPT Micro Pulse Tube.

MWIR Mid-Wave InfraRed.

NASA National Aeronautics and Space Administration.

NEP Noise Equivalent Power.

NETD Noise Equivalent Temperature Difference.

QW Quantum Well.

ROIC Read-Out Integrated Circuits.

SNR Signal-To-Noise Ratio.

SWIR Short-Wave InfraRed.

T2SL Type II Superlattice.

TDI Time Delay Integration.

TUM Technische Universität München.

UV UltraViolet.

VLWIR Very Long-Wave InfraRed.

VNIR Very-Near InfraRed.

1 Introduction

Nowadays the satellite development for high and medium spatial resolution for thermal infrared bands is not much advanced. Aside from the Copernicus Land Surface Temperature Monitoring (LSTM), which will provide very accurate land temperature mapping thanks to a LWIR (8-12.5 μm) device coupled with VNIR and SWIR bands. LSTM may be the only source of this type of imaging for the entire 2020's.
Furthermore, apart from being the only satellite with those characteristics, the LSTM leaves uncovered some high temperature events like volcanos and wildfires. The concept of this project should be to provide for a group of MWIR detectors that could detect and map those type of events.

1.1 Why MWIR?

The MWIR measurements offer several advantages. First of all, the contrast for the power variation in function of the changes of temperature, for the MWIR the contrast is higher when comparing with the LWIR band. So as mentioned previously it should be useful to observe targets which are very hot such as volcanos or wildfires, when sensitivity is not as important as contrast.
The MWIR signal is also composed by reflected light and thermal emissive signal, this means that it can be used during the night when it is easy to detect the thermal emissive signal and during the day to obtain the reflected light. It is less subject to diffraction, it requires less cooling than LWIR band and is less disturbed by the radiation of its own instrument.
The efficiency of the MWIR band is better in atmospheric conditions in which the humidity is high, thus the transmission of the MWIR when there is a high percentage of humidity is better. So as seen it could provide an improvement for some scene characteristics and have some very interesting applications that could be used in a satellite mission.

1.2 Objectives of the project

The main goal of the project is to propose a scientific instrument on board a prototype satellite -in-orbit demonstration mission, with the final goal to prove that the technology can be useful in a future constellation.

To do that there will be meet some requirements of the mission:

- Daily revisit.
- MWIR with at least two channels.
- GSD of at least 20 m, target 10 m.
- Δ T better than 2 K.
- Absolute temperature accuracy of 5 K.

To do so, there is a proposed a series of secondary objectives which will lead to the final goal of the project:

- Compare and study the performance of the MWIR detectors on the market.
- Cooled detector vs uncooled detector, advantages and disadvantages.

- Search of the best suitable MWIR detector for three proposed space applications, Crop Humidity Monitoring, Wildfire tracking and Maritime Vessel Tracking.
- How to fit the better choice in a satellite mission and related interfaces. Thermal and power requirements, response time, noise and on-board processing.

2 Mid-Wave Infrared Physics & Figures of Merit

2.1 Introduction

In this section it will be carried out a review of the infrared detector in the Mid-Wave range. Definitions, characteristics, and technologies oriented to space applications. The objective will be to establish which type of Mid-Wave Infrared Detector is suitable for which type of space application.

2.2 Infrared spectrum

The infrared is a region of electromagnetic radiation which its wavelength is longer than the one in the visible spectrum, so it can not be seen by the human eye [1]. It encompass a wavelength range of approximately 700 nm to 1 mm. Infrared radiation has multiple applications which include industrial, medical, scientific, military, and commercial. It is used in astronomy as it is included to penetrate molecular clouds, detect planets, and view red-shifted objects. It is interesting to divide the infrared spectrum as sometimes detectors collect radiation within a specific bandwidth.Thus, it is divided into smaller sections depending on how it is employed. The scheme which is going to be used is the one regarding the response of various detectors:

Band	**Wavelength**
Near-infrared (NIR)	0.7-1 μm
Short-wavelength infrared (SWIR)	1–3 μm
Mid-wavelength infrared (MWIR)	3–5 μm
Long-wavelength infrared (LWIR)	8–12 μm
Very Long-wavelength infrared (VLWIR)	12-30 μ m

Table 2.1 – Infrared wavelengths bands [1].

This wavelength division is also motivated because the atmosphere is transparent or opaque to certain bands, due to the atmospheric transmittance in the infrared region, which is shown in the next figure:

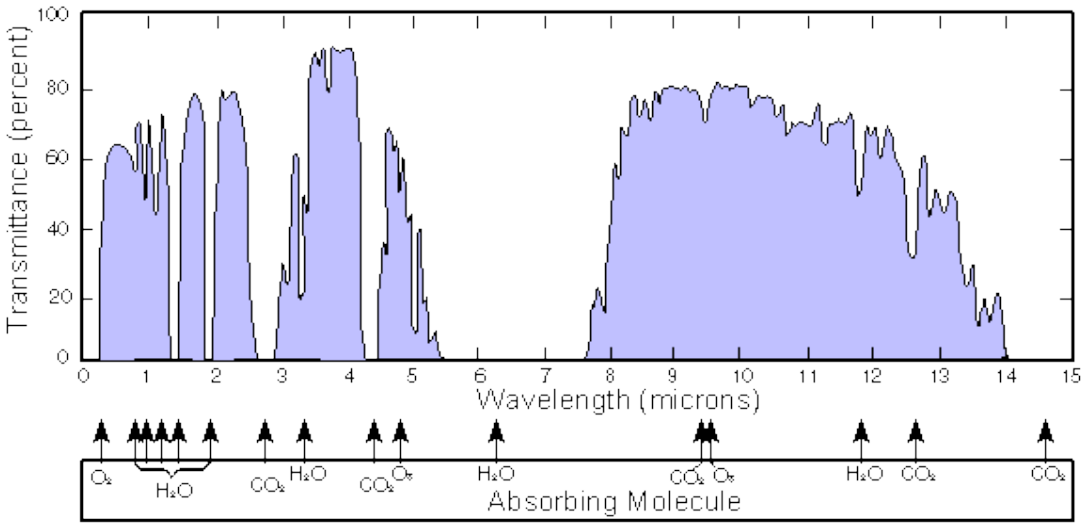

Figure 2.1 – Atmospheric transmittance.

This thesis is going to be centered around the Mid-wavelength infrared from 3-5 μm and it would be discussed its advantages and limitations throughout the further sections.

2.3 Infrared optics

Is necessary to understand that to capture the infrared radiation is used a system of lenses and mirrors, so it is mandatory to mention some of the optical concepts attached to it. First of all, the main parameters to describe an optical instrument which are the focal length, f and the diameter of entrance pupil, D_p . The focal length is the distance from the lens to the point in which the light is focused, which is called focal point. The diameter of entrance pupil is the diameter of the physical aperture stop as seen from the lens. The ratio between these two parameters is a very important one and is known as the f-number, $f/\#$, defined as:

$$f/\# = \frac{f}{D_p} \tag{2.1}$$

It is an important parameter because it defines the resolution limit of a system due to optics [10]. The other limiting factor is the diffraction limit, because infinite resolution is impossible to achieve even with perfect optics. The wave light properties limit resolution, the diffraction limit spot size is defined through the f-number and the wavelength of the electromagnetic spectrum observed. It is defined as it follows:

$$D_l = 2.44\frac{f \cdot \lambda}{D_p} = 2.44 \cdot f/\# \cdot \lambda \tag{2.2}$$

The pixel size is defined by the pixel pitch of the detector. Usually, pixels for infrared detectors are of the order of micrometres. Although the fill factor is introduced to define which percentage of the pixel area is sensitive to infrared radiation and thus participates in the conversion of photons into electrons. Furthermore, the number of pixels will also define the resolution of the final image. However, not always having a higher number of pixels is the better choice as the SNR depends on the pixel size , which is also necessary to be taken into consideration when considering a detector.

The term Field of View (FoV) is also an important concept in remote sensing, as it defines the solid angle through which a detector is sensible to the radiation, in this case the infrared. As it is for just one pixel detector, it is specified as Instantaneous Field of View (iFoV) when applied for the full sensor width is the full or the real FoV. This term is very closed related to another concept, the Ground Sampling Distance (GSD), the GSD is a measure of spatial resolution and is the distance between pixel centers in a digital photo taken from the space. The FoV depends on the GSD, the altitude of the satellite h, the effective focal length f and the pixel size ps, all related to the next equation and figure:

$$tan(FoV) = \frac{GSD}{h} = \frac{ps}{f} \tag{2.3}$$

The GSD is a pivotal parameter to plan a remote sensing satellite mission. For example, if the GSD is fixed because the mission requirements need to, a change in the altitude would translate into a change of the focal length or pixel size. Therefore, it is crucial to choose a specific detector, optics or mission orbit. The GSD also establishes the minimal area the detector can differentiate from the ground as each pixel [10] [9] will be associated with that area, which is the square root of the ground sampling distance.

In Figure 2.2 it is possible to observe all this term previously mentioned and another one, the swath width, which is the result from the product of the pixel width of the detector and

the GSD. This concept is closely related to the revisit time of the satellite as a larger swath could reduce the revisit time or the number of satellites of a constellation as a larger surface is observed in every orbit cycle.

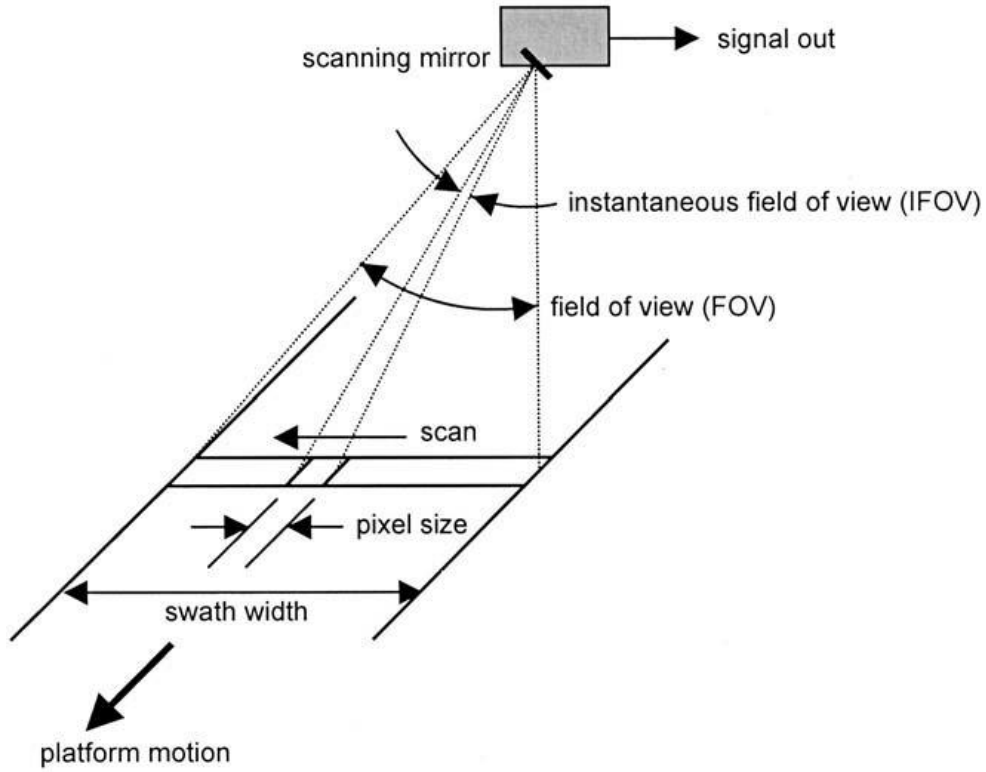

Figure 2.2 – The schematic representation of the field of view and the swath width [13].

Finally, another important parameter in optics is the effective focal length (EFL), which is a measure of how strongly the optics converge or diverge the incident radiation and as mentioned earlier, it is the key to compute the spatial resolution obtained, the formula for the effective focal length can be written as:

$$f = \varnothing_{aperture} \cdot F_{/\#} \tag{2.4}$$

Where $\varnothing_{aperture}$ is the maximum clear aperture of the optics and $F_{/\#}$ is the f-number.

2.4 Infrared detector

A detector or sensor is a device that responds to some stimulus coming from an event in the surrounding environment and in particular . This input proceeds from a physical change and in particular for an infrared detector it comes from optical and electrical signals that can be measured and quantified.

The purpose of an infrared detector is to capture the radiation in the infrared range from a target and to convert this radiation into an image or a description of what is the system observing.

For infrared optics, an image will be formed with the thermal heat radiation that the detector receives from the infrared spectrum detected. Thus, it will reflect in an image about the temperature differences of the target.

The detector as it is located in the focal plane of the optical system is possible to refer to it as the Focal Plane Array (FPA). This could be one of the main parts of the detector, the other one being the readout system, since it is necessary to convert the signal into an electrical signal that can be measured and treated. Both parts used to have a chip for each action but nowadays are all integrated in the read-out integrated circuit (ROIC) [2].

The FPA is an image sensor consisting of an array, as it name indicates, which is composed by pixels which collect the incident radiation and is situated also as it name indicates at the focal plane of the lens. There exists two main types of architecture to convert photons into electrons and these into current/voltage output. The first one, the Charge-Coupled Device (CCD) architecture, converts photons into electrons within each pixel in the FPA. On the other hand, Complementary Metal-Oxide-Semiconductor (CMOS) architecture converts photons into electrons and these into voltage within each pixel, instead of the CCD that converts all electrons in the array into voltage.

The possible classification of infrared detectors can depend on how the thermal image is formed, the material of the sensitive element, the infrared wavelength in which is operating, or the circuit used for processing the signal [2].

2.5 Detector figures of merit

As it is difficult to characterize the performance of IR detectors due to the substantial number of variables involved, the following parameters are the ones that provide a comparison between detectors easily.

2.5.1 Responsivity

The responsivity is the ratio between the electrical output signal per unit of the input radiation power. The units are volts per watt (V/W) or amperes per watt (A/W), as it can be defined as the voltage or current responsivity, the voltage responsivity is as it follows [3]:

$$R_V = \frac{V}{P \cdot A} \tag{2.5}$$

The current responsivity has an analogous definition, replacing the voltage by the current intensity. From the equation, the electrical signal V is expressed in volts [V], P is the incident radiation energy per area [W/m^2] and A is the pixel active area [m^2]. The active area is calculated as the product of the pixel pitch horizontal times the pixel pitch vertical times the fill factor, which is the percentage of each pixel sensitive to the light.

When the responsivity is defined in function of the wavelength of the incident radiation is also known as the spectral responsivity [3] [5]. The optimal situation is that the spectral response is maximum in the wavelength range studied and has no response outside this range.

For the photodetectors, the spectral responsivity can be expressed in the following way [5]:

$$R_\lambda = \frac{\eta q \lambda}{h \cdot c} = \frac{\eta \lambda}{1.24} \tag{2.6}$$

Where η is the quantum efficiency [%], q is the electron elementary charge [C, coulombs], λ is the wavelength [m], h is the Planck's constant [J·s] and c is the speed of light in the vacuum [m/s].

This parameter does not depend on the altitude, as it may depend on the wavelength but

not on the incident radiation received. This characteristic should be useful later on to compute some other parameters in space as this one should remain constant.

2.5.2 Cut-off wavelength

There exists a limit wavelength in which the spectral responsivity stops increasing with the wavelength, this wavelength is called cut-off wavelength. Thus, photons with a larger wavelength are not absorbed by the detector materials, so they are not detected. This value can be obtained depending on the material energy gap as in equation 2.7 [5]:

$$\lambda_{cutoff} = \frac{h \cdot c}{\epsilon_{gap}} \tag{2.7}$$

Where h is the Planck's constant in [J·s], c is the speed of light in vacuum [m/s] and ϵ_{gap} is the energy gap in [eV]. It can be observed easily that cut-off wavelength and the energy gap are directly related.

$$\lambda_{cutoff} = \frac{1.24}{\epsilon_{gap}} \tag{2.8}$$

This parameter is crucial as the best performance of the detector is found near the cut-off wavelength because the photons in the cut-off wavelength have an energy equal to the energy gap [3]. Furthermore, when a manufacturer indicates a wavelength range of a photodetector, the superior limit of the range is usually the cut-off wavelength.

2.5.3 Noise Equivalent Power

The noise equivalent power (NEP) is the incident power on the detector signal output equal to the rms noise output. It can also be defined as the signal level that produces a signal-to-noise ratio of 1. Written in terms of responsivity [2]:

$$NEP = \frac{V_n}{R_v} = \frac{I_n}{R_i} \tag{2.9}$$

Where V_n and I_n are the values of current and voltage for the noise and R is the responsivity, it is expressed in [W/Hz$^{1/2}$].

2.5.4 Detectivity

The definition of detectivity is the inverse or reciprocal of the NEP and it is expressed as [2]:

$$D = \frac{1}{NEP} \tag{2.10}$$

The units are [Hz$^{1/2}$/W].

2.5.5 Specific detectivity

It was found although that for many detectors the NEP is proportional to the square root of the detector signal, thus is proportional to the detector area. NEP and detectivity depend on the bandwidth and detector area, so an additional parameter, the specific detectivity, was defined as [2]:

$$D^* = D(A_d \Delta f)^{1/2} = \frac{(A_d \Delta f)^{1/2}}{NEP} \tag{2.11}$$

Where A_d is the active area of a pixel [cm^2], Δf is the frequency bandwidth in [Hz]. The unit of D^* is [cm·Hz$^{1/2}$/W], the unit, also called Jones, to honor the introducer of the concept. Is a figure of merit which is important because it allows to compare detector performance of the same type but with different areas.

An equivalent expression is found next [2]:

$$D^* = \frac{(A_d \Delta f)^{1/2}}{P} SNR \tag{2.12}$$

Along with the responsivity is a very useful parameter because it does not depend on the altitude, so that a detector in the same conditions of temperature and studied in the same range of wavelength should have the same value of specific detectivity in the ground or in space. Therefore, an increase in SNR should not modify the value of the specific detectivity as it is directly linked with an increase in the incident energy, it reflexes on equation 2.12, same increase in these parameters leaves the same value for the specific detectivity.

As large the specific detectivity is, better is the performance of the detector, as the same way it occurs with responsivity, it increases with wavelength until it is limited by the cut-off wavelength of the detector material. Which at the same time is the optimum operation wavelength and the largest value of SNR. Thus, manufacturers usually provide of D^* peak to calculate the specific detectivity for each wavelength:

$$D^*(\lambda) = D^*_{peak} \frac{\lambda}{\lambda_{cutoff}} \tag{2.13}$$

2.5.6 Quantum efficiency

This figure of merit defines the efficiency of a detector transforming the incident photons into electrons (photocarriers). As it is an efficiency parameter, the highest value is the most desirable one, although it depends largely on the range of the wavelength. It can be expressed as [5]:

$$\eta = \frac{h \cdot c}{q} \cdot \frac{R_i}{\lambda} = 1.24 \frac{R_i}{\lambda} \tag{2.14}$$

Where R_i is the current responsivity of the photodetector in [A/W], h is the Planck's constant in [J·s], c is the speed of light in vacuum [m/s], q is the electron elementary charge in [C, coulombs] and λ is the wavelength.

It is necessary to state that is a concept only applicable for the photodetectors because for thermal detectors the conversion to electrons is not carried out the same way. Moreover, to maximize the quantum efficiency of the different photodetectors, it is necessary to increase the absorption coefficient and reduce as much as possible the reflection in the detector front area or increase the reflection on the back side of the detector [3] [9]. In Figure 2.3 it can be observed that different quantum efficiencies depending on the category of the photodetector and the wavelength and as mentioned before, it depends a lot on the range of the wavelength studied:

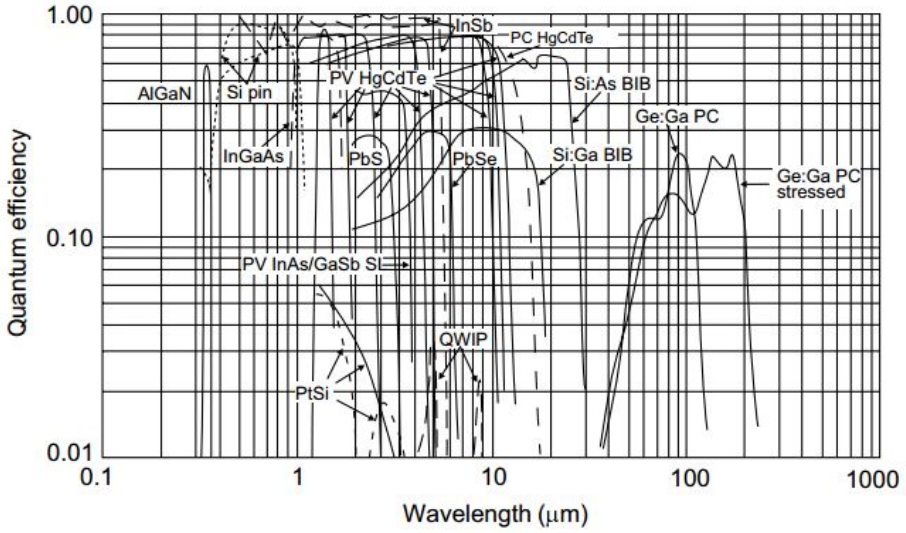

Figure 2.3 – Comparison of quantum efficiency vs the wavelength for different types of photodetectors [2].

This efficiency will be later discussed when different categories of photodetectors will be introduced.

2.6 Signal-to-Noise Ratio

The signal-to-noise ratio is defined as the ratio between the signal received from a target and the total noise produced by the detector. Is a fundamental figure to characterize the performance of a detector. The signal is the power in [W] received from the target, the responsivity of voltage/current has to be multiplied by this power to obtain the definition for an optical system. Therefore, SNR can be defined as in the next Equation 2.15 [5]:

$$SNR = \frac{P \cdot R}{V_n} \tag{2.15}$$

Where the value P of the incoming power [W] is calculated through the Plancks law of a black body, the responsivity [V/W] is intrinsic for the detector and V_n is the total noise of the detector [V]. The value of SNR can be calculated analogously to the current parameters and is adimensional. The noise contribution comes from different sources depending on the type of detector, this will be further discussed.

The Plancks law for the radiation of a black body is a integration over a desired wavelength. Previously, although it must be multiplied by the etendue of the optics, which is a parameter to describe how "spread out" is the radiation is in area and angle. Thus is the pixel active area of the detector times the solid angle of the optics. The solid angle in steradians [str], which is the angle in 3D, is a cone that the radiation forms between the target and the pixel. It depends on the f-number of the optics [10]. Thus, the etendue and the incident power can be described as [9]:

$$dG = ps^2 \cdot f_f \cdot \frac{\pi}{4 \cdot F\#} \tag{2.16}$$

$$P(\lambda, T) = \int_{\lambda_0}^{\lambda} \frac{2hc^2}{\lambda^5 (e^{\frac{hc}{\lambda kT}} - 1)} \cdot dG \tag{2.17}$$

2.7 Noise Equivalent Temperature Difference

The noise equivalent temperature difference (NETD), it is a concept that is used to quantify the temperature resolution, as it marks the minimum change in the temperature that the detector can notice. This change in temperature makes an output signal of the same value of the noise produced by the current, so the change in temperature should be larger to be able to detect it. To compute it, it is used as an alternative equation to calculate the detectivity [2] [9]:

$$D = \frac{4 \cdot F_{/\#}^2}{NETD \cdot A_d \cdot \phi \cdot \pi \left(\frac{dP}{dT}\right)_{\lambda_1 - \lambda_2}} \rightarrow NETD = \frac{4 \cdot F_{/\#}^2}{D \cdot A_d \cdot \phi \cdot \pi \left(\frac{dP}{dT}\right)_{\lambda_1 - \lambda_2}} \tag{2.18}$$

Where D is the detectivity of the detector [m $\cdot$ Hz$^{1/2}$ /W], A_d is the active area of the pixel [m^2], ϕ is the transmission of the optics, $\frac{dP}{dT}$ is the radiant power of the black body for a specific range in temperature and in wavelength, $F_{/\#}$ is the f-number of the optics. If is wanted to be obtain the NETD in the space environment, the $\frac{dP}{dT}$ is Planck's law by the ground emissivity and by the atmosphere transmittance in the MWIR, then differentiate it with respect to the temperature and finally integrate it for the specified range of wavelength.

This value of the NETD is normally given by the manufacturer and the conditions in which the detector was tested to obtain the NETD from the ground. Knowing this is possible to compute the detectivity and as the detectivity does not change with altitude, it is possible to calculate the NETD in the space by computing the radiant power as stated above.

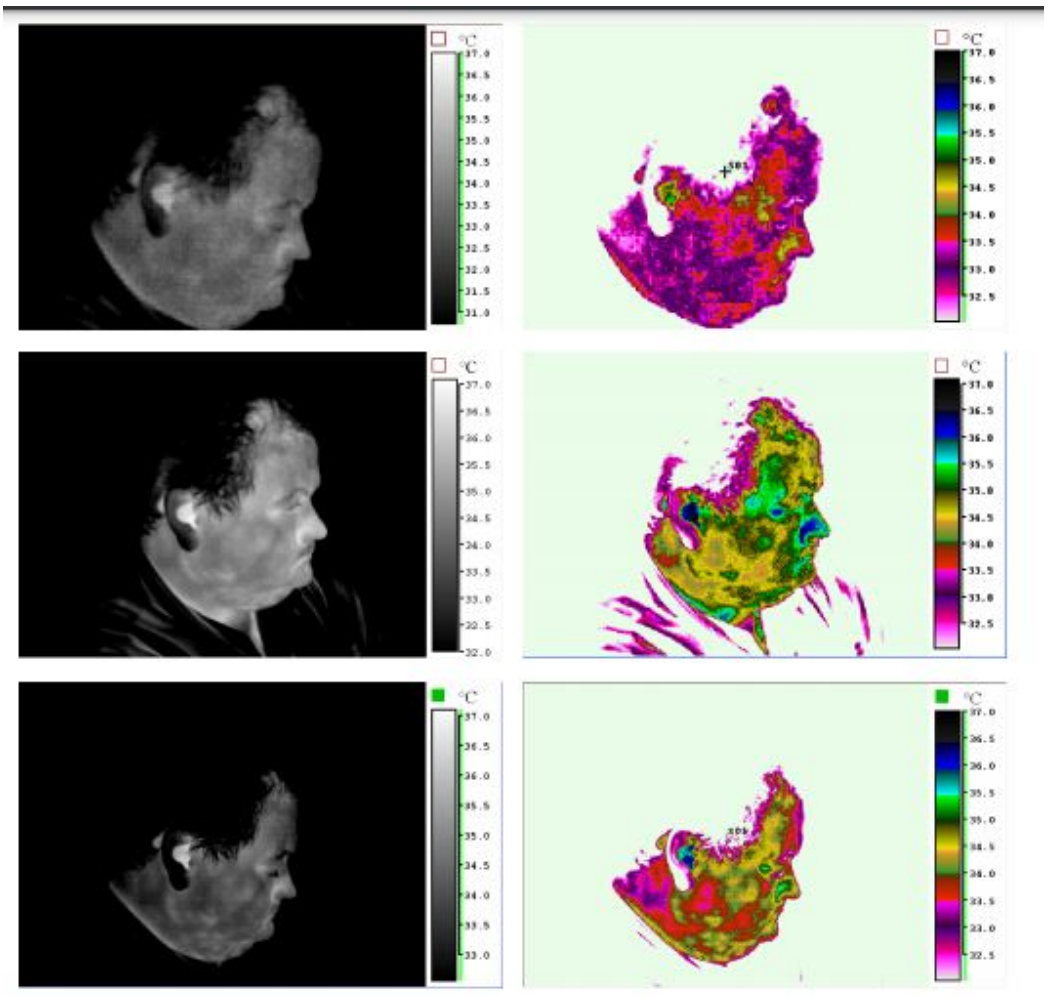

Figure 2.4 – Comparison of same element of interest with differnt values of NETD, at the top 100 mK, in the middle 70 mK, in the bottom 50 mK [48].

To realize the importance of the NETD is Figure 2.4, which compares three different cameras with different NETD, for the last image which is the one with more temperature resolution, it is possible to observe that the surface is smoother and more detailed. It is fundamental in low thermal contrast applications to be able to notice the changes in the ground temperature even if being very small.

2.8 Characteristic Times

There exist some characteristic times which are important to define the principle of working of a detector. As the satellite is traveling at a determined speed in space, the detector and its pixels need some time to collect the photons and finally the electronics need some time to convert the electrons into voltage or current. With this being said, next are presented some of the most relevant ones.

2.8.1 Integration time

The integration time is determined by the spatial resolution of the mission is fixed. This spatial resolution is defined by the already mentioned ground sampling distance (GSD) and it is calculated as the time the spacecraft needs to pass over the GSD distance. Therefore, the velocity of the spacecraft must be calculated to find the time needed, as it is obvious that it will depend on the altitude of the chosen orbit:

$$t_{int} = \frac{GSD}{v_{sat}} \tag{2.19}$$

For calculating the velocity of the satellite with respect to the ground, it can be used as the following equation:

$$v_{sat} = \frac{2\pi}{T_0} a - \omega_{earth} \cdot R_{earth} \tag{2.20}$$

Where a is the radius of the orbit in [km], ω_{earth} is the Earth angular velocity in [rad/s], R_{earth} is the Earth's radius in [km] and T_0 is the orbital period that can be calculated as:

$$T_0 = 2\pi\sqrt{\frac{a^3}{\mu}} \tag{2.21}$$

Where μ is the gravitational parameter of the Earth in [km^3/s^2].

2.8.2 Exposure time

The pixels must be exposed to the incident radiation to trap photons. Thus, the time the detector needs in order for the pixels to capture photons is referred to as exposure time. There must be some considerations taken to establish the exposure time and is related to the dynamic range. The dynamic range is then the maximum number of photons that the FPA can receive before saturation [11]. Therefore, it is desirable that the exposure time is shorter than the saturation time, because if not, there can exist some low quality images due to overexposure. Exposure time should be as close as possible to saturation but never surpass it. In addition, it can be adapted to obtain more photons where the situation is dark by having a longer exposure time or shortening it where the scene is very bright. The exposure time should not be longer than the integration time because it could be sensing photons from another GSD, hence the image will not be accurate.

2.8.3 Response time

The response time is a parameter that measures the interval of time, the increase in the detector output signal reaches the 63% of the maximum value after an input of radiation and the interval of time the decrease in the detector output signal decreases to 37% after the signal is switched off [3]. It must not be confused with the saturation time of the pixels, as the saturation time occurs when a pixel achieves an overexposure state when it can not integrate more photons.

This parameter exists both for thermal and photodetectors although it is calculated differently. It is deducible that the smallest value of this response time the better is for the performance of the detector as it will allow to process more signals in less time, being zero response time the ideal but unreachable value.

For the photodetectors the following equation is used to calculate the response time [5]:

$$|R| = \frac{v_0 \tau}{\sqrt{1 + (2\pi f \tau)^2}} \tag{2.22}$$

Where $|R|$ is the modulus of voltage responsivity in [V/W], v_0 is the initial value of the output signal in [V], f the frequency of the electronics of the detector in [Hz] and the response time τ in [s].
On the other hand, for the thermal detectors, the response time is obtained through the following expression [4]:

$$\tau_{thermal} = \frac{C_{th}}{g} \tag{2.23}$$

Where C_{th} is the thermal capacity of the material detector in [J/K] and g is the thermal conductivity of the material detector in [W/K].
The major difference of the response time between these two types of detectors is that meanwhile in photodetectors the time constant is very short and can be approximated as a step function, in the thermal detectors this function can be approximated as a exponential function. Furthermore, the values for a photodetector are of the order of microseconds and for the thermal detectors are between 5 and 15 ms [9].

Response time for thermal detectors is a crucial value because there is needed to have at least 95% of the signal to obtain an image which is not blurred. This 95% of the signal corresponds to three times the thermal time constant and thus this value must be equal to the exposure time, so for a 5 ms thermal time constant, the exposure time should be at least 15 ms or the image will be blurred. This could lead to a problem with low integration time, so some solutions will be defined to work around this problem.

2.8.4 Solutions for short response times

The integration time, apart from what is mentioned earlier, is composed by the exposure time plus the read-out time, which is the time that the photons captured by a pixel are converted into an electrical voltage or current. The sum of both the exposure time and the read-out time and it measures the number of observations the system can do for a given time, is measured in [Hz] or frames per second [fps] and it depends on each detector. The problem comes when, as already mentioned, the response time of the detector exceeds the total integration time of the satellite for a determined GSD, because it will be trapping the photons of the following GSD and thus the signal will be blurred.

In order to solve these problems, two approaches can be taken, the first one and more obvious is to install an active control of the spacecraft attitude to lengthen the integration time and let allow the detector to obtain and process the incident signal properly. For this, an attitude control and determination subsystem must be installed in the spacecraft, being the magnetorquers and the reaction wheel, apart from a sensor that enables the determination of the attitude. It may produce a disadvantage because the image taken from the scene would not be continuous but if the mission has only one point of interest is not a relevant problem. This approach is known as satellite slow down factor [6].

The second approach is a little more technical and is named Time Delay Integration (TDI). The technique consists in capturing the light from the same point of interest on different pixels. It is mainly used with a CCD architecture even though recently there have been developed CMOS with the capacity to do the TDI. Detectors that perform the TDI, what they do is scan the same scene with different rows. Then these different captures of the same scene are captured in different pixels and integrated to obtain a high resolution image [7].

The working principle of TDI is to have multiple rows, in Figure 2.5 is shown in an example of a 4 row TDI, in this case the first pixel from the first row captures the photons from the point of interest (t_1), the second pixel from the second row captures again the same point of interest and adds it up to the one obtained in the first row (t_2) and the process continues until the last row obtains the signal from the same point of interest.

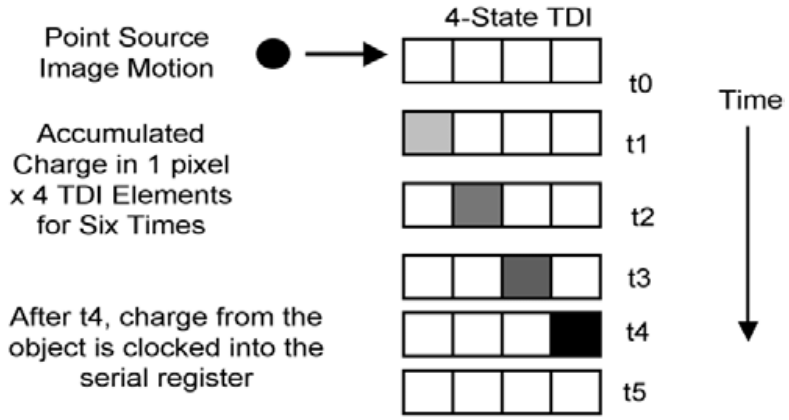

Figure 2.5 – Schematic of the TDI system work principle [12].

The exposure time of each pixel is individual, but read-out is done only once when all signals are obtained and added up. This technique is one of the main solutions to solve the problem for the microbolometers long response time. Although, the major disadvantage is that there is required very precise optics as each pixel of the row must capture the same point of interest as the previous and next pixel. This may be an issue in terms of spacecraft dimensions, especially in CubeSats, which may have greater restrictions in those terms as it also needs an attitude control and determination system.For instance, it has been only used in one operational mission for CubeSats AeroCube-11R3, which is a multi-band mission in which the TDI is done in the ground processing of the signal [15].

3 Mid-Wave Infrared Detectors

In this section, it will be explained how the technology of the MWIR detectors is nowadays, as well as which types of detectors have been more developed.

3.1 Classification of IR Detectors

The main classification, however, is done into two main categories: photon detectors and thermal detectors. The semiconductor IR detectors, the ones which have seen more progress, are included in the first class, the photon detectors. These detectors absorb radiation within the material by interaction with electrons. Spectral detectivity, a concept that will be discussed later on, of these detectors for a number of commercially available as shown in Figure 3.1, as it can be observed, is centered around two main atmospheric windows, one for the LWIR (8-14 μm) and the one for the MWIR (3-5 μm). Therefore, the spectral character of the photon detectors is influenced by the atmospheric transmittance, which as seen in section 2.2 in controls the range in which the IR spectrum may be used in the atmosphere.

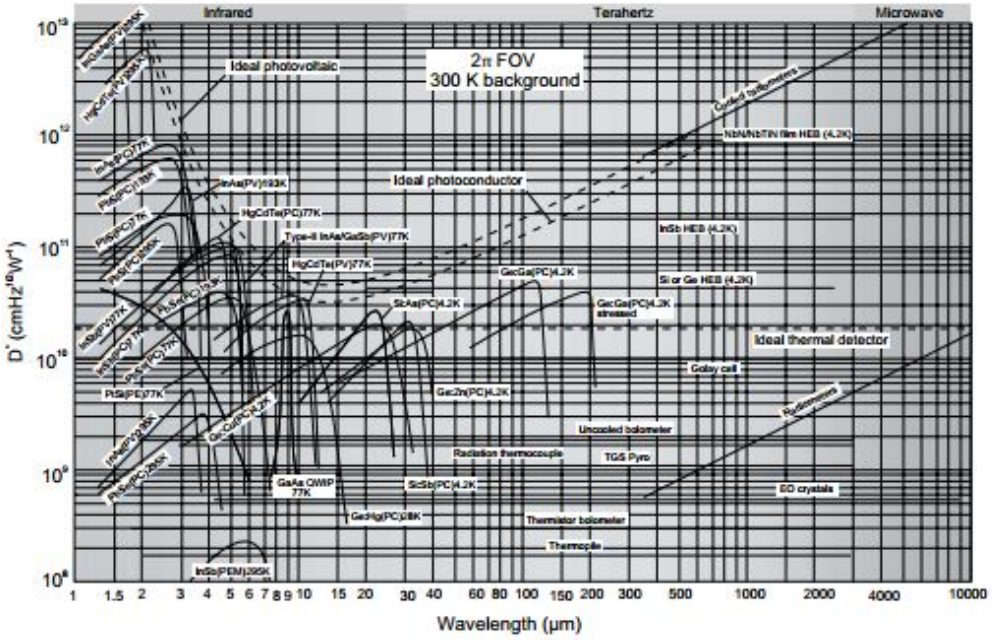

Figure 3.1 – Comparison of the spectral detectivity when operating at the indicated temperature and versus the wavelength [2].

The other class of detector is the thermal detectors. For these thermal detectors, the incident radiation is absorbed to change the material temperature and this temperature changes into another physical property change able to generate an electrical output. Three approaches of this type of detector have found to be most useful for IR technology, the bolometers, the pyroelectric, and the thermoelectric effects.

One of the main differences between both classes is that, on the one hand, although photon detectors may produce a perfect SNR performance and very fast response to achieve this, the photon detectors need cryogenic cooling. This cooling is necessary to prevent thermal generation from the charge carriers. On the other hand, thermal detectors do not need cooling systems as they operate at room temperature. They have a low sensitivity and slow response, because it requires a slow process to heat and cool the detector. However, they are cheap and easy to use. Thermal detectors are used in low-cost, which do not have a high speed and performance

requirement. Although they have not been as used as photon detectors, there is a trend in the past years to exploit this technology, as using large arrays of thermal detectors could achieve good values of temperature sensitivity.

Finally there is a third class which not so much impacts the radiation field detectors. Even though they had not much importance, it has gained some attention recently due to the wider application of harmonic mixers in the far-IR.

Here there is a summary table of all main classes of IR detectors and their advantages. Some of the types will be discussed later in further sections.

DETECTOR TYPE			ADVANTAGES	DISADVANTAGES
Thermal (thermopile, bolometers, pyroelectric)			Light, rugged, reliable, & low-cost Room temperature operation	Low detectivity at high frequency Slow response (ms order)
Photon	Intrinsic	IV–VI (PbS, PbSe, PbSnTe)	Easier to prepare More stable materials	Very high thermal expansion coefficient Large permittivity
		II–VI (HgCdTe)	Easy bandgap tailoring Well-developed theory & experience Multicolor detectors	Nonuniformity over large area High cost in growth and processing Surface instability
		III–V (InGaAs, InAs, InSb, InAsSb)	Good material & dopants Advanced technology Possible monolithic integration	Heteroepitaxy with large lattice mismatch Long wavelength cutoff limited to 7 μm (at 77 K)
	Extrinsic (Si:Ga, Si:As, Ge:Cu, Ge:Hg)		Very long wavelength operation Relatively simple technology	High thermal generation Extremely low-temperature operation
	Free carriers (PtSi, Pt_2Si, IrSi)		Low-cost, high yields Large & close packed 2-D arrays	Low quantum efficiency Low-temperature operation
	QWs	Type I (GaAs/AlGaAs, InGaAs/AlGaAs)	Matured material growth Good uniformity over a large area Multicolor detectors	High thermal generation Complicated design and growth
		Type II (InAs/GaSb, InAs/InAsSb)	Low Auger recombination rate Easy wavelength control Multicolor detectors	Complicated design and growth Sensitive to the interfaces
	QDs	InAs/GaAs, InGaAs/InGaP, Ge/Si	Normal incidence of light Low thermal generation	Complicated design and growth

Figure 3.2 – Comparison of the different IR detector types [2].

3.2 Photon detectors

One of the main categories, the photon detectors, the radiation received is absorbed within the material by interaction with electrons in three different ways, by bound lattice atoms, by bound to impurity atoms, or bound with free electrons. The observed electrical output signal is due to the change in the distribution of the electronic energy. There exist three main optical excitation processes in semiconductors which are [14]:

- Bulk semiconductors.
- Quantum wells.

- Type-II InAs/GaSb superlattices.

Another important feature to present is the relative response of the infrared detectors regarding power and photon flux:

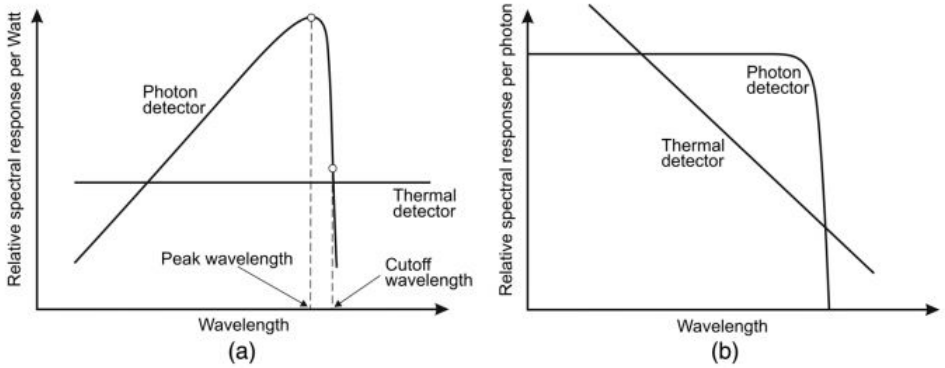

Figure 3.3 – Relative response for a photon and thermal detector for constant (a) incident radiant power and (b) photon flux [14].

As the figure shows, for photon detectors, the spectral response per watt varies theoretically linearly as a function of the wavelength, while on the other hand the spectral response per watt of thermal detectors is constant with the wavelength. For photon detectors, the limit of the curve is reached until the cutoff wavelength, which is determined by the detector material, as specified in the earlier section. For the thermal detectors, in the spectral response per photon, the trend changes as the energy per photon is inversely proportional to the wavelength . As for the photodetectors, it is relatively flat until it reaches the cutoff wavelength.

A further division inside the photon detectors can be made depending on the nature of the electron interaction as seen in Figure 3.2. The most important are extrinsic, intrinsic, photoemissive, and QW detectors. Moreover, it is important to highlight that each material detector can be used differently as photoconductive, photovoltaic, photoelectromagnetic, or photoemissive [14].

The most important difference between intrinsic and extrinsic detectors is that extrinsic detectors need much cooling in comparison with intrinsic detectors to achieve a high sensitivity at a given spectral response. Intrinsic detectors are most common at shorter wavelengths. In longer wavelength regions, the photoconductors are operated in an extrinsic mode, the major advantage of photoconductors is that they have a higher responsivity than photovoltaic detectors. Another important feature is the relation between the temperature of the background received by the detector and the lower temperature at which the detectors have to operate to achieve background-limited performance. From this relation it is possible to determine that [14]:

$$T\lambda_{cutoff} = constant \tag{3.1}$$

Therefore, the longer λ_{cutoff} is, the lower T becomes. This is possible because the quantities that determine the detector performance are exponential to the excitation energy. Then the detector temperature of operation can be approximated to:

$$T_{max} = \frac{300[K]}{\lambda_{cutoff}} \tag{3.2}$$

This trend can be observed in Figure 3.4, where they appear several high-performance detector materials which are suitable for low-background temperature: Si, InGaAs, InSb, T2SL, HgCdTe

photodiodes, Si:As BIB detectors and extrinsic Ge:Ga unstressed and stressed detectors. From these detectors, the ones that offer a lower operating temperature for the MWIR, such as the HgCdTe, the T2SL, and the InSb, will be the technology of some of the the detectors selected for further study to achieve the proposed values for the target mission.

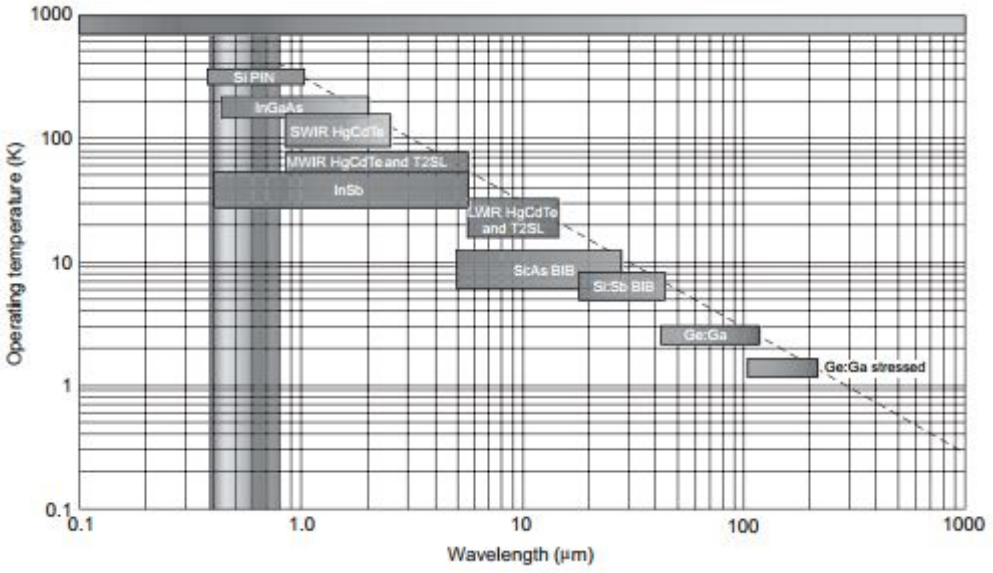

Figure 3.4 – Operating temperature vs wavelength for low-background materials. The dashed line is the trend described in Equation 3.2 [2].

Another relevant characteristic of photon detectors is the quantum efficiency, which is the efficiency of transforming photons into electrons. For intrinsic detectors like HgCdTe, InSb, and InGaAs, the quantum efficiency is really high over 70 %, meanwhile extrinsic detectors and specially the QWs detectors do not have a good value for quantum efficiency (see Figure 2.3).It is another reason why they may not be selected to study as they are not reliable.

3.3 Thermal detectors

The other main class of detector is the thermal detector. For the thermal detector, its principle of work is that the incident radiation is absorbed so that it changes the temperature of a chosen material, thus it changes also physically to generate an electrical output that can be measured. Hence, the thermal detector does not depend on the wavelength as the signal produced depends on the radiant power received rather than the spectral content of it (as seen in Figure 3.3). There are three main approaches to design the thermal detectors, bolometers, pyroelectric, and thermoelectric effects.

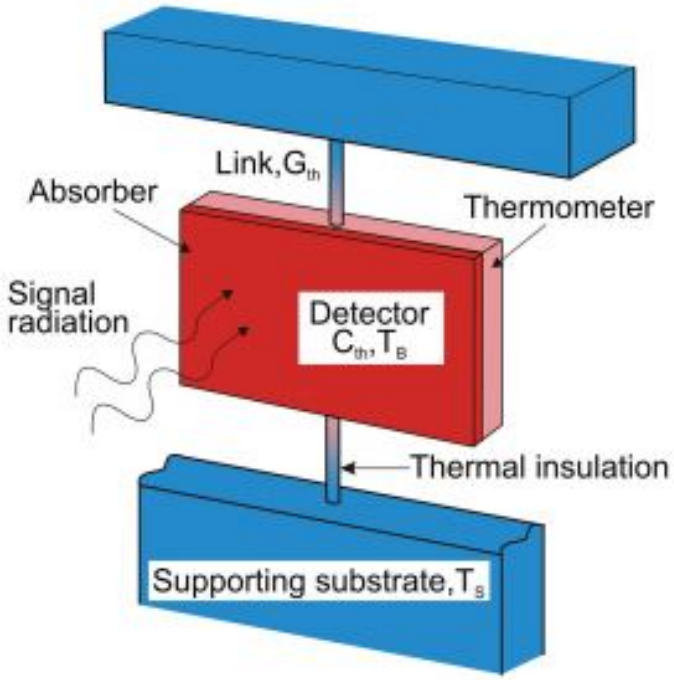

Figure 3.5 – Schematic diagram of the principle of operation of a thermal detector [14].

An example of a thermal detector designed by using thermoelectric effects is the thermopile, which is one of the oldest and consists of a series of thermocouples connected in series to achieve a better sensitivity. Thermopiles are based on the thermoelectric effect, generating a voltage when the thermocouples are exposed to a temperature difference. However, thermopile technology was not advanced enough so that they were ineffective, slow, and expensive devices, but with some developments in the field of semiconductors, thermopiles have been optimized [14].

In pyroelectric detectors a change in the electrical polarization is measured, meanwhile for bolometers the change measured is a change in the electrical resistance of the material. Usually a bolometer is a thin, blackened flake or slab, whose impedance is highly temperature dependent. Bolometers can be divided into several types. The most important ones are the metal and semiconductor bolometers. There exists another fourth type, superconductors not so widely used. They differ a lot in terms of the temperature dependence on resistance. Another advantage of bolometers is that they can be used in a wide spectral range of electromagnetic radiation and, for example, in the infrared can be used in MWIR as well as LWIR.

The most popular type of bolometer is the microbolometer and it is the most produced compared to other IR arrays. Nowadays, the VO_x microbolometer owns the biggest market share followed by Amorphous Silicon. This is due to the VO_x technology being older and thus more stable, sensitive, and compact than others. In addition, the most important feature of the microbolometer is that unlike other infrared detecting equipment, it does not need cooling.

3.4 List of detectors

Following the indications from the previous sections, there has been a selected group of detectors taking into account the availability in the market, as it is possible to observe that there has been chosen a variety of photon and thermal detectors of different technologies. These include HgCdTe, InSb, XBn, T2SL, and VO_x Microbolometer to test the most common and advanced technologies in the market. Another important point of choice was the f-number as well as the pixel size, the f-number was chosen as low as possible as one of the objectives is to be able

to collect as much radiation as possible, so the detectors with a low f-number tested were the ones chosen. For the pixel size, it was required a low pixel size which was compatible with the f-number to have a good ground spatial resolution. Another point of interest could be the detector operation temperature but is made with the assumption that the size is not a critical criteria, so it has been looked up for the temperature of operation but is not critical if it is required to be too low as it is assumed there is room for a cooler. Additionally, the detectors must have a size of FPA of at least 640x480 pixels.But above all, the detectors must work in the range of the MWIR, paying special attention to those detectors with several IR bands. Next are presented the list of detectors:

Manufacturer	**Detector Name**	**Material FPA**	**Wavelength range**
Lynred (France)	DAPHNIS-HD MW RM2/K563	HgCdTe	3.7 μm - 4.8 μm
AIM (Germany)	HiPIR-Engine HOT	HgCdTe	3.4 μm - 4.8 μm
Leonardo (Italy/ manufactured in UK)	SUPERHAWK INFRARED DETECTOR	MOVPE with HgCdTe	3.7 μm - 4.95 μm
Leonardo -DRS (USA) Necessary export license	HEXABLU 6 micrometer COOLED THERMAL CORES	HgCdTe	3.4 μm - 4.8 μm
Wuhan Global Sensor Technology (China)	C615M MWIR MCT COOLED FPA DETECTOR RS046	HgCdTe	3.7 μm - 4.8 μm
Xenics (Belgium)	XCO 640 SERIES	HgCdTe	3.7 μm – 4.8 μm 1.5 μm – 6 μm
SCD (Israel)	PELICAN D	InSb	1 μm - 5.4 μm
SCD (Israel)	HERCULES 1280	InSb	1 μm - 5.4 μm
SCD (Israel)	BLACKBIRD 1920	InSb	3.6 μm - 4.9 μm
SCD (Israel)	HOT PELICAN D 640	InGaAs-XBn (HOT detector)	3.6 μm - 4.2 μm
FLIR (USA) Available for Europe	HOT Neutrino Swap C	T2SL	3.4 μm - 5.0 μm
SCD (Israel)	Bird 640 Ceramic	VO_x Microbolometer	3 μm - 14 μm
SCD (Israel)	VO_x imager BB	VO_x Microbolometer	3 μm - 14 μm

Table 3.1 – List of the final selected detectors with the manufacturers, material and wavelength range [16] [17] [18] [19] [20] [21] [22] [23].

Detector Name	Size FPA (pixel x pixel)	Pixel pitch	NETD	F number	Sizing
DAPHNIS-HD MW RM2/K563	1280 x 720	10 μm	<20 mK	f/2	IDCA H <123.5 mm Ø 30.5 mm × L 82 mm 0.55 kg
HiPIR-Engine HOT	1024 x 768	10 μm	<25 mK	f/2.2	60x50 mmm 0.37 kg
SUPERHAWK INFRARED DETECTOR	1280 x 1024 or 1280 x 720	8 μm	20 mK	f/2	IDCA L. 118 mm (Cooler included) 350g
HEXABLU 6 micrometer COOLED THERMAL CORES	1280 x 960	6 μm	<30 mK	Cold Shield (f/2.6)	IDCA 46 x 61 x 68 mm, 295 g (Cooler included)
C615M MWIR MCT COOLED FPA DETECTOR RS046	640 x 512	15 μm	<22 mK	f/2.0	IDCA 124 x 81 x 46 mm <450 g
XCO 640 SERIES	640 x 512	15 μm	22 mK	f/2.0	93 x 100 x 160 mm 1600 g
PELICAN-D	640 x 512	15 μm	20 mK	Cold Shield (f/1.5, f/2)	L. 130 mm, 600 g (Cooler included)
HERCULES 1280	1280 x 1024	15 μm	22 mK	Cold Shield (f/2)	L. 148.5 mm, 800 g (Cooler included)
BLACKBIRD 1920	1920 x 1536	10 μm	<25 mK	Cold Shield (f/3)	L. 150 mm, 1.1 kg (Cooler included)
HOT PELICAN-D 640	640 x 512	15 μm	<28 mK	f/1.5	L. 102.5 mm, 300 grams (Cooler included)
HOT Neutrino Swap C	640 x 512	15 μm	<25 mK	f/2.5	74 mm x 46 mm x 61 mm <380 grams
Bird 640 Ceramic	640 x 480	17 μm	<35 mK	f/1	26 x 23 x5 mm 7 grams <380 grams
VO_x imager BB	640 x 480	17 μm	<35 mK	f/1.9	31 x 31 x 29.7 43 g

Table 3.2 – List of the final selected detectors with the pixel x pixel size, the pixel pitch, the NETD, the f-number and the size [16] [17] [18] [19] [20] [21] [22] [23].

3.5 Conclusions

To summarize, for MWIR detectors, photon detectors have higher sensitivity, responsivity, and noise figures than the thermal detectors, meanwhile thermal detectors offer a low cost and low power consumption option plus it does not require cooling and can operate at ambient temperature.

For the photon detectors, the two with more accountability and the ones with more flight heritage are the HgCdTe and InSb detectors. They offer is considerable, so it is possible to find one adapting the requirements of the mission and this is the most common type of detector selected to study. The major drawback, although for both of these types, is the operating temperature around 80 K, which requires cooling and could be an issue for certain missions. However, there exists the option of the T2SL detector, which their technology is still not fully developed and could be an option to replace HgCdTe as the photon detector with the most important market share, but it is still far from it in terms of quantum efficiency and sensitivity.

Additionally, for the thermal detector, the fundamental one is the VO_x microbolometer, which has been selected for further study. An important characteristic is that they have a wide broadband and could be used as well for the LWIR. One of the disadvantages apart from a worse overall performance is the response time due to a long thermal time constant, this could be also a major drawback needed to assess if the microbolometer is the chosen option.

4 Radiometric Simulation

A radiometric budget or simulation is basic to know from which source the detector receives the signal and how is it and its fundamental characteristics. Thus, to establish a more accurate understanding of the signal received is the key to observe if a MWIR detector could be used in some mission or another and which type of detector is more suitable to fulfill the requirements of a specific mission.

This section dives into the radiometric simulation of the satellite. It will be assessed the external and internal sources which generate the signal the detector receives. Furthermore, it will be performed a radiometric analysis among all components that occur in the process.

4.1 Signal sources

The radiation sources of a mission can be highly variable depending on the requirements of the mission. It takes into account the orbit, the purpose of the mission.

The scenario presented would be the one from a remote sensing mission in the MWIR. Thus, the main goal of the mission should be the surveillance of Earth or gathering information from the Earth's soil, this means that the main source of radiation flux is obtained from the soil, but also it would be taken into account other sources that affect the signal as well. Hence, the analysis would be focused on the acquisition phase of the mission.

Even though the main focus or the most important part of the radiometric budget should come from the Earth's soil, there exist other sources that should not be obviated. One of these sources is the Sun's radiation that reaches the Earth and is reflected back to the space by the atmosphere and the ground. That percentage of radiation reflected back is called albedo and has an important effect on the Earth's observations due to the fact that if this source reflects more power that the target source chosen for surveillance, it can perturb the image taken, preventing to obtain a real image from the targeted spot.

As already mentioned, the Earth's radiation emission is the fundamental one. Conceived as a black body around 255 K [27]. The value of this radiation depends also on the emissivity of the observed area and the wavelength.

Furthermore it should be considered the satellite as an emitter itself, but the radiation emitted does not affect too much the whole system, so it can be neglected, although the temperature is still considerable.

Finally, it exists the Cosmic Microwave Background, which is an electromagnetic radiation which is a remnant from an early stage of the universe. This is approximated as the Deep Space being a black body at a temperature of 3 K, which on the order of magnitude can be completely neglected.

To sum up the following figure represents a good schematic approximation of the radiometric budget taken into account:

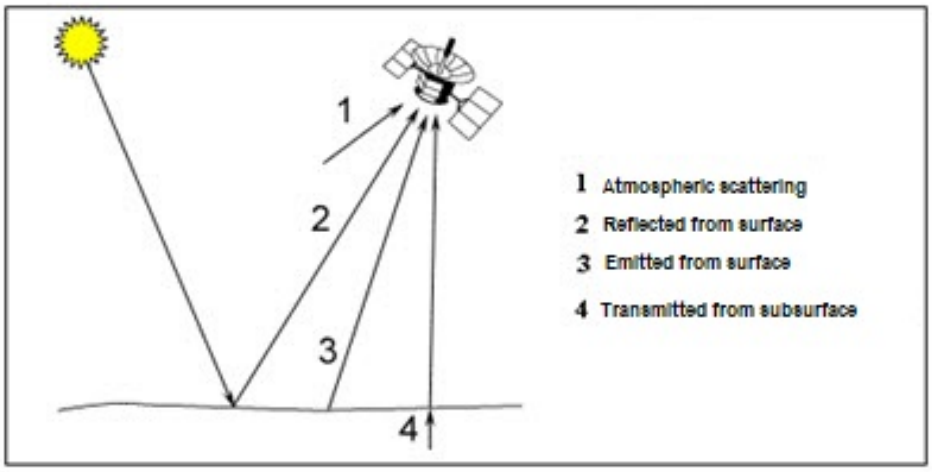

Figure 4.1 – Scheme of the signal sources that affect the satellite [26].

In this scheme, the first source, the atmospheric scattering as it will be mentioned later,it will be not taken into account because a clear sky sky will be considered. Radiation transmitted from the subsurface will also be neglected because it will be a very low level of radiation in the IR band. Therefore, numbers 2 and 3 from the Figure 4.1, will be considered for the simulation, one albedo and the other the ground emissivity.

4.2 Black body radiation

To understand the heat transfer by radiation is necessary to introduce the black body, as it will be used from now on. A black body is an idealized physical object, which absorbs all incident electromagnetic radiation, regardless of wavelength or angle of incidence. As it is at a constant temperature, it emits black body radiation. This radiation is emitted in a spherical distribution and according to Planck's law 4.1, which depends on wavelength and temperature, hence meaning that it is not determined by the body shape or composition.

$$L_\lambda(\lambda, T) = \frac{2 \cdot h \cdot c^2}{\lambda^5 \cdot \left(exp\left(\frac{h \cdot c}{\lambda \cdot K_b \cdot T}\right) - 1\right)} \tag{4.1}$$

Where h is Planck's constant ($h = 6.626 \cdot 10^{-34} J \cdot s$), c is the speed of light ($c = 3 \cdot 10^8 m/s$), K_b is Boltzmann's constant ($K_b = 1.38 \cdot 10^{-23} J/K$).

4.3 External sources

In this section, apart from the ground segment and the albedo mentioned earlier, it should be taken into account the atmospheric transmittance as well.

4.3.1 Atmospheric transmittance

The atmosphere of the Earth is constituted by several gases and an amount of water vapor (Table 4.1), which dictate the atmospheric transmittance.Atomic gases and diatomic gases of the same atomic species do not absorb IR radiation in the thermal IR range. However, molecules constituted by two or more chemical elements (NO, CO, CO_2 or H_2O) are capable of absorbing IR radiation [29].

Gas		Volume
Name	**Formula**	**in %**
Nitrogen	N_2	78.084
Oxygen	O_2	20.946
Argon	Ar	0.9340
Carbon dioxide	CO_2	0.0415
Neon	Ne	0.001818
Helium	He	0.000524
Methane	CH_4	0.000187
Krypton	Kr	0.000114
Hydrogen	H_2	$5 \cdot 10^{-5}$
Nitrogen monoxide	NO	$5 \cdot 10^{-5}$
Ozone	O_3	$7 \cdot 10^{-6}$
Not included in the dry atmosphere		
Water vapor	H_2O	0-3

Table 4.1 – Major constituents of atmosphere per volume [33].

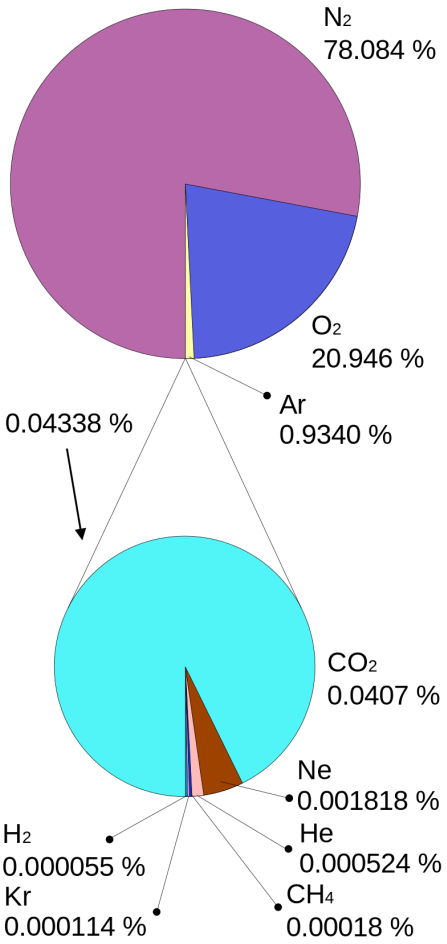

Figure 4.2 – Atmospheric composition for dry air in percentages. Values are mostly from 1987 except methane and carbon dioxide, which are from 2009 [33].

Because of these constituents that absorb IR radiation, there are only specific thermal IR bands in which the Earth observation can be performed normally since for certain wavelengths the atmosphere becomes completely opaque to IR radiation.

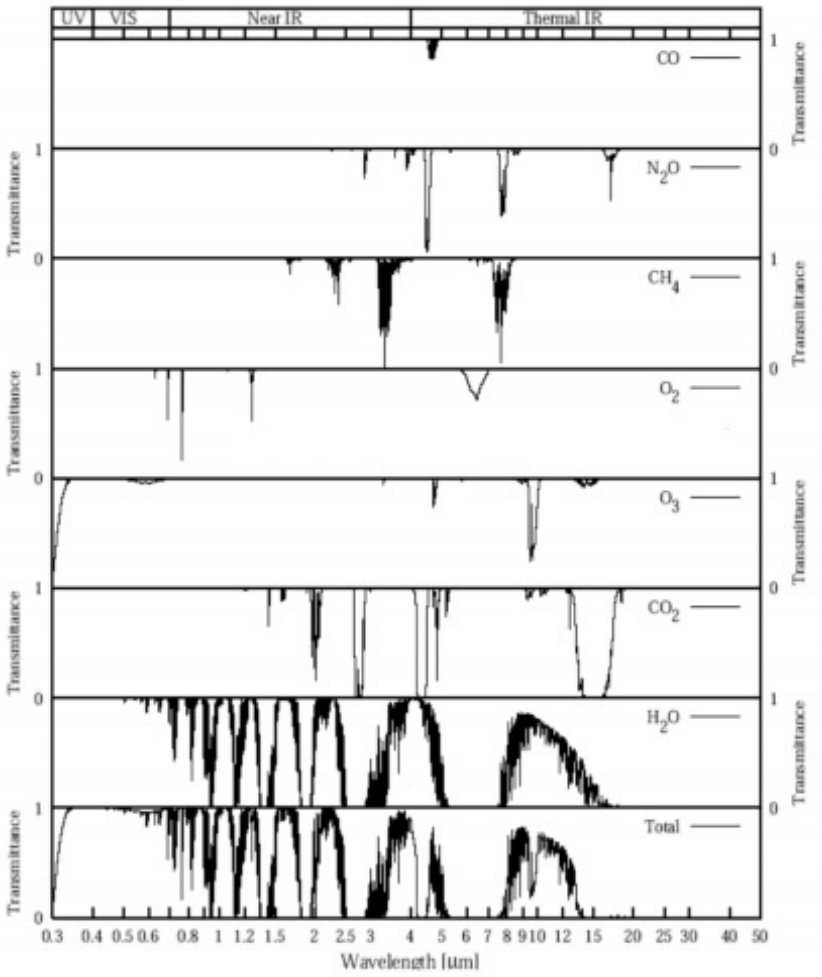

Figure 4.3 – Absorption bands for different constituents of the atmosphere [32].

Is possible to observe that the constituent which affects the most transmittance is water vapor (H_2O). It presents two absorption bands, one from 2.5 up to 3 μm and another one from 5 up to 7.5 μm, the first band dictates the separation between SWIR and MWIR, this band the absorption is also affected by carbon dioxide (CO_2), the second one establishes the separation between MWIR and LWIR.

Molecules nitrous oxide (N_2O) and carbon dioxide (CO_2), also result in an absorption band between 3.6-4.2 μm. Carbon dioxide also results in a big absorption beyond 14 μm and nitrous oxide and methane (CH_4) result in a band after water vapor's second absorption band up to 8 μm. Finally, ozone (O_3) around 9.5 μm in LWIR band, impedes transmission enough to be considered.

There has been developed a model of atmospheric transmittance in the MWIR range to apply the bands mentioned earlier. It has been done based on the observations at the Gemini Observatory [24].

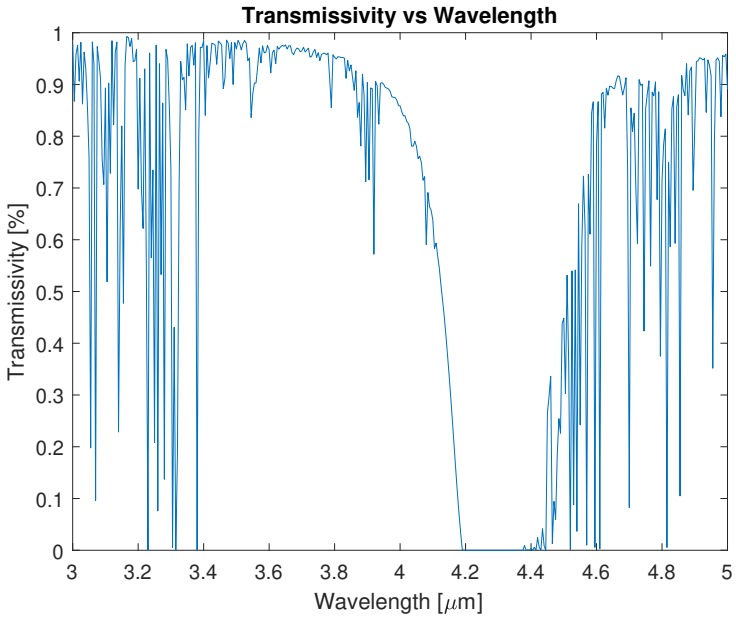

Figure 4.4 – Atmospheric transmittance in the MWIR range. The model follows the guidelines from [8].

There must be done some assumptions to modelize the atmospheric transmittance for the further sections. The results from figure 4.4 are based on the a specific concentration of gas species. The concentration of water vapor is crucial to define the transmittance, as it can vary greatly spatially and temporally. In this case, considering an air mass of 1.0 and a water vapor column of 1.0 as well, this in line with the values for the Gemini Observatory [24].

Air mass is a measure of the amount of air along the line of sight through the Earth's atmosphere. The ratio of absolute air masses, as defined earlier, at oblique incidence relative to the zenith. This means that an air mass of 1.0 is at the zenith, the value increases as the angle of the source and the zenith increases, reaching the peak at the horizon, in which the source will appear less bright.

Water vapor column is the total water in gas state contained in a vertical column of the atmosphere. It must not be confused with the relative humidity, which is the amount of water vapor the air is capable of holding.

Another fact to take into account is scattering, as absorption is not the only factor to reduce the vertical transmission. The Rayleigh scattering must be considered, as the particles are much more smaller than the wavelength of the radiation. Atmospheric gases do not have a great impact on the IR band as the size is too small to affect this wavelength. Although, for some aerosols, not considered in the model, the size can be up to 0.1 μm, such as smoke or dust can perturb IR results but still enhance a good result. Finally, it must be pointed out that the cloud particles are large enough particles to affect the IR wavelength range, which are around 10 μm, so that to simplify it is considered a clear sky for the modelisation of the problem.

4.3.2 Albedo

To discuss about the albedo contribution to the radiometric simulation, some terms must be introduced as the solid angle and the steradian. Spectral radiance is distributed homogeneously as a sphere. Supposing it radiates in one direction and incites in a volume, this energy would be a conical portion of the sphere, which is named the solid angle [25], being the vertex of this

conical region the source of the radiation. Thus, the solid angle defines the amount of field of view occupied by an object. Solid angle is similar to a planar angle but considering three dimensions instead of two and its unit is the steradian sr .

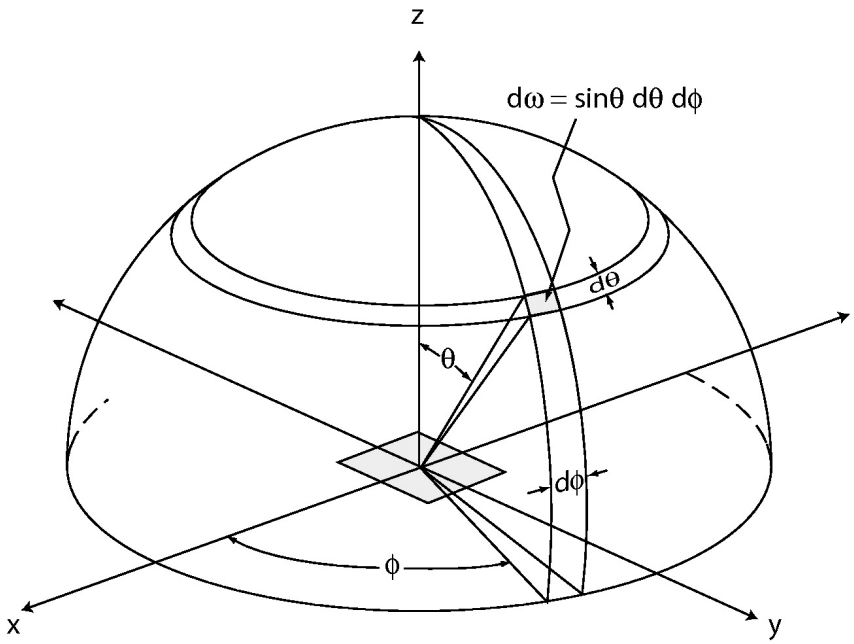

Figure 4.5 – Solid angle in an hemisphere related to the polar coordinates [34]

Integrating in polar coordinates for the whole hemisphere, it is obtained the solid angle for the hemisphere:

$$\int\int d\omega = \int_{\theta=0}^{\pi/2}\int_{\phi=0}^{\pi/2} sin(\theta)d\theta d\phi = 2\pi[sr] \tag{4.2}$$

Is possible to apply the concept of the solid angle in the Sun-Earth relation to further used it in the albedo problem. Knowing that the distance Sun-Earth is large enough to consider Earth as a point and Sun's radius, the solid angle between Sun and Earth is:

$$\theta = 2sin^{-1}\left(\frac{R_{sun}}{d_{Sun-Earth}}\right) = 0.5328[^\circ] \tag{4.3}$$

$$\omega = 2\pi\left(1 - cos\left(\frac{\theta}{2}\right)\right) = 6.7906 \cdot 10^{-5}[sr] \tag{4.4}$$

This solid angle is assumed to be constant, because the variations due to Earth's rotation are neglected.

The spectral radiance that reaches the Earth passes through the atmosphere that is already seen, absorbs, reflects, and transmits this radiation, the same occurs for the radiation that reaches the Earth's surface. The point of interest is the radiation reflected back by the Earth. This radiation reflected back is estimated by the albedo, which is not easy to estimate, as it depends a lot on the surface reached and the wavelength of the radiation, being the global average value around 0.3.

To estimate the value of the albedo, it has been taken into account the data from the ECOSTRESS

Spectral Library [31][8] and some categories and representative materials for each category have been picked up:

- Man-made materials.
- Rock.
- Non-photosynthetic vegetation.
- Soil.
- Water: water, ice, and snow.
- Vegetation

The approach carried out to simulate the albedo is to simply compute the average of these categories, as for now the hypothetical objective of a mission in the MWIR remains open, so this approach is to just observe the value of the albedo for each type of surface. In further sections it will be possible to neglect some surface categories such as man-made materials, which are the ones with a higher albedo and not the target of a mission in the MWIR.

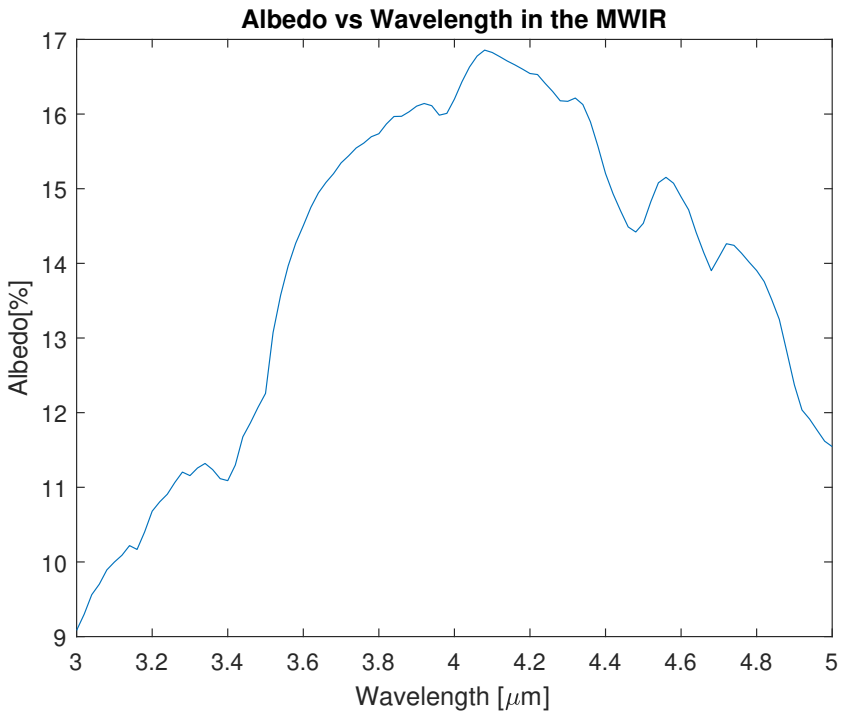

Figure 4.6 – Albedo vs wavelength in the MWIR. Taking into account the multiple surfaces and the solid angle between Sun and Earth.

As can be noticed in figure 4.6 the albedo in the MWIR is in the range of 0.1 up to 0.17. It has to be said although that this model is a worst case scenario [8] because it could be considered a different model in which some of the usual targets for the MWIR, such as crops, water, or vegetation have a higher value in the albedo modelisation as they have a lower reflectivity than made-man materials for example.

The spectral irradiance reflected by Earth has to pass through the atmosphere again until reaching the top, with the consequent loss that this supposes. Furthermore, it is assumed that the Sun radiates as a black body at a temperature of 5800 K [28] and that only one hemisphere of

the Earth is receiving sunlight, as the other one is at night. Hence, the formula must be divided by the solid angle of the hemisphere. Then, the equation that describes the spectral radiance at the top of the atmosphere produced by the Earth's albedo [8]:

$$L_{albedo} = \frac{L_\lambda(\lambda, T_{sun}) \cdot \tau^2(\lambda) \cdot a(\lambda) \cdot \omega}{2\pi} \tag{4.5}$$

Where L_λ is the spectral radiance obtained with the Planck's law (4.1), T_{sun} is 5800 K, τ is the atmospheric transmittance, a is the albedo and ω the solid angle between Sun and Earth previously calculated.

For this model it has been also considered a clear sky, as for the IR as mentioned earlier clouds suppose a problem due to scattering. Cloud droplets also reflect back radiation to the space, up to 70% out of the total radiation the Earth reflects back comes from the clouds. Another assumptions have been made, such as rainfall and aerosols, which could modify the values of the albedo greatly.

4.3.3 Ground

The ground contribution to the signal radiation is the most important one. For the infrared domain, the Earth emission is really relevant. The use of the Planck's law 4.1 will be used in order to compute the signal obtained from the Earth's emissions.

The issue is that Earth is not a perfect black body and not should be treated as one, it emits with a certain emissivity, which depends on the surface observed, and it must be calculated and taken into account to obtain a realistic spectral radiance coming from the Earth's ground emittance.

The emissivity of most natural surfaces is in the range of 0.6 up to 1.0. Emissivities in lower than 0.85 are only typical for deserts and semi-arid areas, while other surfaces like water, snow, cropland, or grass have usually larger emissivities in the IR [8].

Although, to precisely approximate a realistic model, it is not enough to approximate the emissivity by just one value. Instead, it is a function, which delivers the ground emissivity depending on the wavelength.

Different types of ground are considered, following the guidelines from the International Geosphere-Biosphere Programme (IGBP), which establishes 18 [35] different soil types as seen in figure 4.7. However, only 3 have been selected to study the different targets for a mission in the MWIR:

- Croplands in relation to the humidity monitoring of crops.
- Natural Vegetation Mosaics in relation to wildfire surveillance and tracking.
- Water bodies in relation to maritime vessel tracking.

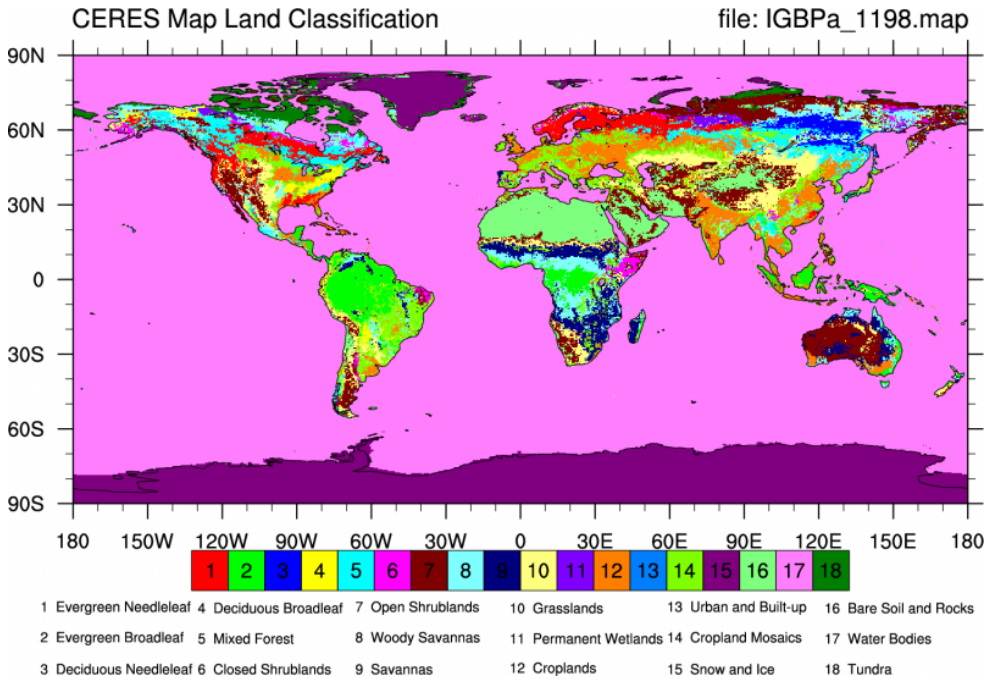

Figure 4.7 – CERES land classification from IGBP [35].

This data was obtained from Cloud and Earth's Radiant Energy System (CERES), a mission, which uses scientific satellite instruments, part of NASA's Earth Observing System (EOS).

The spectral radiance from the ground component will be computed using these different soil types to analyze different possible missions for the MWIR. Furthermore, the same considerations of a clear sky are taken as in the albedo section. Hence, the equation which allows to compute the spectral radiance from the Earth source is [8]:

$$L_{ground} = L_{\lambda}(\lambda, T_{earth}) \cdot \tau(\lambda) \cdot \varepsilon_{ground}(\lambda) \tag{4.6}$$

Where L_{λ} is the spectral radiance obtained with the Planck's law (4.1), T_{earth} will vary, τ is the atmospheric transmittance, ε is the ground emissivity, depending on the type of soil.

4.4 Simulation Results

For the simulation results, as mentioned in earlier sections, there will be computed as for different mission scenarios, in particular three. The first one, humidity monitoring of croplands, which will set the type of soil in croplands and a range of temperature of 270-310 K. The second one, based on maritime vessel tracking, which will set the same range of temperature and soil in water bodies. The third and final one, wildfire tracking, which is set in a high temperature range of about 960-1000 K and a natural vegetation mosaic. With these variables set, next are the presented results.

4.4.1 Low Temperature and Cropland Soil

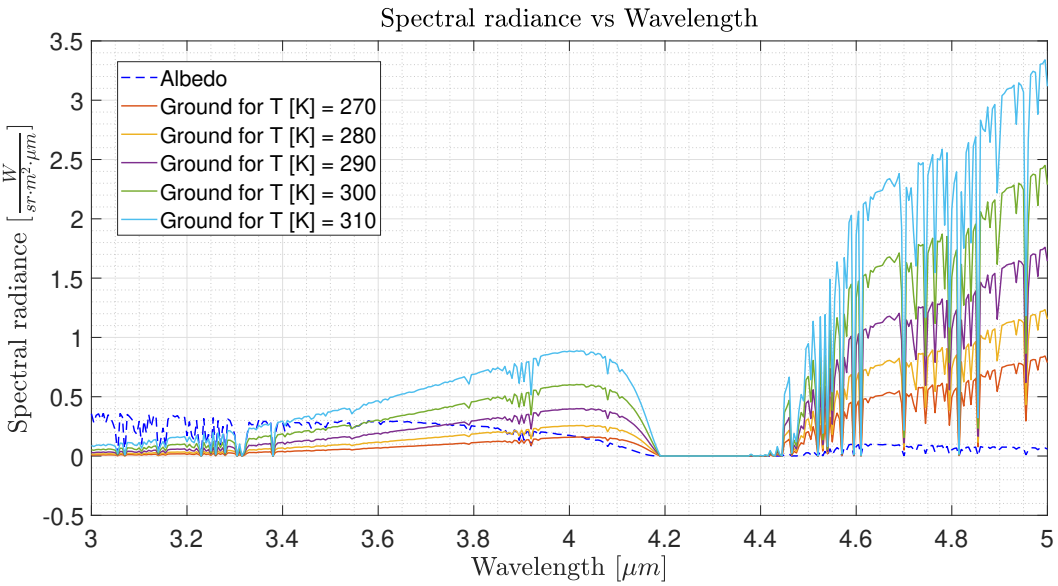

Figure 4.8 – Radiometric simulation for a temperature range of 270-310 K and croplands type of soil.The conditions of this simulation are f-number= 1.4 and pixel size= 10 μm.

For this first scenario, there are some conclusions obtained from figure 4.8. The first one is that the spectral radiance emitted by the satellite can be negligible for the whole band compared to the other two sources. Moreover, beginning at the start of the band at 3 μm the albedo spectral radiance is predominant until it starts decreasing at approximately 3.6 μm up to where exists the gap already mentioned before between 4.2-4.4 μm, due to the atmospheric transmittance. Then, signal from the ground predominates over the albedo and keeps increasing while the albedo decreases. Thus, the final conclusion of the MWIR band for these conditions is that there exist two bands that can be used which are from 3.6-4.2 μm with a considerable perturbation from the albedo and another one from 4.4-5 μm which the ground source signal will be received without significant perturbations.

4.4.2 Low Temperature and Water Body

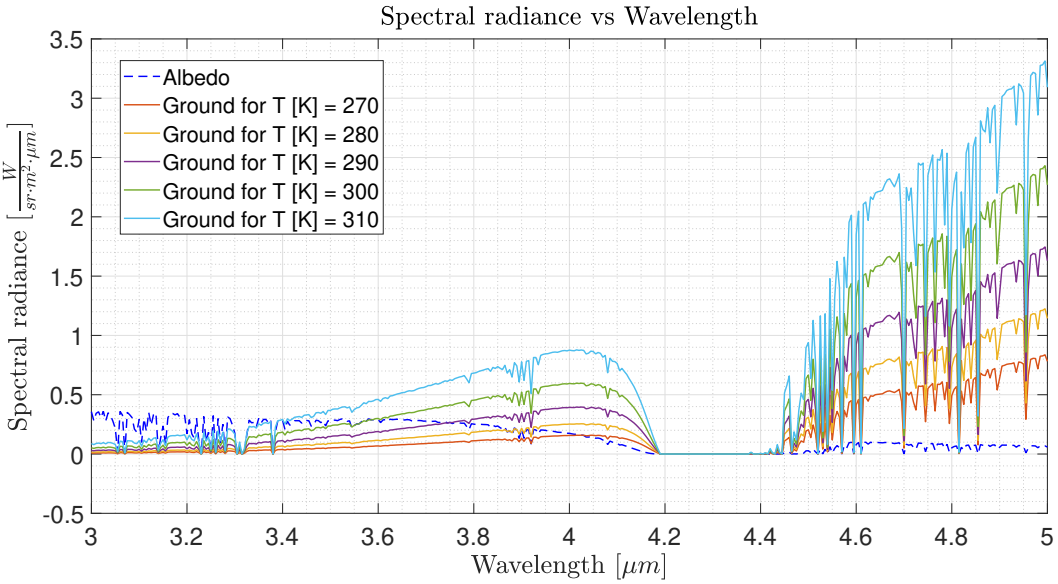

Figure 4.9 – Radiometric simulation for a temperature range of 270-310 K and water body type of soil.The conditions of this simulation are f-number= 1.4 and pixel size= 10 μm.

For the second scenario, the results are nearly identical that the ones from the first scenario. The reason behind this is because of the ground emittance being almost the same even though the type of soil chosen is different, because as mentioned earlier, almost any kind of soil in the IR band has a high emissivity from 0.85 up to 1.0. Thus, the conclusion of this scenario is that regarding the radiometric budget is almost identical as the first one and can be treated the same in further studies.

4.4.3 High Temperature and Natural Vegetation Mosaic

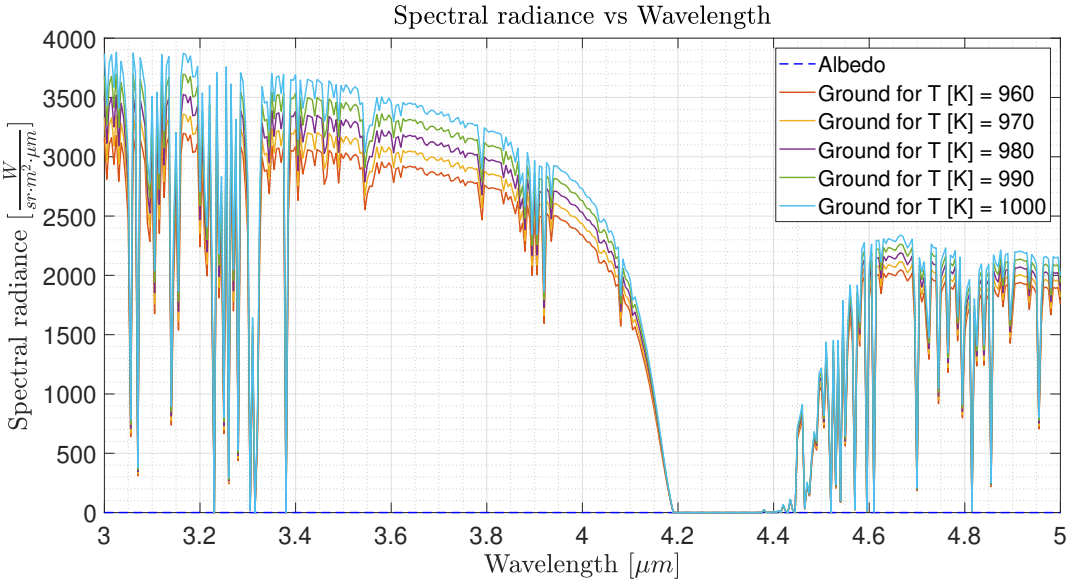

Figure 4.10 – Radiometric simulation for a temperature range of 960-1000 K and natural vegetation mosaic type of soil. The conditions of this simulation are f-number= 1.4 and pixel size= 10 μm.

For the last and third scenario, the results are rather different. At high temperature, it results in a large spectral radiance emitted from the ground with the signal being three orders of magnitude higher than the other scenarios. This implies that the albedo is not predominant and can even be neglected. The only common feature is the gap produced by the atmospheric transmittance. Hence, for this mission, the target is possible to use the band from 3.6-4.2 μm without considering perturbations from the albedo.The only drawback is that around 1000 K the signal becomes unstable and can be a source of problem when obtaining the signal.

4.4.4 Power per pixel

Related to the earlier sections, it has been computed the power per pixel as an estimation of the sensitivity of the detector. In this simulation, it has been used a GSD of 20 m, a f-number of 1.4, and a pixel size of 10 μm. For this, it is also known that the incident power is detectable after 270 K in the MWIR, but its tendency grows rapidly and it surpasses the LWIR band in blue around 700 K. This enables the selected detector to obtain more information about higher temperatures of the Earth and better than the LWIR.

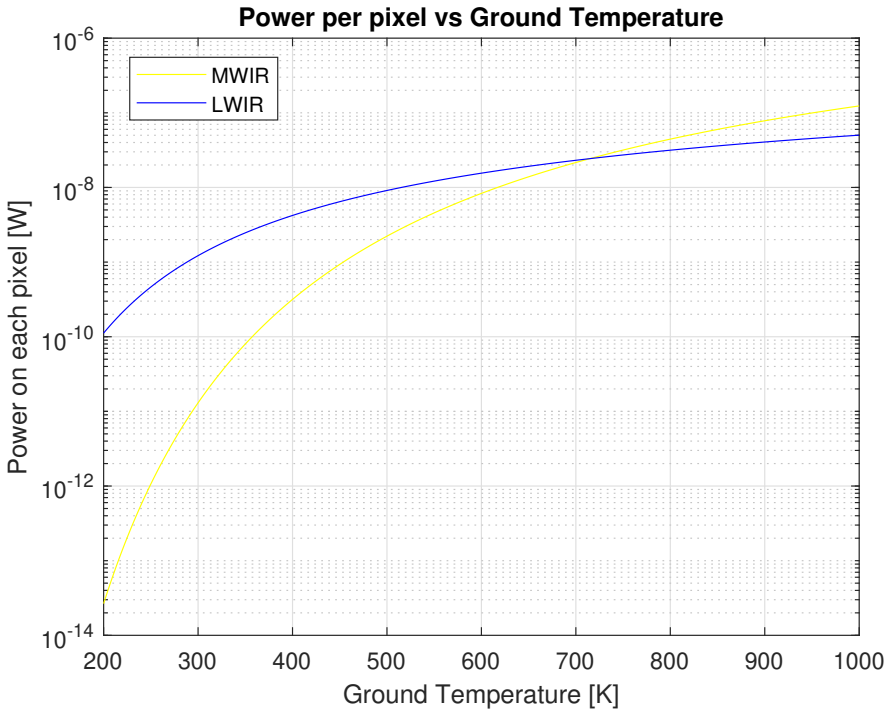

Figure 4.11 – Power per pixel vs temperature for a high temperature range.The conditions of this simulation are f-number= 1.4, pixel size= 10 μm and transmittance optics= 0.9. is in accordance with the results obtained in [36].

4.5 Conclusions

There are several relevant conclusions obtained from the simulation of the radiometric scenario. The first and most important one is that the albedo is quite relevant for low temperature missions and the first wavelength range in the MWIR. Therefore, that they exist two bands useful in the MWIR, one in between 3.6-4.2 μm considerably perturbed by the albedo and another one between 4.4-5 μm where the albedo can be obviated. This condition changes when observing high temperature scenarios in which the albedo is almost non existent, at least for the level of radiation received by the detector.

Additionally it has been proved that the ground emissivity is not restrictive in terms of which type of soil is selected to observe, because as shown, all types of soil have a high ground emissivity so that the radiation obtained from the ground does not vary a lot depending on the type of soil in the MWIR band.

Finally, it has been proved that the MWIR surpasses the LWIR in terms of permonance for high temperatures, as the power per pixel received is greater than for the LWIR in those conditions (4.11).With this being said between the three mission scenarios for the maritime vessel surveillance and the humidity crop monitoring, the radiometric conditions are almost identical, meanwhile for the wildfire surveillance mission it shows a better scenario for the MWIR with the possibility of receiving a stronger signal, which opens multiple possibilities.

5 Nanosatellites and CubeSats with Mid Wave Infrared payload

In this chapter, there will be mentioned different nanosatellites and more specifically CubeSats, which carry MWIR payload. These missions are of special interest for future applications involving MWIR technology as they present an example of which type of detector was used for a specific purpose or application and which are the target performance of the mission. These missions and detectors can be used as a reference for future investigations in a specific subsystem and its relation to others subsystems.

5.1 Past missions

5.1.1 Qbito (ES01) – Polytechnics University Madrid – Spain – 2U- 2017/04/08 – No signal reentered

Qbito is a 2U CubeSat with 2 kg mass, which takes part in the QB50 European project.This project comprises a network of up to 36 CubeSats. The project was led by Von Karman Institute and its main goal was to obtain information on the properties of the lower atmosphere. The orbit characteristics of the Qbito were an altitude of 420 km and 51^o [38]. The main objective of this mission is to operate its primary payload and ion mass and neutral mass spectrometer (INMS). It carried also as a secondary payload MWIR detector developed by the Spanish Company New Infrared Technologies. The manufacturing process is based on the Vapour Phase Deposited PbSe technology in space conditions [38].

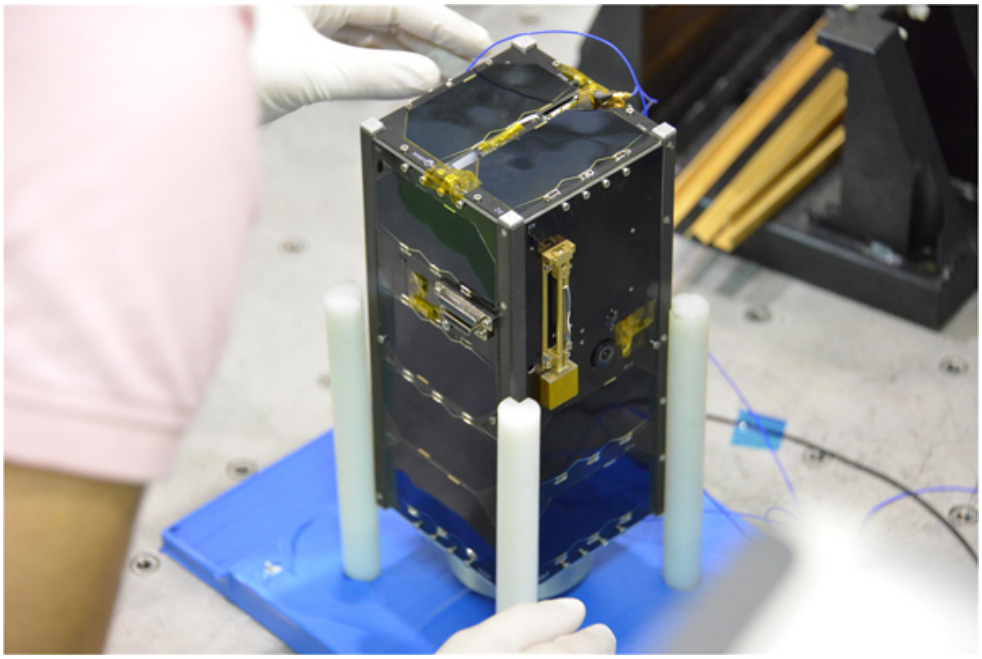

Figure 5.1 – Qbito CubeSat [39].

5.2 Present missions

5.2.1 Arkyd 6A (A6A) – Planetary Resources – US – 6U – 2018/01/12 – Operational

Arkyd 6A is a 6U CubeSat developed by Planetary Resources. Designed to accommodate a MWIR instrument, the main objective was to test the technology for the Arkyd-100 CubeSats.

The primary payload is MWIR Imager, which some of the most important features of the spacecraft are [40]:

- Mass: 10 [kg].
- Spectral range: 3.4-5.1 [μm].
- Altitude: 500 [km].
- Ground spatial resolution: 26 [m].
- Focal length: 200 [mm].
- FPA material: Indium Antimonide (InSB).
- Operation temperature 77 [K], cooled with a Stirling cryocooler.
- Ground footprint: 19 x 15 [km].

The target of this mission was to prove a method to detect water through MWIR and map thermal energy. As it can be noticed, it has a quite good spatial resolution for a CubeSat and is not too large and the MWIR detector is one of the most developed technologies as it is the InSb. The issue with this mission that it has requirements that are quite similar to the one of this Thesis is that the company which was in charge of the mission Planetary Resources went out of funding, so the data from the mission is no longer available to check if the mission was a success or not.

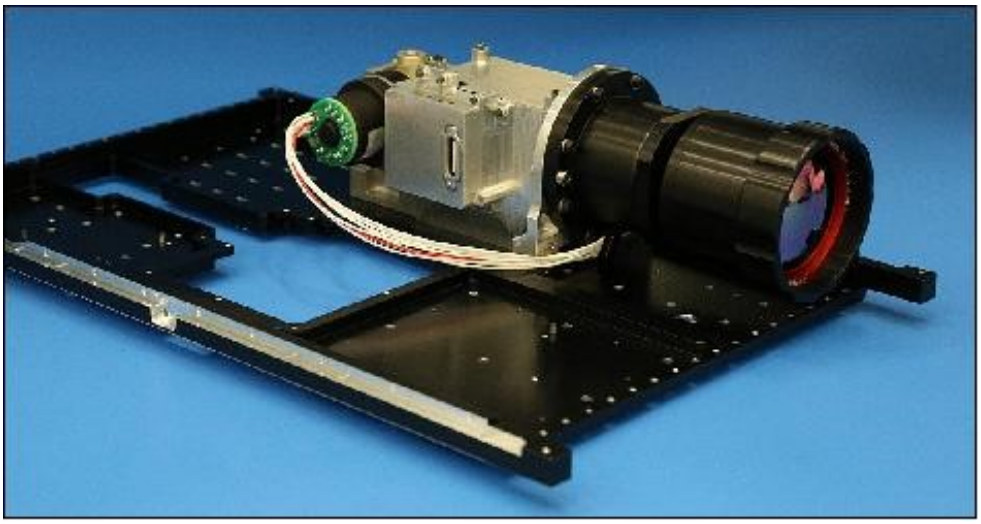

Figure 5.2 – MWIR Imager for the Arkyd-6A mission [40].

5.3 Future missions

5.3.1 LunIR (SkyFire, Lunar InfraRed imaging) – Lockheed and Martin – US – 6U – Not launched

LunIR is a 6U CubeSat developed by Lockheed and Martin and Tyvak Nano-Satellite Systems. It is a very interesting mission even though there is not much information about it, it is scheduled to be launched in November 2021 - March 2022 and is still not sure the launch date.The LunIR will be deployed along another 13 CubeSats during the mission Orion Artemis-1. It will perform a lunar fly-by and is expected to be equipped with a cooled MWIR detector and to have a mass about 14 kg [41]. The target of the mission is to characterize the lunar surface, the remote

sensing of the moon, and to risk reduction for future human missions to help in the site selection observations.

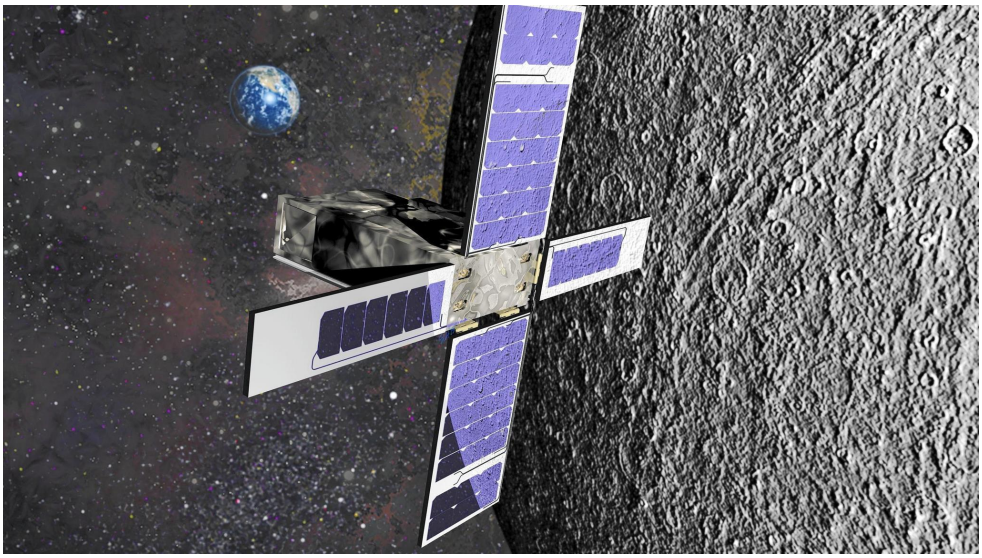

Figure 5.3 – LunIR CubeSat [42].

5.3.2 CIRAS (CubeSat Infrared Atmospheric Sounder) – NASA – US – 6U – Not launched

CIRAS is a 6U CubeSat developed by NASA. The objective of CIRAS is to develop an infrared sounder in a CubeSat. Demonstration mission of three new infrared (IR) sensing and cryogenic technologies that can be able to reduce the size and cost of future space-borne IR remote sensing instruments.

The main characteristics of the mission are: which some of the most important features of the spacecraft are [43]:

- Mass: 14 [kg].
- Spectral range: 4.08-5.13 [μm].
- Spectral channels: 625.
- Orbit Altitude: 450-600 [km].
- Ground spatial resolution: 13.5 [km].
- Target temperature: 250 [K].
- NETD @ 250 K: 0.2 - 0.6 [K].
- FPA material: Barrier GaInAsSb.
- Operation temperature 150 [K], cooled with a Stirling cryocooler.
- Swath: 165 [km].
- Power consumption: 37.5 [W].

The CIRAS as observed can be a technology changing mission, it has incorporated two new instruments very interesting for the MWIR detectors. The first is the state-of-the-art HOT-BIRD detectors, which offer low noise, low cost, and higher operating temperatures than the most used materials in the market. Moreover, the Micro Pulse Tube (MPT) cryocooler, which provides of new possibilities as it enables a longer life mission thanks to its improved cooling capacity.

The objective of the mission is to gather information from the lower atmosphere, specifically in the troposphere, about water vapor and other atmospheric gases. Even though it is a very interesting mission to take into account, it is not very in-line with the proposed spatial resolution as the targeted spatial resolution for the CIRAS is really high to cover as much atmosphere as possible and not survey certain points of interest as it is the target of the proposed mission in this Thesis.

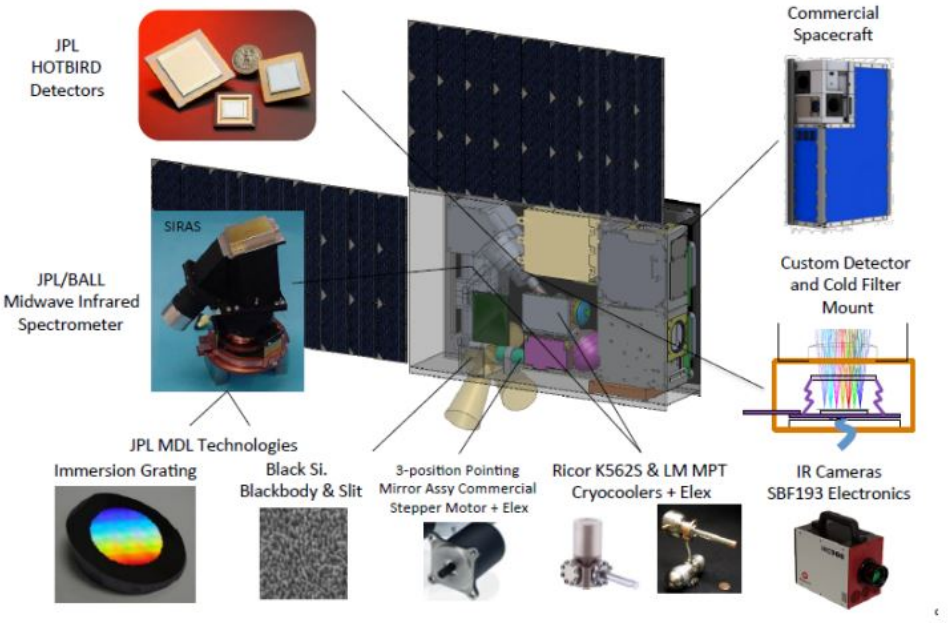

Figure 5.4 – Optical subsystems for the CIRAS mission [43] .

5.3.3 eve-1 – OroraTech – Germany – 3U – Not launched

eve-1 is a 3U CubeSat developed by OroraTech in collaboration with TUM. The main purpose of this mission is to test the prototypical technology to later be used for the detection and tracking of wildfires. There is a patent pending Thermal Infrared Imager, which contains an uncooled microbolometer. Thermal system was also implemented to stabilize the detector at a 8 mK variation. There were also some experiments carried out [36]:

- NETD $<$ 100 mK.
- Absolute temperature accuracy maximum deviation of 2.5 K due to the size of the source effect.
- Best performance measured at 20^{o}C.
- Sub-pixel hotspot detection

Some other characteristics of the spacecraft, the optical system, and the detector include [36]:

- Orbit altitude: 600 [km].

- Spectral range: 3-12 [μm].
- Pixel pitch: 17 [μm].
- Lens design: 50mm f/0.72 .
- Ground spatial resolution: 200 [m] .
- NETD: 50 [mK].
- Power consumption estimation: 15 [W].

The optical design of the mission includes a 17 μm pixel pitch on the microbolometer. A 70 mm aperture to achieve a ground spatial resolution of 200 m at a 600 km orbit. The lens design is a 50 mm maximum diameter with f/0.72, which is challenging in terms of cost and feasibility but still manageable. This mission it is also really interesting, especially because the detector chosen is a microbolometer. This enables two main advantages that respect photodetectors, the first one, it does not require a cooler because it operates at room temperature enabling to reduce the size of the spacecraft and the second one, it enables the possibility to operate in a dual band system as the spectral range of the detector is both for MWIR and LWIR adding the possibilities of remote sensing in the LWIR. Another particularity of this mission is to use the advantage of a higher temperature of the soil when tracking wildfires, to install a microbolometer in the MWIR range that has a better performance due to the power density being higher because of the high ground temperature compared to other missions. This is shown in Figure 5.5.

Although, it may rise to some concerns because it is not clear if the long response time of the thermal detector supposes a problem for the mission requirements and the spatial resolution is still a little too low.

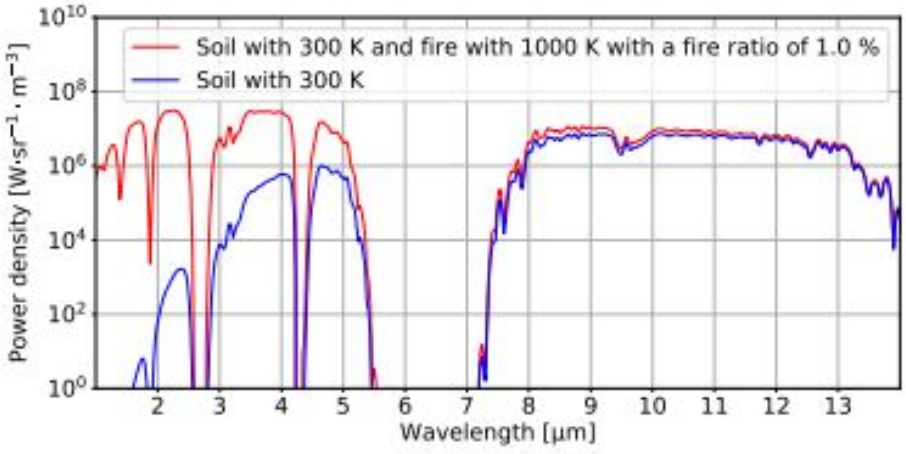

Figure 5.5 – Simulation of power density emitted by soil with and without fire vs wavelength [36].

5.3.4 ERNST (Experimental Spacecraft based on Nanosatellite Technology) – Fraunhofer EMI – Germany – 12U – Not launched

ERNST is a 12U CubeSat developed by the Fraunhofer Institute to evaluate the utility of a 12U nanosatellite mission built with CubeSat components for scientific and military purposes. The main payload is an advanced MWIR camera for monitoring the Earth infrared background. In addition, there is a radiation sensor for in-orbit measurements, Cryocooled MWIR detector. The system objective is to observe the Earth in two spectral bands and look for ballistic missiles

during their launch [37].

Some of the characteristics of the mission are [37]:

- Orbit altitude: 500-600 [km] sun synchronous orbit.
- Spectral range: 3-5 [μm].
- Material FPA: InSb.
- Swath width: 164 [km].
- Power consumption estimation: 20 [W].

The other components of the optical payload include, apart from the detector, one filter to switch to multiple spectral bands, the crycooler needed to cool the detector until an operating temperature for the InSb (80 K), and the data processing unit. All elements are assembled as Figure 5.6 shows. There is not much information about the detector and the orbit apart from the material of the detector and that the optical design is more focused in a large swath sacrificing a high spatial resolution.

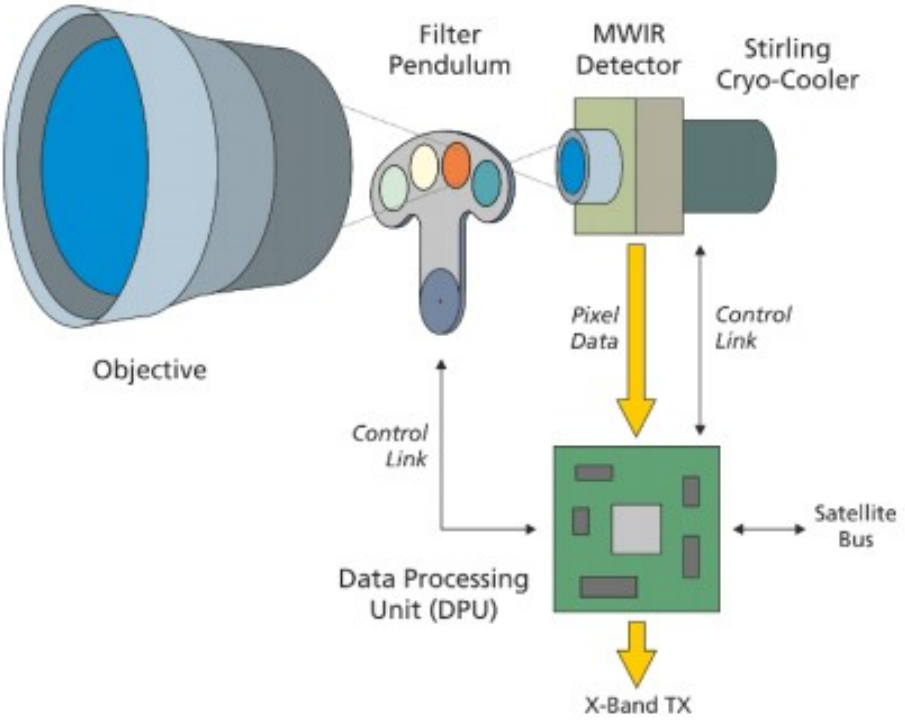

Figure 5.6 – MWIR imager payload block diagram [37].

5.3.5 AMS (Agriculutural Monitoring) – ISISpace – Netherlands – 16U – Not launched

The AMS is a 16U CubeSat developed by ISISpace to Demonstrate MWIR instruments in a CubeSat.
It is not provided much information as it seems to be a preliminary plan for a CubeSat mission, knowing only the objective, which is to provide data in real time for the soil moisture and further implications as a commercial scalable service [44].

5.4 Cancelled/Failed missions

5.4.1 Arkyd-100 – Planetary Resources – US – 12U – Cancelled

Arkyd-100 was supposed to be a constellation of 10 satellites, 12 U satellites that their main target was to provide mid-wave infrared information and multispectral data for any point of interest on Earth. The mission and detector payload main characteristics are [45]:

- Spectral Range : 3.4 -5.1 [µm]
- Mass: 20 [kg].
- Orbit Altitude: 550 [km] sun-synchronous orbit.
- Array Size : 640 x 512 pixel.
- Focal Length : 720 [mm].
- Optical Diameter : 8".
- Ground Footprint : 7.3 x 5.8 [km].
- GSD : 15 [m].

Figure 5.7 – Arkyd-100 model CubeSat [45].

This constellation was supposed to be the first real example of a profitable application and a total global coverage in the MWIR using CubeSats. It would have inherited the optics and detector from Arkyd-6 and a high spatial resolution suitable for the mission standards proposed in this Thesis. It was cancelled as Planetary Resources, the operator and manufacturer went out of funding.

5.4.2 Arkyd 6B (A6B) – Planetary Resources – US – 6U – Cancelled

Arkyd 6b was supposed to be a 6U CubeSat developed by Planetary Resources to be of the same series of Arkyd 6A, but it may have had been canceled due to the same reason that the company Planetary Resources went out without funding.

5.5 Conclusions

Of all CubeSat missions, nearly 50 carry a payload of IR. Of these 50, only 7 use a MWIR detector. These missions are the Qbito, the Arkyd 6A, CIRAS, LunIR, ERNST, AMS and eve-1. The MWIRS used or planned to use in these missions [38] [40] [43] [37] [36] [44] [41]:

- PbSe Technology for the Qbito detector.
- InSb detector array with Stirling cooler for the Arkyd 6A.
- HOT-BIRD detector for CIRAS.
- InSb detector array with Stirling cooler for ERNST.
- Uncooled microbolometer for eve-1.
- HgCdTe detector from Sofradir E2V and AIM for the AMS. mission.
- Not specified but with microcooler for the LunIR.

It is clear that the main aspect to highlight is that there are few CubeSats in the IR and even fewer in the MWIR. For that reason, it should be a spectral band with large possibilities as it is has not been exploited for nanosatellites. It has been also not real space proven except for Arkyd 6A which remains the more interesting mission among the studied because it has a spatial resolution and size which are the target of this Thesis, which shows that a CubeSat with these characteristics is possible. Moreover, future missions open a considerable number of opportunities, especially the eve-1 mission, which includes a microbolometer and dual-band in the LWIR as well. However, it will have to wait because it is uncertain when future missions will be launched to see how they progress and what they can achieve. Furthermore, it has been noticed that the size of the CubeSats keeps increasing because of the future missions studied, all but one are larger than 3U, which means that launch costs are reducing allowing spacecrafts to be larger and thus, be able to install in this case larger optics, detectors and other subsystems to enable a better performance of the mission.

6 Results and analysis of different detectors

6.1 Pre-sizing

In this section, it will be carried out the study of the different selected detectors from the market which have the best features to perform the three proposed missions. Hence, first of all is to have a pre-sizing of the spacecraft needed to achieve the main resolution goal of the mission, that is, to have a 20 m GSD. To do so and as explained in section 2.3, is obtained the GSD and swath of the proposed mission with the variables of the maximum diameter of the optics, the f-number, and the pixel size of the detector. It is fixed that the altitude of the orbit is 500 km and that the sensor width is 640 pixels.

6.1.1 Parametric study

A parametric study will be carried out to know the trade-off between the variables and decide regarding which variables are more compromised to achieve the target values. The model used to obtain the results is the one from [9].

6.1.1.1 f-number

The first parametric study it is been done for the f-number. In this case, the pixel size has been fixed for 10 μm meanwhile the other variables such as the f-number and maximum diameter are varied inside a range of 1.0 up to 2.0 for the f-number and 50 up to 200 mm for the maximum diameter. The procedure is to vary first the maximum diameter to obtain the maximum clear aperture and with this and the f-number obtain the effective focal length (EFL). ´Then knowing the pixel size, altitude, and the effective focal length is possible to compute GSD. Finally, multiplying by the sensor with the swath is obtained. The maximum length is obtained by multiplying by a factor of 1.3 EFL.

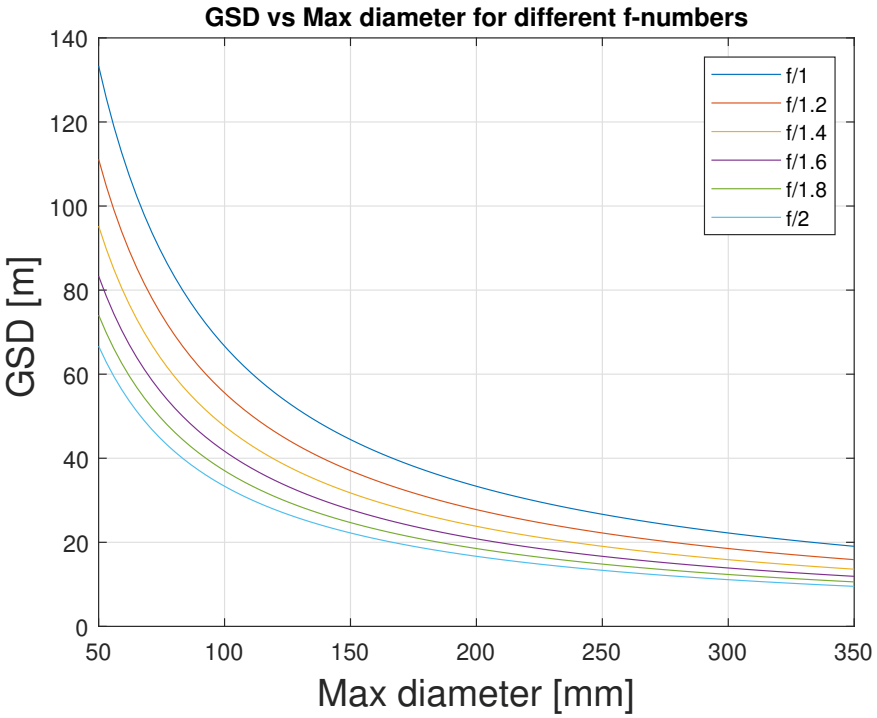

Figure 6.1 – GSD vs max diameter for different f-number. For pixel size= 10 μm and H=500 km.

Once performed, the parametric study for the f-number is concluded that a higher f-number results in a better ground resolution as the plot trend is to decrease for higher f-number. Moreover, for lower diameters, the difference between choosing an f-number or another is more notable and the difference decreases as the diameter increases, so by choosing a large diameter it is possible to choose between different f-numbers without losing resolution.

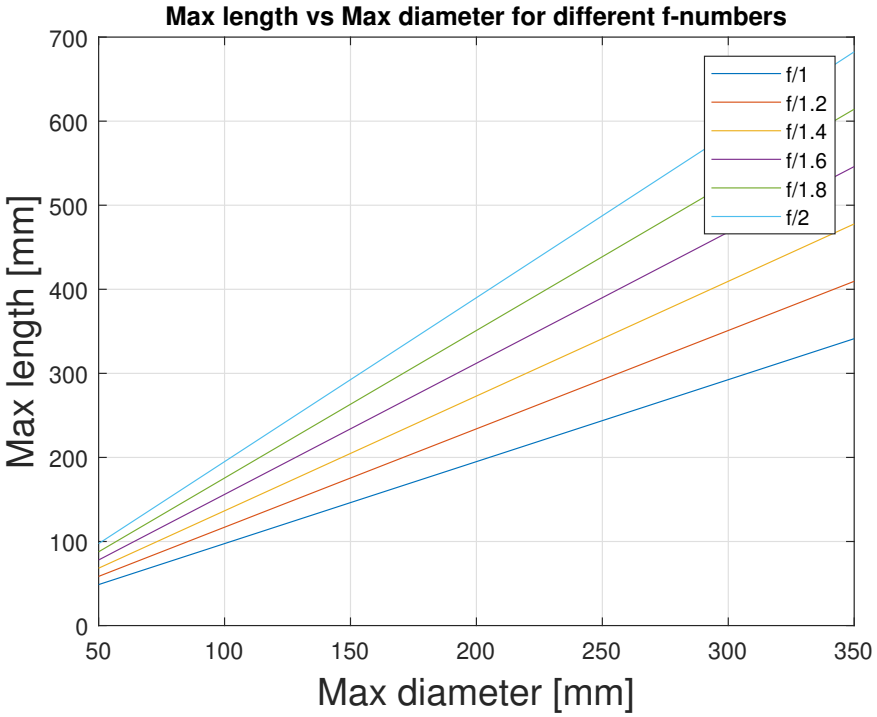

Figure 6.2 – Max length vs max diameter for different f-number.For pixel size= 10 μm and H=500 km.

Here are presented the relation to the length of the optics. From this trend, it is possible to observe that for larger diameters, it will translate into a large length for larger f-numbers. Being the difference larger between choosing f-number when the diameter is larger. Thus, a large diameter will translate into a large length, also compromising the size of the spacecraft.

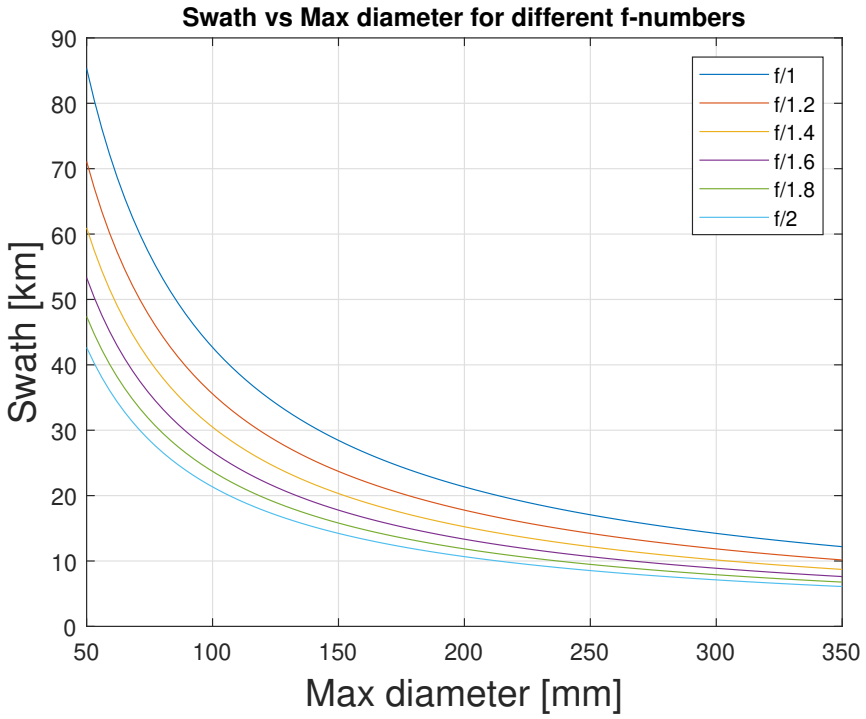

Figure 6.3 – Swath vs max diameter for different f-number.For pixel size= 10 μm, H=500 km and sensor width= 640 pixels.

For the swath, the curves are, as expected, equal as the ones for the GSD. In this case, as the swath is interesting to be as large as possible, the relation is inverse as for the GSD, as the lower the f-number a larger swath is obtained. However, it is not as restrictive as the GSD because the surveillance will be only of a determined zone and not the whole globe and it can be chosen another detector with a larger array of pixels.

6.1.1.2 Pixel size

The same parametric study is performed for the pre-sizing but now varying the pixel size instead of the f-number. F-number is fixed, this time at 1.4, the altitude and sensor width remain the same. Diameter is varied from 50 up to 200 mm as well and the pixel size is varied from 6 up to 17 μm. The procedure is the same as the previous section, next are presented the results of the study.

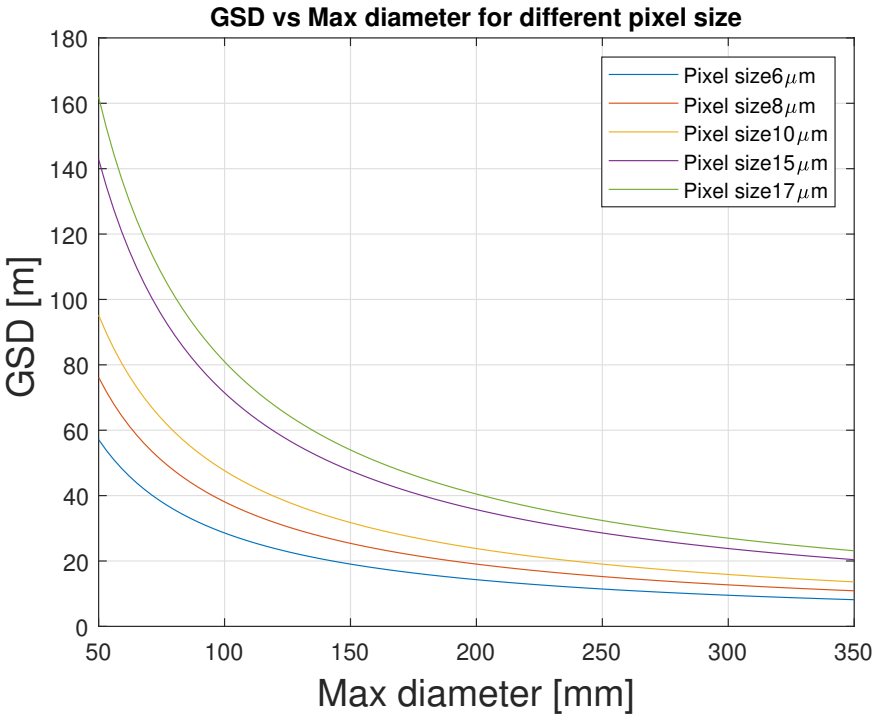

Figure 6.4 – GSD vs max diameter for different pixel sizes. For a f-number= 1.4 and an altitude H= 500 km.

The results of the parametric study of the pixel size reveal that the relation is inverse to the one of the f-number, as lower the pixel size it is obtained a better spatial resolution. The difference of choice between pixel sizes reduces with the diameter. The matter with the pixel size and the f-number is that it may result in a problem related to the diffraction limit, so a trade-off must be made to avoid trespassing the limit or work on a solution.

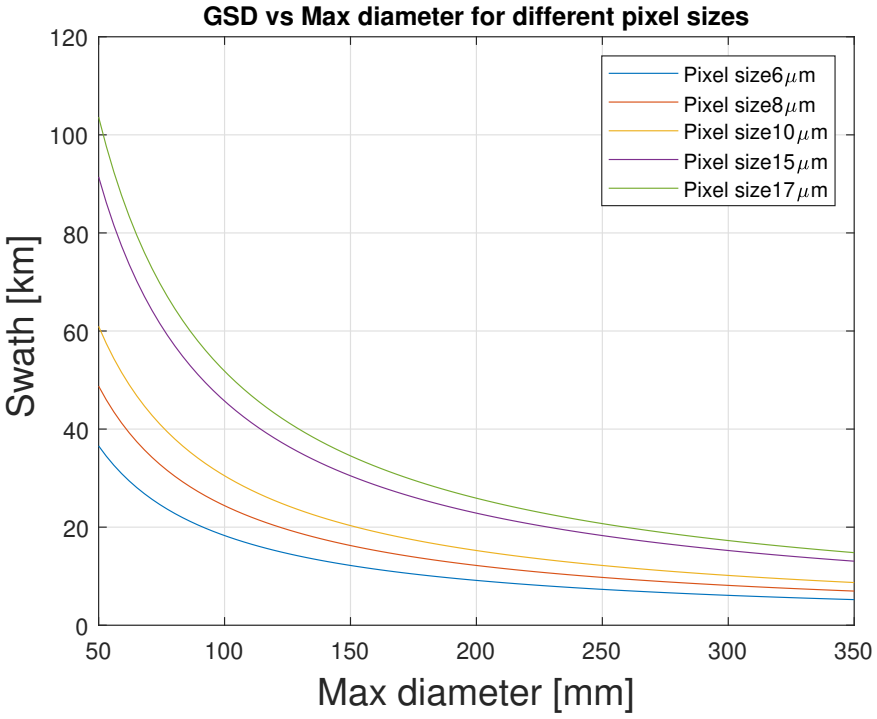

Figure 6.5 – Swath vs max diameter for different pixel sizes. For a f-number= 1.4, altitude H= 500 km and sensor width= 640 pixels.

As expected, the results show that for a larger pixel size the swath increases, but again there is not a critical value in which the mission can be limited.

6.1.2 Detector comparison

Then, it is presented a preliminary sizing of the detectors including the measures of the selected list and adding their measures, the ones included in the optic assembly necessary to obtain the desired spatial resolution. It is chosen a f-number of 1.4 and a pixel size of 10 μm. The maximum diameter is varied from 50 up to 350 mm to compute how it affects the sizing of the satellite. To note that measure L accounts in the direction of the the optical axis.

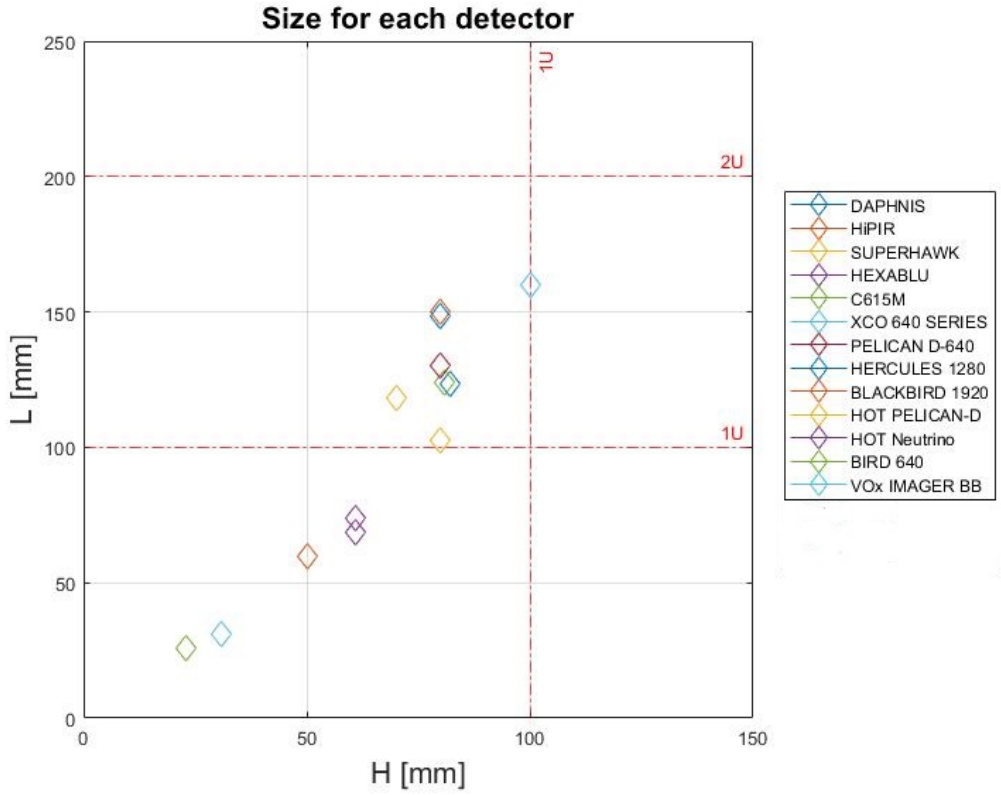

Figure 6.6 – Length and height for each studied detector.

When introducing the measures of each detector into the same plot, it shows as expected that the smaller detectors are the microbolometers VO_x Imager BB and Bird 640 from SCD, followed by the MCT detector Daphnis HD MW, the HOT Neutrino Swap C and the Hexablu 6 μm are the only detectors that could fit into 1U CubeSats but this without considering the optics necessary (see Table 3.2 for more information). The others could fit into a CubeSat 1Ux2U except for XCO 640 series which is too large.

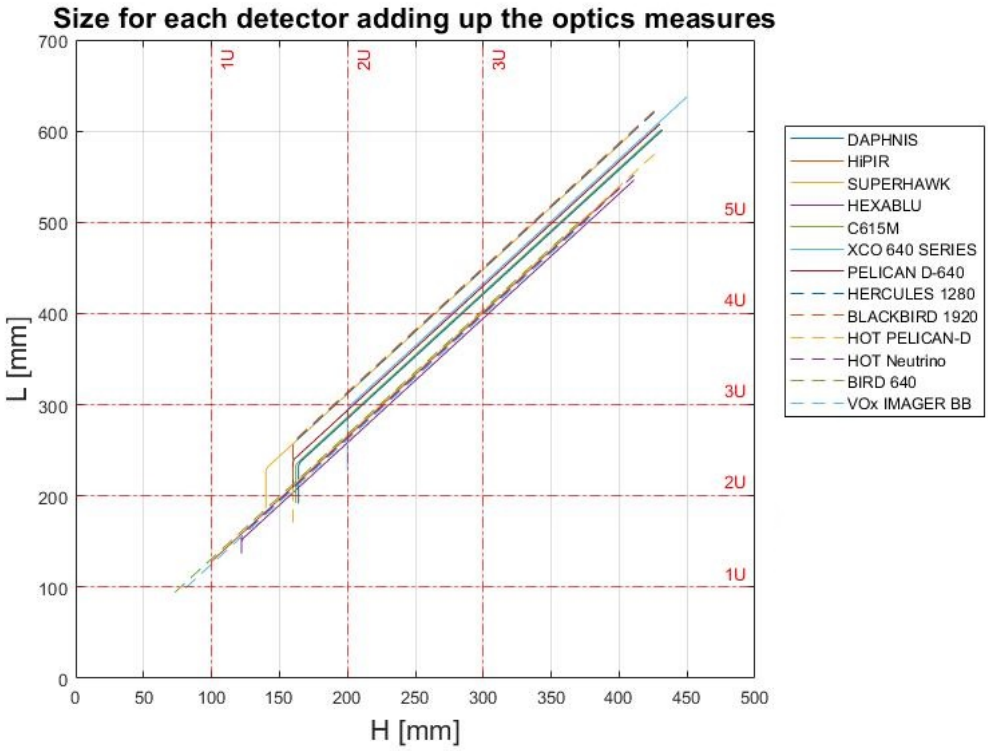

Figure 6.7 – Length and height for each studied detector adding the length and diameter necessary for the optical assembly. For a f-number= 1.4 and a pixel size= 10 μm

When adding the optics, the scene varies a lot, as the minimal size for a CubeSat to fit the optical and detector assembly is 1Ux2U and only for the bolometers. As it is seen, the relation is directly proportional between the length and height of the optical and detector system, this should be useful to estimate the sizing of the spacecraft once the diameter of the optics is fixed as it is related with the value of the height in the plot.

6.2 Temperature resolution and signal-to-noise ratio

To compute the performance of the detectors, it is needed to obtain the temperature resolution through the Noise Equivalent Temperature Difference (NETD) measured in space and the Signal-to-Noise Ratio (SNR) to simulate the quality of the signal and the detectivity of the detector. The model used to obtain the results is the one developed in [9].

6.2.1 Parametric study

First of all, it is performed a parametric study to observe how the trend is when varying the f-number. In this case it has been taken the data from the detector Daphnis HD MW from Tables 3.1 and 3.2. The wavelength range is from 3.7 up to 4.8 μm, the pixel size is 10 μm, the f-number tested on the ground is 2.0, the f-number for the spacecraft optical system is considered 1.4, the NETD measured on the ground is 20 mK. The fill factor, which is the percentage of the pixel surface sensitive to incident radiation, is supposed at 0.75 and the transmittance of the optics is supposed to be 0.9. The range of ground temperature is established between 270 up to 310 K, the altitude of the satellite is 500 km, and the type of soil is set to be cropland, to simplify the problem also has been considered an atmospheric transmittance of 0.614.

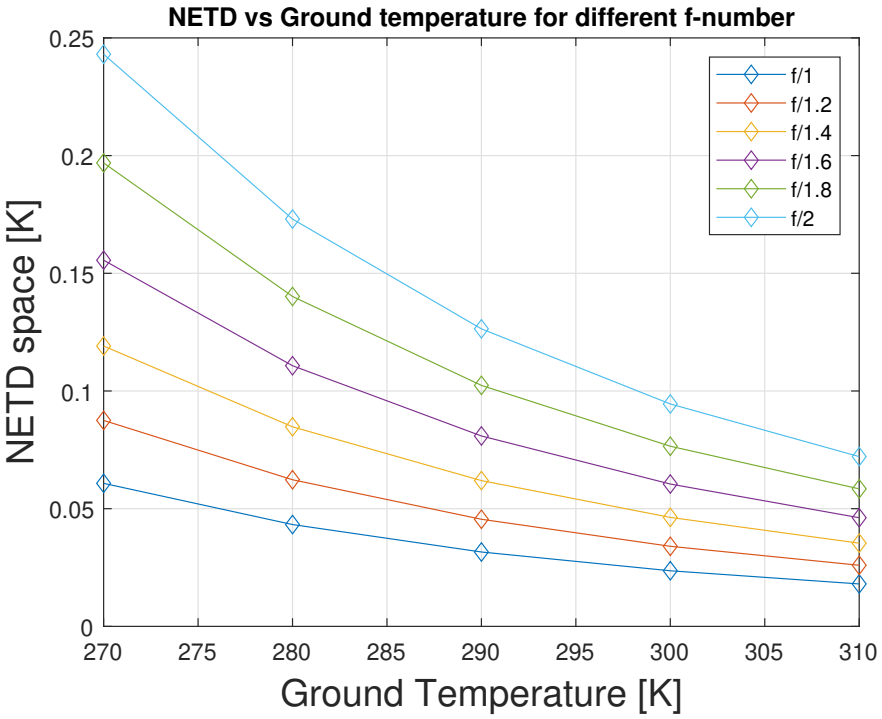

Figure 6.8 – NETD vs Temperature for different f-number.For f-number on the ground= 2.0, NETD in the ground= 20 mK, pixel size= 10 μm and the wavelength range between 3.7-4.8 μm.

The results from the parametric study show that as low as the f-number is, a better temperature is achieved as NETD decreases along with the f-number. As the temperature increases, the NETD starts to show an asymptotic behaviour around 0.

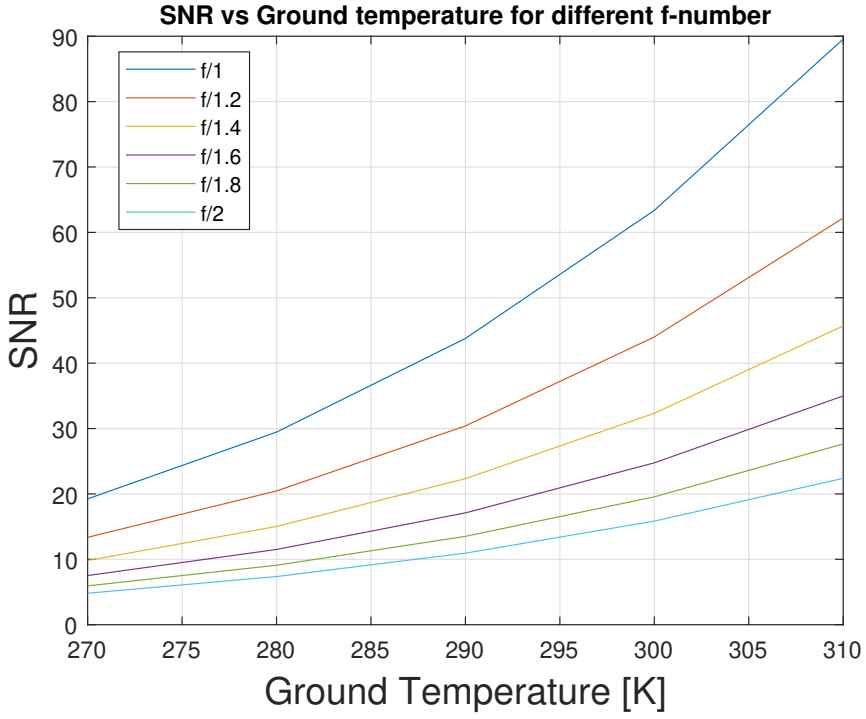

Figure 6.9 – SNR vs Temperature for different f-number. For f-number on the ground= 2.0, NETD in the ground= 20 mK, pixel size= 10 μm and the wavelength range between 3.7-4.8 μm.

The SNR shows an increase with the decrease of f-number, which means that for lower f-number the quality of the image obtained will be higher.

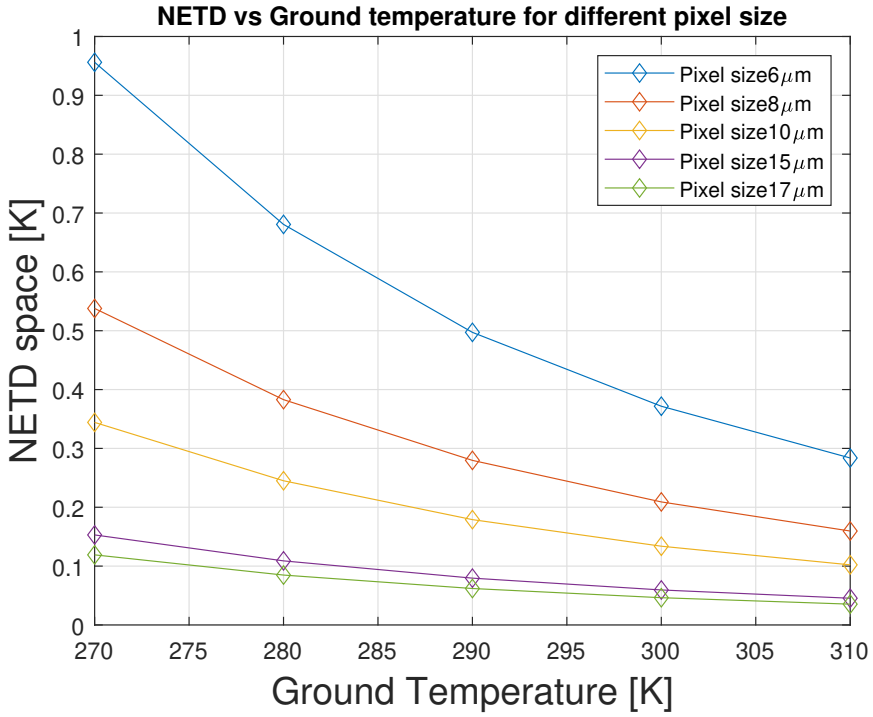

Figure 6.10 – NETD vs Temperature for different pixel size. For f-number in space= 1.4, f-number on the ground= 2.0, NETD in the ground= 20 mK and the wavelength range between 3.7-4.8 μm.

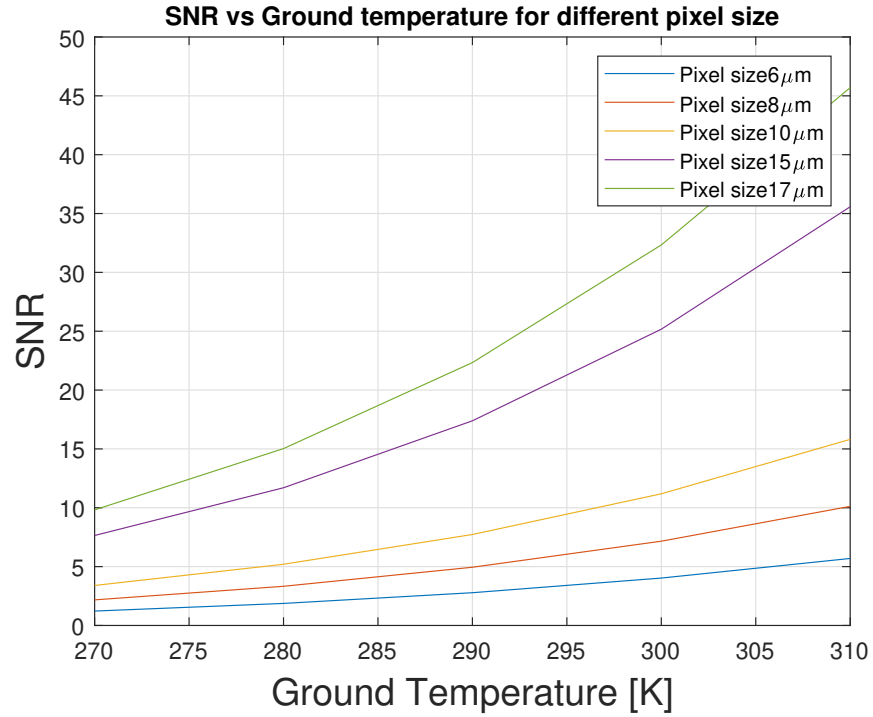

Figure 6.11 – SNR vs Temperature for different pixel size. For f-number in space= 1.4, f-number on the ground= 2.0, NETD in the ground= 20 mK and the wavelength range between 3.7-4.8 μm.

For the pixel size variation, the effect is the inverse, for a larger pixel size the values of NETD and SNR improve. Therefore, the same approach must be taken as in the pre-sizing, a trade-off between pixel size and f-number must be made.

6.2.2 Times

Time as seen in section 2.8.1 is fundamental to have a good acquisition of the desired scene. As already mentioned, the integration time depends on the GSD and the velocity of the satellite, knowing, for example, that the orbit of the satellite is 500 km and that the desired GSD of 20 m, it is possible to calculate the integration time for those parameters using Equation 2.19:

$$t_i = 0.0028[s]$$

For the photodetectors this does not suppose a problem because the response time is of the order of μs but for thermal detectors with a much longer response time it could suppose an issue to expose that it is presented the next graph that relates the integration time related to the GSD and the response time computed in the same graph for both microbolometers selected (Table 3.1). In this plot, they are also added the response time of the best case scenario for the thermal time constant and the worst case scenario, which are, respectively, 7 and 16 milliseconds [8]. For the microbolometer selected from the list, the thermal time constants are 12 ms for the VO_x Imager BB, and 14 ms for the Bird 640 [16]. Just to remind, as explained in section 2.8.1, the thermal time constant is the time necessary to obtain 63% of the output signal, so that the response time is the time necessary to obtain the 95% of the signal, which corresponds to three times the thermal time constant. With that being said, here is presented the integration time for both microbolometers, the best and worst case scenario times :

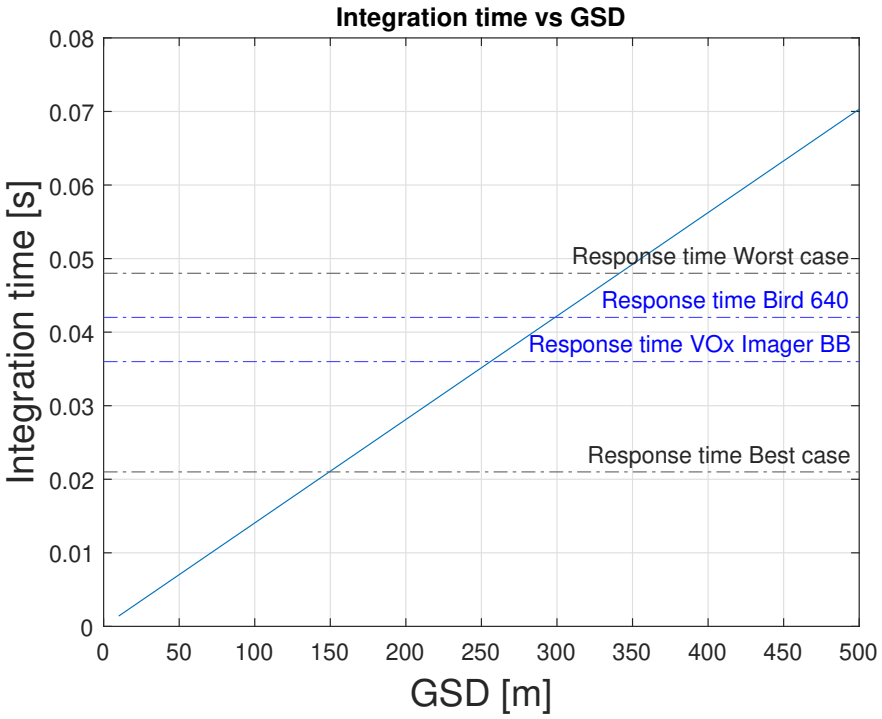

Figure 6.12 – Integration time vs GSD.The response time of the microbolometers selected to study (thermal time constants of 12 and 14 ms) is also plot alongside the best and worst case scenario corresponding to values of 7 and 16 ms of thermal time constants [16].

It shows that is necessary to have at least a GSD of 250 m in order for the integration time to be long enough to allow the response time of the detector to occur for a single GSD. This as

noticed is an order of magnitude superior to the required spatial resolution, so it is necessary to implement a solution to be able to use a microbolometer for a mission in the MWIR. As the thermal time constant is defined by the manufacturer and limits the response time, the already mentioned solutions of TDI and satellite slow-down factor should be implemented to avoid the long response time problem for the microbolometers.

Along with the implementation of an ADCS system to perform the slow down factor and the TDI, it should be made a computation of the point accuracy needed to result in a good receiving signal because if not the pixel could capture radiation from other pixels and not the radiation from the desired point of interest. The ADCS should be made probably with three-axis reaction wheels and three-axis magnetorquers as the actuator and a star tracker as the sensor, as are the more reliable ones in terms of accuracy and mission tested and provide stabilization for the 3-axis and zero momentum. Supposing a scenario in which the detector has 64 pixel rows for integration (TDI) and the pointing stability during the integration has been established at 10% error of the pixel. By setting these parameters and considering the GSD= 20 m and the altitude of the orbit = 500 km, it is possible to find that the pointing accuracy for the pitch should be as follows:

$$t_{exposure} = \frac{n_{lines} \cdot GSD}{V_{sat}} = 181.303[ms] \tag{6.1}$$

Then, the GSD angle of each pixel has to be:

$$\theta_{pixel} = tan^{-1}\left(\frac{GSD}{h}\right) = 8.251[arcsec] \tag{6.2}$$

The requirement of stability and accuracy was set to be a 10% of error so it is:

$$\omega_{pitch} = 0.1\frac{\theta_{pixel}}{t_{exposure}} = 4.551[arcsec/s] \tag{6.3}$$

That is the stability requirement for the optical system and that should be provided by the ADCS to ensure a correct capturing of the desired scene when performing the TDI plus the slow down of the spacecraft.

6.2.3 Detector comparison

To compare the detectors, there has been established that the wavelength range to study is from 4.4 up to 4.8 μm in order to avoid the perturbations that may be caused by the albedo at low to medium ground temperatures. Additionally f-number in space is set at 1.4. The other parameters are set the same as in the parametric study. The fill factor is supposed at 0.75 and the transmittance of the optics is supposed to be 0.9. The altitude of the satellite is 500 km and to simplify the problem also has been considered an atmospheric transmittance of 0.614. The range of temperatures will be tested for three different scenarios, one for low temperature from 270-310 K, one for medium temperature range from 310-370 K, and the last one for high temperature range 370-1000 K. The type of soil is set to be cropland.

In the section A are presented the values at different temperatures 270, 310, 370, and 1000 K. It is worthy to say that the detector with the best specific detectivity is the SuperHawk from Leonardo, followed by the Hexablu 6 from Leonardo DRS and Blackbird 1920 from SCD. The worst detectors in terms of detectivity are the Bird 640, Pelican-D and VO_x Imager BB, both three from SCD. Meanwhile, the results for the NETD are quite good, however, the values for SNR are relatively low, especially in low temperatures, which could affect the quality of the image. To obtain the values in A, it has been used Equations 2.12, 2.15 and 2.18. It has been

considered also that the frame rate of the detector is at 60 Hz to compute the value for specific detectivity.

6.2.3.1 NETD

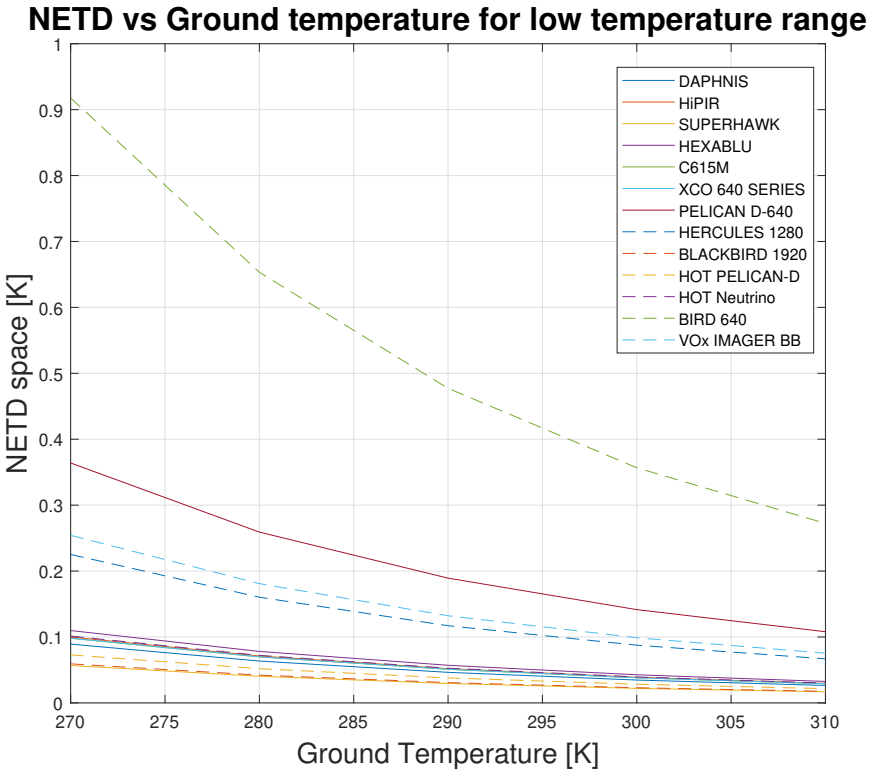

Figure 6.13 – NETD vs temperature for the different selected detectors at a low temperature range 270-310 K. f-number in space= 1.4, wavelength range 4.4-4.8 μm, transmittance of the optics= 0.9, fill factor= 0.75 and h= 500 km. Each parameter values can be checked in Tables 3.1 and 3.2.

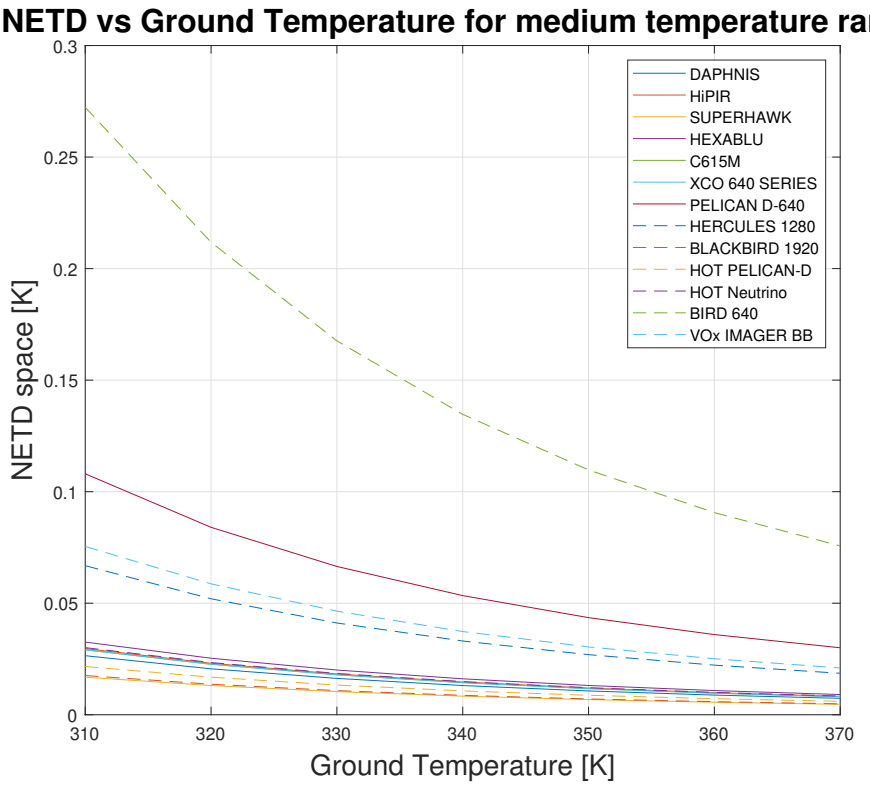

Figure 6.14 – NETD vs temperature for the different selected detectors at a medium temperature range 310-370 K. f-number in space= 1.4, wavelength range 4.4-4.8 μm, transmittance of the optics= 0.9, fill factor= 0.75 and h= 500 km. Each parameter values can be checked in Tables 3.1 and 3.2.

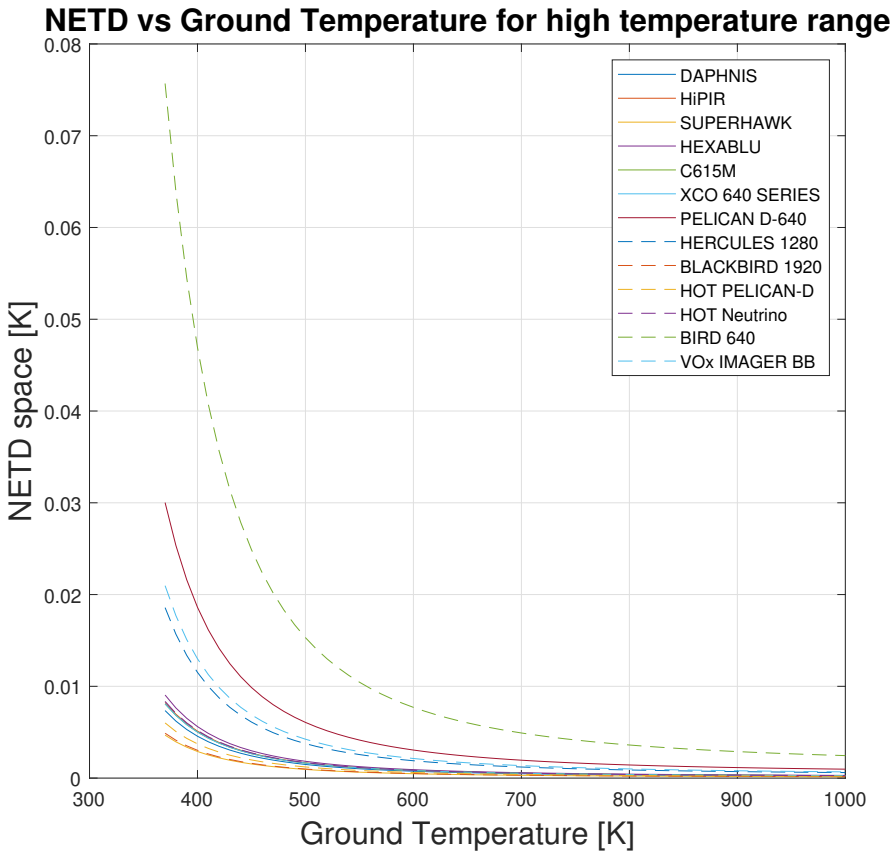

Figure 6.15 – NETD vs temperature for the different selected detectors at a high temperature range 370-1000 K. f-number in space= 1.4, wavelength range 4.4-4.8 μm, transmittance of the optics= 0.9, fill factor= 0.75 and h= 500 km. Each parameter values can be checked in Tables 3.1 and 3.2.

In terms of the NETD, the values are inversely proportional to the temperature of the ground. The reason is that for higher temperatures there is a higher incoming signal, so the difference between the detectors for higher temperatures is almost negligible. The best temperature resolutions for the selected detectors are SuperHawk Infrared Detector from Leonardo, Blackbird 1920 from SCD and HOT Pelican-D from SCD as well. The problem with the last one is that there can not be considered because the range selected for the study is from 4.4 up to 4.8 μm in order to avoid perturbations caused by the albedo. Therefore, the following detector in terms of temperature performance is Daphnis HD MW from Lynred. The material of the FPA in this detector is either HgCdTe or InSb as anticipated in previous sections. On the other hand, the two microbolometers VO_x Imager BB, and Bird 640 are the ones with the worst performance along Hercules 1290 and Pelican D-640, all four from SCD, which also work in the SWIR so that is why they have a worse performance.

6.2.3.2 SNR

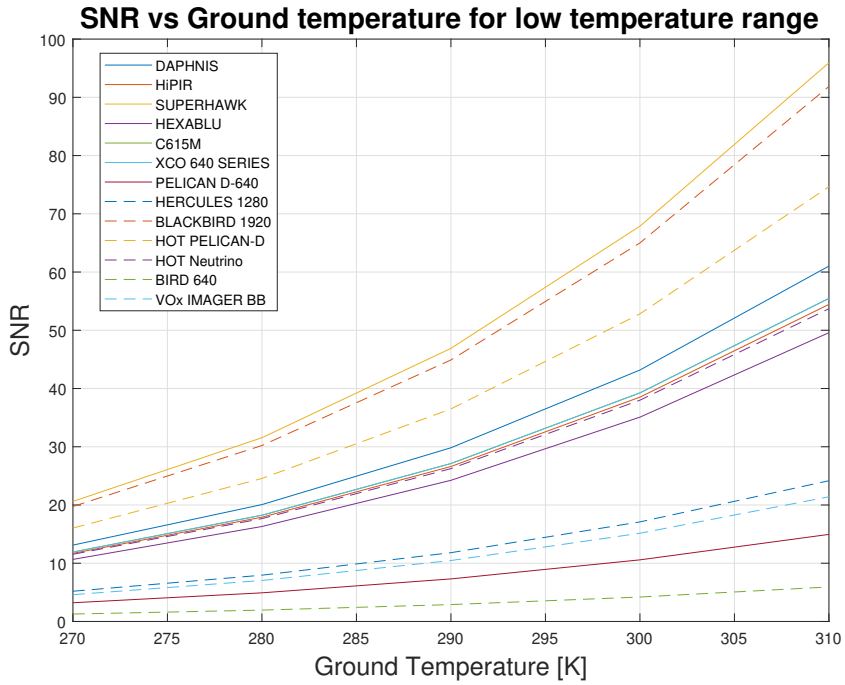

Figure 6.16 – SNR vs temperature for the different selected detectors at a low temperature range 270-310 K. f-number in space= 1.4, wavelength range 4.4-4.8 μm, transmittance of the optics= 0.9, fill factor= 0.75 and h= 500 km. Each parameter values can be checked in Tables 3.1 and 3.2.

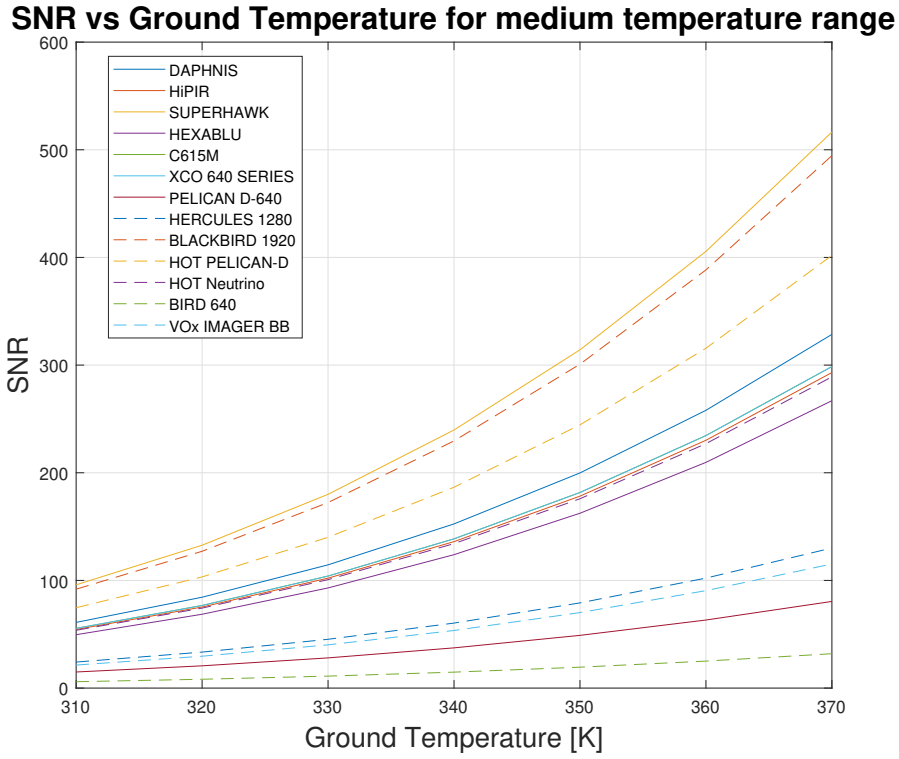

Figure 6.17 – SNR vs temperature for the different selected detectors at a medium temperature range 310-370 K. f-number in space= 1.4, wavelength range 4.4-4.8 μm, transmittance of the optics= 0.9, fill factor= 0.75 and h= 500 km. Each parameter values can be checked in Tables 3.1 and 3.2.

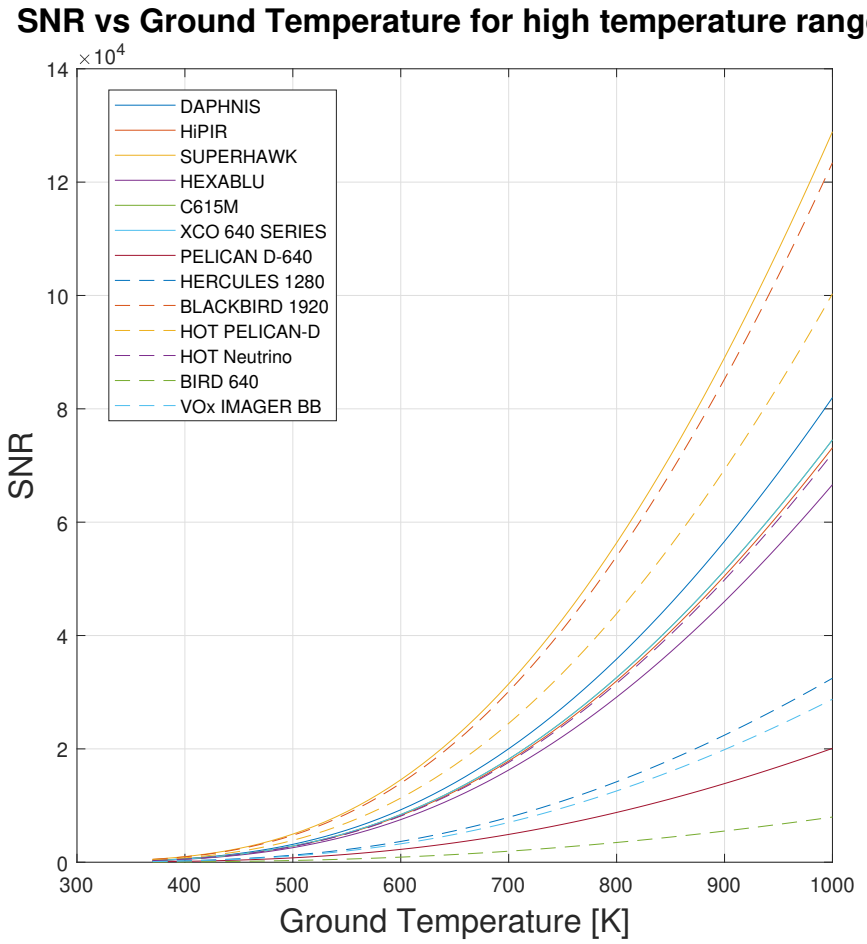

Figure 6.18 – SNR vs temperature for the different selected detectors at a high temperature range 370-1000 K. f-number in space= 1.4, wavelength range 4.4-4.8 μm, transmittance of the optics= 0.9, fill factor= 0.75 and h= 500 km. Each parameter values can be checked in Tables 3.1 and 3.2.

For the SNR in the space environment, considering as well an f-number of 1.4, SNR increases as the temperature increases for the same reason as the NETD reduces, more radiation is received by the detector, thus the signal is better. This has been demonstrated also in the radiometric simulation section. The same results can be concluded as for the NETD, the best performance detectors are SuperHawk, Blackbird 1920 and Daphnis HD MW and the worst are the microbolometers plus the detectors that also work in the SWIR.

6.2.3.3 Photon detector vs Thermal detector vs LWIR

Conditions for this study are repeated, f-number in space is set at 1.4. The other parameters are set the same as in the parametric study. The fill factor is supposed at 0.75 and the transmittance of the optics is supposed to be 0.9. The altitude of the satellite is 500 km and to simplify the problem also has been considered an atmospheric transmittance of 0.614.

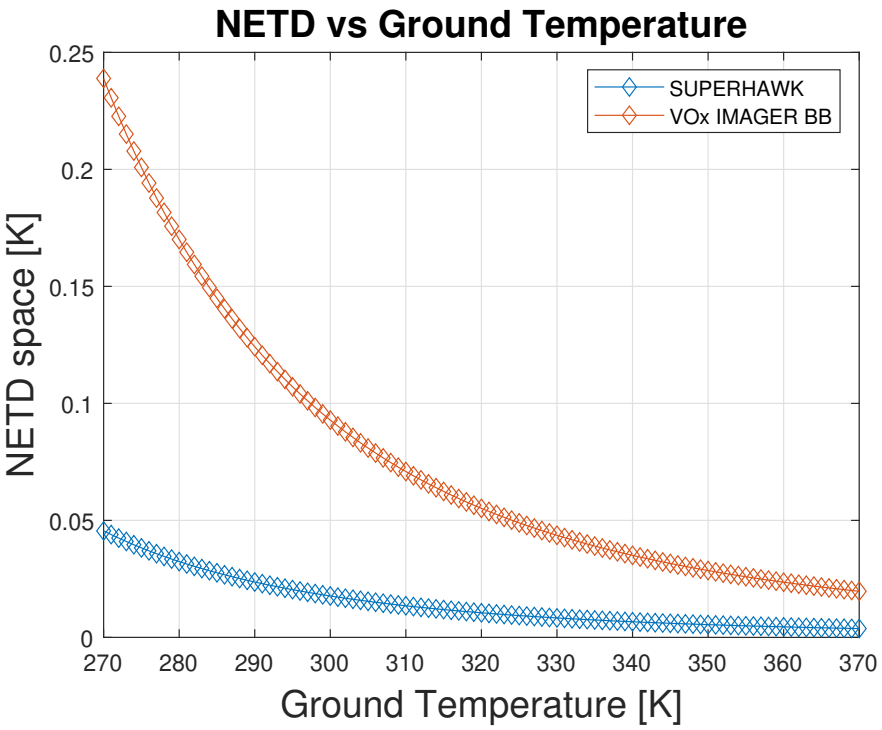

Figure 6.19 – NETD vs Ground Temperature for a photon detector and a thermal detector. f-number in space= 1.4, wavelength range 4.4-4.8 μm, transmittance of the optics= 0.9, fill factor= 0.75 and h= 500 km. Each parameter values can be checked in Tables 3.1 and 3.2.

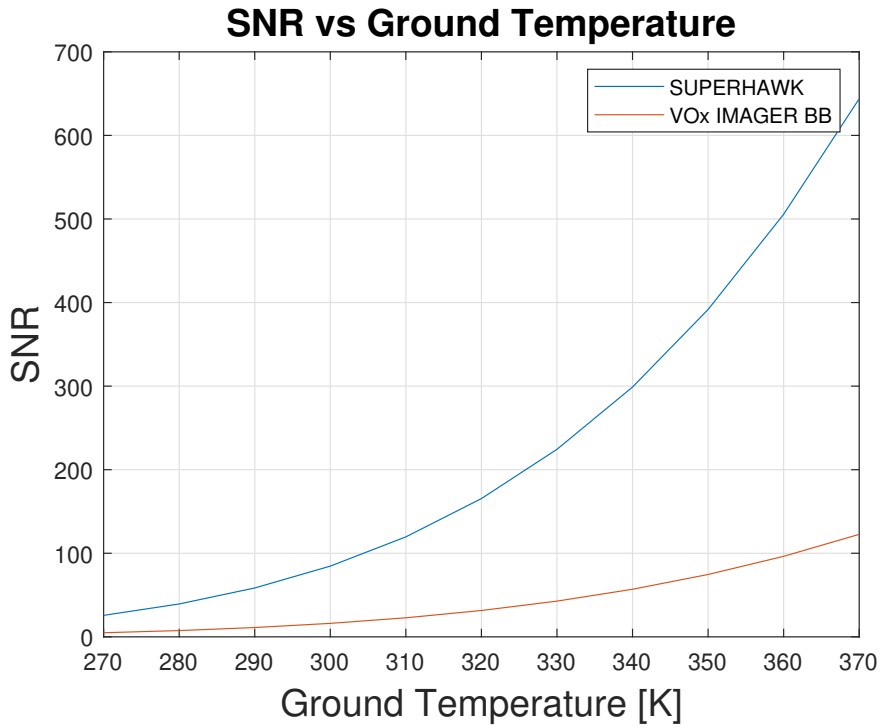

Figure 6.20 – SNR vs Ground Temperature for a photon detector and a thermal detector. f-number in space= 1.4, wavelength range 4.4-4.8 μm, transmittance of the optics= 0.9, fill factor= 0.75 and h= 500 km. Each parameter values can be checked in Tables 3.1 and 3.2.

In the comparison between the thermal detector and photon detector, it is more clear now in

a direct comparison that the capabilities of the photon detector are much better than the ones of the microbolometer. Especially, for low temperatures, the difference is quite evident in the NETD. However, for example, for the SNR it does not suppose so large handicap because both detectors have a low value for low temperatures and even though the gap increases for higher temperatures, the SNR for the microbolometer is good enough so it is possible to work with. In addition, for high temperatures the gap for the NETD is not that critical, which overall it leads to conclude that as for high temperatures the signal is stronger, the difference in the sensitivity and performance for the two different technologies is not so big.

Although it is not in the scope of the project to study the LWIR detectors, a little comparison was made to observe the difference between both IR bands performance under the same optics. In this study is performed again with the f-number set at 1.4. For the LWIR computation of the performance of the detector, the emissivity of the Earth, it has been set at a value of 0.9812 for the wavelength range between 8 to 14 μm. The atmospheric transmission in the LWIR is set in 0.902. The detector chosen in the LWIR to compare with is a T2SL detector named Pelican-D LW from the company SCD. It shows a very good performance even in terms of thermal resolution. The values of the detector are pixel size= 15 μm, f-number in the ground= 1.6, NETD in the ground= 15 mK and is studied in the range 8-9.3 μm.

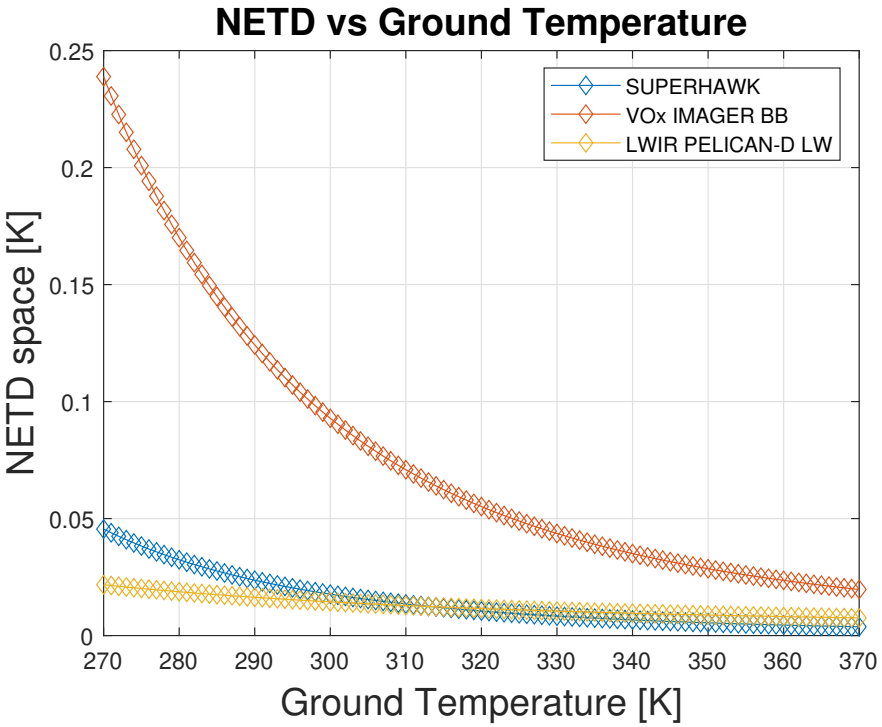

Figure 6.21 – NETD vs Ground Temperature comparison with a LWIR detector. Common values are f-number in space= 1.4, wavelength range 4.4-4.8 μm for the MWIR, transmittance of the optics= 0.9, fill factor= 0.75 and h= 500 km. Each parameter values for the MWIR can be checked in Tables 3.1 and 3.2. For the LWIR detector the values are pixel size= 15 μm, f-number in the ground= 1.6, NETD in the ground= 15 mK and is studied in the range 8-9.3 μm.

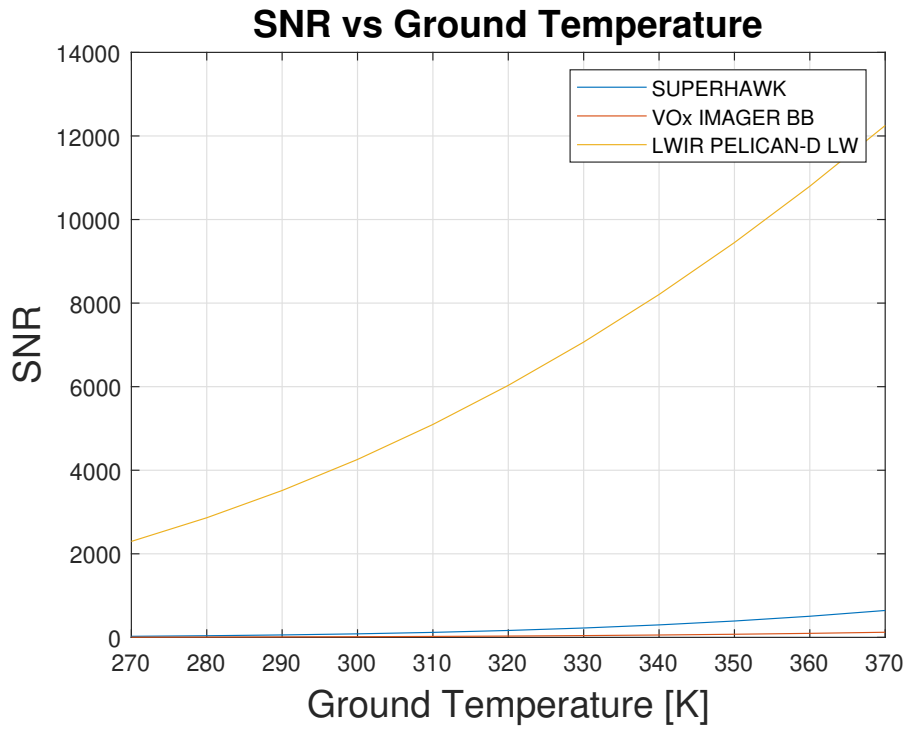

Figure 6.22 – SNR vs Ground Temperature comparison with a LWIR detector. Common values are f-number in space= 1.4, wavelength range 4.4-4.8 μm for the MWIR, transmittance of the optics= 0.9, fill factor= 0.75 and h= 500 km. Each parameter values for the MWIR can be checked in Tables 3.1 and 3.2. For the LWIR detector the values are pixel size= 15 μm, f-number in the ground= 1.6, NETD in the ground= 15 mK and is studied in the range 8-9.3 μm.

From this comparison, it is clearly that in terms of SNR, the LWIR receives a much better signal compared to the ones in the MWIR, three orders of magnitude better, this is because between other reasons the atmospheric transmittance for the LWIR is much larger, so it allows a major radiation incidence in the detector. Furthermore, in terms of temperature resolution, the results for the MWIR and the LWIR are not that different because at 310 K at room temperature are almost the same only with the photon detectors, as the thermal detector still shows a worse performance. Thus, for the temperature resolution, the performance of the MWIR compared with the LWIR is similar, meanwhile the SNR is very much worse. It is important to state that normally the temperature resolution of MWIR is better than the LWIR detector in this case, although the LWIR detector shows an excellent performance and that is the reason it is better at lower temperature than the MWIR but is needed to say that is an exception and not the common trend.

6.3 Conclusions

6.3.1 Mission Requirements

To decide for which detector may be used in each of the three proposed missions (maritime vessel tracking, humidity of croplands monitoring, and wildfire surveillance), it must be set some requisites and constraints to obtain which values of temperature resolution and SNR are needed.

There has been done a search for a mission with similar requirements and there has been found two which can be used as a guideline. The first one was the MISTIGRI mission, which its objective was to monitor the water conditions of agricultural crops and natural vegetation. For

this objective, the requirement set for the TIR was to have NETD between 0.2 to 0.6 K and a SNR for the VNIR between 70 and 180 for the worst radiance received [6]. Another mission, the European Remote Sensing Information Service, ERSIS mission, had a NETD requisite between 0.1 K and 0.5 K for crop hydric stress. The spatial resolution of this TIR instrument was 200 m. The ERSIS satellite was also used for fire detection for which the NETD requirement was only between 1.5 K and 2 K since the signal captured is much higher [47].

The mission proposal which has no guidelines is the maritime vessel tracking but taking into account that as the temperature in the sea is really low compared to the vessels installed in the boats, as a minimum temperature coming from the crew or the engine can be noticed compared to the temperature background it is possible to estimate that the NETD requirement would be the same as for the fire detection between 1.5 and 2 K.

6.3.2 Final choice

From this section, it is possible to conclude that in terms of pre-sizing, to obtain a good GSD, around 20 m, it is necessary to have a large optic diameter, a low f-number and a large pixel size as well. As there is no size restriction, it is assumed that the diameter can be as large as necessary, so it can be set around 200 mm, this being fixed and following the marked guidelines from previous sections, the f-number can be fixed at 1.4 (see figure 6.1), just to not have to design a really complex optics, meanwhile pixel size can vary from 10 μm to 15 μm (see figure 6.4).This is because of the aberration problem as a low pixel size can be a problem in terms of diffraction limit as the spot size from the signal received could be bigger than the actual pixel size. Therefore, by blocking these parameters and coming back to size, this should translate into at least a 3Ux2U size (see figure 6.7), which means that the optical system of the satellite is 6U. Thus, the CubeSat designed to contain this system should be larger as it requires also all subsystems that support the optical payload. A suitable size for the CubeSat could be 12U depending on the other systems.

Moreover, starting to choose the best fit for each proposed mission starting with the humidity monitoring of the crops, for these missions, the range of ground temperature is set around 270 up to 310 K for these ranges of temperatures only two detectors are close to the requirement imposed for a value of 70 for the SNR, the SuperHawk Infrared Detector from Leonardo and the Blackbird 1920 from SCD. The thermal resolution requirement is accomplished by all detectors except the Bird 640 and the Pelican-D 640, both from SCD . So between both detectors, the pixel size of the Blackbird 1920 is more adequate to the requirements established at 10 μm because for the SuperHawk with 8 μm pixel size, may have problems with the diffraction limit and some solution may be implemented to avoid it as the pixel binning, which is also possible. The pixel binning consists of grouping together multiple pixels to avoid problems with the diffraction limit and decreasing the read-out and exposure times but sacrificing spatial resolution and with the limitation that the detector pixel resolution must be high enough. In terms of size, Blackbird 1920 is a little larger but has a better pixel resolution. Thus, for the humidity monitoring of the crops the choice is to have the Blackbird 1920.

For the proposed mission of wildfire detection and tracking, the temperature requirements vary as little as they comprise from 310 K up to 1000 K, when the point of interest is the wildfire itself. In this case and the following requirements of the previous subsection for the temperature resolution requirements, all detectors except the two again meet these constraints. For the SNR, even though it is lower than the proposed requirement images, around 20-50 SNR are useful in the MWIR [49], although the quality of the definition of the image is quite worse. With this being said for this mission, the choice is the VO_x Imager BB, which for the temperature range

has the SNR value mentioned before and offers multiple possibilities as it can work in the LWIR band too, the size and operating temperature are good advantages as well. The only major drawback is that it has to be applied to the TDI technique plus some attitude control systems, as the resolution time of the microbolometer is too long for the GSD required. The TDI can be avoided if the GSD required is sacrificed by an order of magnitude, but this being one of the main objectives of the mission for now is rejected.

Then, for the mission concerning maritime vessel tracking as it is not demanding as humidity monitoring, it has been taken the same approach as for the wildfire tracking so that the SNR is a minor constraint so it is opted for a reasonable and more size favoured option as the Daphnis HD MW from Lynred. This choice is made constraining the size of the optical system as the mission is not so demanding in terms of sensitivity and the Daphnis HD MW is still a very good option in terms of temperature resolution and SNR.

Just to be clear, the type of soil has not been changed because as the radiometric study has shown, the ground emissivity for each type of landscape is almost the same in the MWIR, so in this case it has not been considered a key parameter to modify and analyze the results that would be practically the same.

In addition, it is possible to consider an scenario in which the GSD should not be such a constraint as, for example, the proposed missions of humidity monitoring of croplands or wildfire tracking, because the targeted scenes are big enough so that the spatial resolution can be relaxed. Not so for the maritime vessels as the targets are quite small,thus the requirement of spatial resolution is maintained. If GSD is relaxed up to 50 m for cropland monitoring and up to 100 m for wildfire tracking, it can be approached in two different ways. The first one should translate in a reduction in the maximum diameter of the optics and in the satellite as well, especially in the length, because although the diameter is reduced, the measures of the detector prevail, this approach is if the f-number, 1.4, and the pixel size, 10 μm, are maintained. For a GSD of around 40 m, the diameter can be down to 100 mm, half of the proposed diameter and down to 50 mm with a GSD around 80 m (See Figure 6.1 and 6.4). The other approach is to maintain the diameter size, 200 mm, the length of the optics, and modify the f-number or the pixel size. In this case, as it shows Figure 6.10 and 6.11 the parameter to modify would be the pixel size by increasing it up to 17 or 20 μm as in the market there are few detectors with a larger pixel size than that. By doing so, with a diameter of 200 mm, f-number of 1.4, and a pixel size equal to 20 μm GSD would be around 50 m, with a better value in NETD and SNR. Thus, by sacrificing in spatial resolution, it could return to an improvement in the sizing or in the performance of the detector. Furthermore, by increasing the GSD it would affect also the integration time of the satellite, which would be longer but still insufficient for detectors with a long response time (see Figure 6.12).

Overall, it has been seen that for accomplishing the requirements of the proposed mission it has to have a complex optics and a large optical system in terms of nanosatellites. This sacrifice in sizing has been made based on the assumption that the space mission should be more affordable in the near future so that it is possible to achieve those measures. Concerning the SNR, for the MWIR, the value is quite low and thus the quality of the images taken is worse than the ones in the LWIR, for example. Nevertheless, the MWIR excels in some points for high temperature missions as the performance is better than LWIR detectors, so it is still a large gap where they can be used.

7 Conclusions

The main objective of this Thesis is to understand in which situation is a feasible a mission using a MWIR detector. MWIR detectors have been underused in space missions and especially in CubeSats and nanosatellites, although they offer several situations in which their use is feasible and improves the performance of detectors with more extended use as the LWIR.

A proposal of a mission was made, which goal was to carry out an in-orbit demonstration of the MWIR technology to further implement a constellation of MWIR satellites. Some of the proposed requirements of the mission were:

- Daily revisit.
- MWIR with two channels.
- GSD around 20 m.
- Temperature difference better than 2 K.

With this in mind, there were planned some guidelines to follow to achieve the required characteristics of the detector to comply with the previous requirements. First of all, there was thought three different mission scenarios in which apply the MWIR technology, the proposed missions were cropland humidity monitoring, wildfire tracking and surveillance, and finally maritime vessel tracking. Later on, there would be introduced more significant figures of merit to determine the performance and possible constraints that could affect their use. Then, different detectors would be studied, which are available in the market and understand which one adapts better to the proposed mission requirements and in which situations, producing a trade-off between the advantages and disadvantages of choosing one detector or another, making special attention to the differences between photodetectors and thermal detectors.

In the side of optics, the most important parameters that would be pivotal in the study will be the f-number, the diameter of the optics, the pixel size of the array, and and the GSD, the spatial resolution. Through determining those parameters, it would be possible to determine the detectivity, another key figure of merit, which is very useful due to the fact that it does not depend on the altitude of the orbit and will be used to compute the values of the temperature resolution, NETD and SNR, which will give a value for the sensitivity of the detector towards the mid-wave infrared wavelength range. Important to mention that there are some constraints that may affect the choice as the diffraction limit could suppose a problem in terms of aberration of the result image, and the response time needed for the detector should be short enough to happen when the satellite passes by a GSD area. The quantum efficiency would also be a parameter to take into account when selecting the required detector.

Later on, it was carried out a comparison between the technologies of thermal and photodetectors. From there, it was concluded that the major drawback of photodetectors is that they need to operate at a really low temperature so that they need to be cooled down by a cryocooler, with the consequences that may carry in terms of power consumption, sizing and vibration issues. On the other side, the thermal detectors offer a worse overall performance and a longer response time, but they operate at room temperature, are smaller, and they are not affected by the quantum efficiency or the cut-off wavelength. For each technology, the most widespread material is InSb and HgCdTe for the photoconductors, they have the best quantum efficiencies and are more developed. Meanwhile, for the thermal detectors, VO_x microbolometer has the largest market share and overall features. Then, it has been made a market study pointing out

suitable detectors that fit into the mission requirements, this search has been done by focusing on some parameters, it has been chosen the detectors with already low f-number tested, a good enough NETD, a low pixel size that accounts both for the required spatial resolution and to avoid the diffraction limit aberration. Moreover, the pixel resolution limit was set at 640x480 pixels in Figure 7.1, as for low pixel resolution, the different objects studied in the desired scene could not be distinguishable due to low pixel resolution, especially in a space mission scenario. Additionally, it is important to have a sufficient number of pixels so it is possible to zoom in the image if needed or perform pixel binning if necessary.

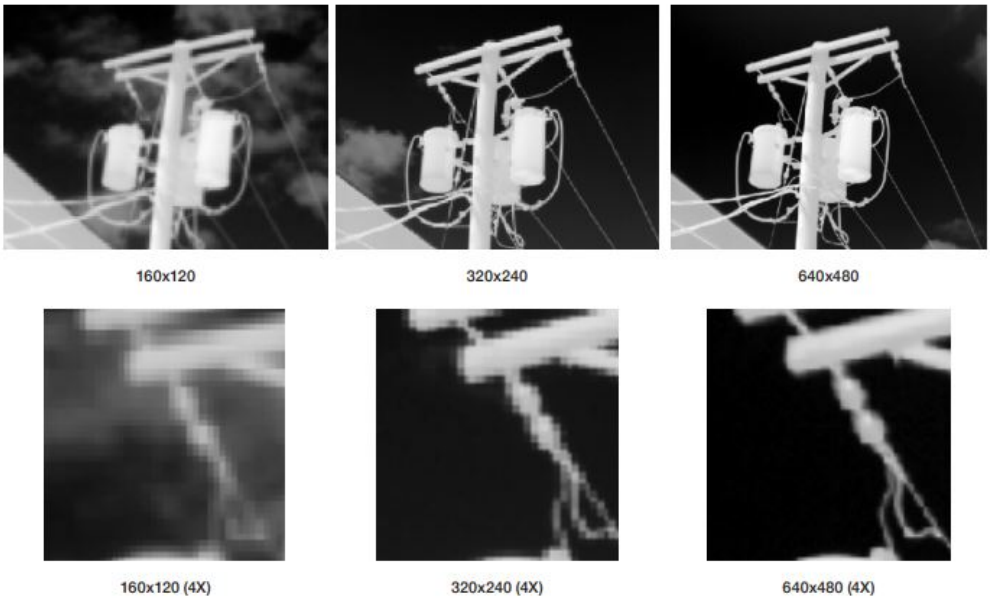

Figure 7.1 – The importance of pixel resolution. [48].

The list of the final detectors selected and their characteristics is found in Table 3.1 and 3.2.

In addition, as they are proposed three different mission scenarios, it is required to perform a radiometric simulation of three different conditions, which are affected by the targeted ground temperature and the type of soil because of the emissivity and albedo. Following a radiometric model based on [8], which takes into account the two major sources of radiation, the Earth's ground emission and the albedo reflected by Earth's ground, considering also the atmospheric transmittance in both cases. The conclusions of the simulation showed that ground emissivity was not a crucial factor as the emissivity is high for all types of soil, even water and ice and that the incident radiation is higher in high temperature situation. Moreover, it was proved that MWIR detectors have a higher power per pixel than the LWIR for high ground temperatures, which enables the MWIR detector to have a better performance when monitoring high temperatures on the ground.

Furthermore, to prove that this type of mission and the detector selected are a real and feasible option, it was surveyed the missions past, present, and future for CubeSats and nanosatellites which carry MWIR payload. Of those, the most interesting ones were already past mission Arkyd 6A, which in terms of size and spatial resolution resembles the requirements of the proposed mission and the target of the mission of humidity monitoring, what it means that the targeted values are achievable and not utopian. Then, the other interesting future mission is the eve-1, because of the fact that they include a microbolometer as the payload acting in the MWIR and LWIR, achieving a reduced size when compared to the other CubeSats which carry MWIR payloads and is the first CubeSat in the MWIR to include a thermal detector so it is

interesting to see how it turns out, also interesting for the comparison with the proposed mission of wildfire tracking which has the same objective.

Finally, there were studied the performance and pre-sizing of the detector by following the model [9] based on the NETD and SNR for the performance and another model to study how the GSD requirement affects the size of the detector. The parameters which were fixed to choose the different detectors were especially the GSD and NETD. Spatial resolution is pivotal to differentiate the different elements when observing an area to see an example as it is presented in Figure , for example, for the maritime vessel tracking and humidity monitoring which can resemble to the images in the Figures 7.2 and 7.3, it shows that for a 100 m GSD it is nearly impossible to distinguish the boats in the bay, On the other side, even though is hard to differentiate is possible to see the river streams flowing from the lake so it may be feasible to use in a mission like the humidity monitoring where it is not needed high detail.

Figure 7.2 – (a) GSD = 15 m Reconstructed image from Landsat 7 & 8 panchromatic band (b) GSD = 100 m Reconstructed image from Landsat 8 Thermal infrared bands. Both from San Francisco [50].

Figure 7.3 – (a) GSD = 20 m Reconstructed image from Sentinel-2 bands 5, 6, 7, 8a, 11, and 12 (b) GSD = 100 m Reconstructed image from Landsat 8 Thermal infrared bands. Both from lake Pukaki in New Zealand [50].

With this being said, the other important parameter to take into account was the NETD, which accounts for the temperature resolution. Following the guidelines of similar missions [6] [47], it was required for the mission of humidity monitoring, the NETD has to be around 0.1 and 0.5 K because it is the most demanding one and for the other two as the temperature difference between the background and the element of interest is higher the temperature resolution was considered lower around 1.5 and 2 K. In terms of the SNR, it was targeted to an SNR of around 70, but it was considered acceptable between the range of 20 up to 50 [49]. For a daily revisit it was considered that for an altitude of around 500 km it was enough to achieve that [51]. A summary of the mission requirements and detector choices for each one is found in Table 7.1:

Mission	Maritime Vessel Tracking	Wildfire Tracking & Surveillance	Cropland Humidity Monitoring
NETD required (K)	1.5 - 2		0.1 - 0.5
SNR required	target 70, acceptable 20-50		
Orbit Altitude (km)	500		
Type of soil	Water body	Natural Vegetation Mosaic	Croplands
GSD (m)	20		
Targeted Ground Temperature (K)	270-310	310-1000	270-310
Detector			
Name	Daphnis HD MW	Vox Imager BB	Blackbird 1920
Material	HgCdTe	Vox microbolometer	InSb
Spectral range (μm)	3.7 - 4.8	3.0 - 14	3.6 - 4.9
f-number ground	f/2	f/1.9	f/3
NETD ground (mK)	20	35	25
Maximum diameter optics (mm)	200		
f-number space	1.4		
Size Optical System (mm)	200x283	200x283	200x314
Size FPA (pixel x pixel)	1280 x 720	640 x 480	1920 x 1536
Pixel size (μm)	10	17	10
NETD space (K)	0.09 - 0.018 (@ 270 - 310 K)	0.075 - 6.79E-04 (@ 310 - 1000 K)	0.06 -0.018 (@ 270 - 310 K)
SNR space	13.11- 61.02 (@ 270 - 310 K)	21.41 - 2.88E+04 (@ 310 - 1000 K)	19.74 - 91.85 (@ 270 - 310 K)
Detectivity (W^{-1})	1.09E+14	1.33E+13	1.64E+14
Specific Detectivity ($m \cdot Hz^{1/2}/W$)	2.68E+12	4.23E+11	4.03E+12
Quantum efficiency	>70 %	-	85 - 90%
Operating Temperature (K)	Up to 120	300	Approx 80 K

Table 7.1 – Summary of the mission requirements and choices.

Some remarks must be done on the final choices. In the case of maritime vessel tracking and

cropland humidity monitoring, the focal point was the performance of the detector, in terms of SNR, quantum efficiency, and number of pixels, emphasizing in the humidity monitoring that the requirements met were the most demanding. On the other hand, as the conditions of incident power and requirements offer a more relaxed scenario, it was chosen for the wildfire tracking microbolometer as the final option, but with some constraints as the response time of the microbolometer chosen is too long for the integration time that corresponds to the altitude and the GSD, so alongside the detector it must be implemented a ADCS system with a specific accuracy (see Section 6.2.2) that allows the spacecraft to have a longer integration time for the microbolometer and apply as well the TDI technique to obtain a enough quality image. It was thought about the option to sacrifice spatial resolution up to 50 or 100 m, only for humidity monitoring or wildfire tracking, to understand which could be the consequences. The main advantage comes in terms of sizing reduction or the possibility to have not so complex optics, this option was dismissed because the improvement in sizing was not as considerable and one of the previous hypotheses is that there was not limited by sizing, so the spatial resolution remains the same but is still an option to consider.

Future considerations to follow up this work should be to introduce the power consumption requirements of the detector and check if it is feasible and which under circumstances. Moreover, a datalink budget and data handling to figure out how the data process must be carried out. In addition, it could follow up the implications of applying TDI in terms of attitude control and the algorithm implemented to do so. Finally, it could scope how it should be possible to plan a constellation of nanosatellites using MWIR detectors and under which requirements.

To conclude, the purpose of this Thesis was to demonstrate how the proposed missions for MWIR could be done and under what circumstances. It has been clearly proved that it is feasible and that they exist a lot of options were they can be used and improve the performance of LWIR detectors, they have a better temperature resolution and higher sensitivity when monitoring high ground temperatures. It is true that they have a worse sensitivity in remote sensing, the final product is not an image but information which is more than proven that the MWIR detector can provide. Moreover, it has been backed by the fact that they already exist future and past missions which have similar features. Especially interesting is the case of microbolometers which offer the opportunity to monitor the Earth in a larger broadband using both MWIR and LWIR and the advantages of being able to switch from one to another.

A Results

Detector Name	**Wave length range & f-number**	**Detectivity (W^{-1})**	**NEDT (K)**	**Power per pixel (W)**	**SNR**	**Specific Detectivity (m· $Hz^{1/2}$/W)**
DAPHNIS-HD MW RM2/K563	3.7 μm - 4.8 μm f/2.0	1.09E+14	0.09	1.20E-13	13.11	2.68E+12
HiPIR-Engine HOT	3.4 μm - 4.8 μm f/2.2	9.74E+13	0.10	1.20E-13	11.70	2.39E+12
SUPERHAWK INFRARED DETECTOR	3.7 μm - 4.95 μm f/2.8	2.68E+14	0.06	7.68E-14	20.61	5.88E+12
HEXABLU 6	3.4 μm - 4.8 μm f/2.3	2.47E+14	0.11	4.32E-14	10.66	4.68E+12
C615M MWIR MCT COOLED FPA DETECTOR RS046	3.7 μm - 4.8 μm f/2.0	4.41E+13	0.10	2.70E-13	11.92	1.32E+12
XCO 640 SERIES	3.7 μm – 4.8 μm f/2.0	4.41E+13	0.10	2.70E-13	11.92	1.32E+12
PELICAN-D	1 μm – 5.4 μm f/1.5	1.19E+13	0.36	2.70E-13	3.21	3.57E+11
HERCULES 1280	1 μm – 5.4 μm f/2.0	1.92E+13	0.23	2.70E-13	5.19	5.77E+11
BLACKBIRD 1920	3.6 μm – 4.9 μm f/3	1.64E+14	0.06	1.20E-13	19.74	4.03E+12
HOT PELICAN-D 640	3.6 μm - 4.2 μm f/1.5	5.94E+13	0.07	2.70E-13	16.04	1.78E+12
HOT Neutrino Swap C	3.4 μm – 5.0 μm f/2.5	4.27E+13	0.10	2.70E-13	11.54	1.28E+12
Bird 640	3 μm - 14 μm f/1.0	3.67E+12	0.92	3.47E-13	1.27	1.17E+11
VO_x Imager BB	3 μm - 14 μm f/1.9	1.33E+13	0.25	3.47E-13	4.60	4.23E+11

Table A.1 – Results of the performance of the detectors at 270 K.

Detector Name	Wave length range & f-number	Detectivity (W^{-1})	NEDT (K)	Power per pixel (W)	SNR	Specific Detectivity (m· $Hz^{1/2}$/W)
DAPHNIS-HD MW RM2/K563	3.7 μm - 4.8 μm f/2.0	1.09E+14	0.026	5.59E-13	61.02	2.68E+12
HiPIR-Engine HOT	3.4 μm - 4.8 μm f/2.2	9.74E+13	0.030	5.59E-13	54.44	2.39E+12
SUPERHAWK INFRARED DETECTOR	3.7 μm - 4.95 μm f/2.8	2.68E+14	0.017	3.58E-13	95.94	5.88E+12
HEXABLU 6	3.4 μm - 4.8 μm f/2.3	2.47E+14	0.033	2.01E-13	49.59	4.68E+12
C615M MWIR MCT COOLED FPA DETECTOR RS046	3.7 μm - 4.8 μm f/2.0	4.41E+13	0.029	1.26E-12	55.48	1.32E+12
XCO 640 SERIES	3.7 μm – 4.8 μm f/2.0	4.41E+13	0.029	1.26E-12	55.48	1.32E+12
PELICAN-D	1 μm – 5.4 μm f/1.5	1.19E+13	0.108	1.26E-12	14.95	3.57E+11
HERCULES 1280	1 μm – 5.4 μm f/2.0	1.92E+13	0.067	1.26E-12	24.17	5.77E+11
BLACKBIRD 1920	3.6 μm – 4.9 μm f/3	1.64E+14	0.018	5.59E-13	91.85	4.03E+12
HOT PELICAN-D 640	3.6 μm - 4.2 μm f/1.5	5.94E+13	0.022	1.26E-12	74.66	1.78E+12
HOT Neutrino Swap C	3.4 μm – 5.0 μm f/2.5	4.27E+13	0.030	1.26E-12	53.70	1.28E+12
Bird 640	3 μm - 14 μm f/1.0	3.67E+12	0.272	1.61E-12	5.93	1.17E+11
VO_x Imager BB	3 μm - 14 μm f/1.9	1.33E+13	0.075	1.61E-12	21.41	4.23E+11

Table A.2 – Results of the performance of the detectors at 310 K.

Detector Name	Wave length range & f-number	Detectivity (W^{-1})	NEDT (mK)	Power per pixel (W)	SNR	Specific Detectivity (m· $Hz^{1/2}$/W)
DAPHNIS-HD MW RM2/K563	3.7 μm - 4.8 μm f/2.0	1.09E+14	7.36	3.01E-12	328.50	2.68E+12
HiPIR-Engine HOT	3.4 μm - 4.8 μm f/2.2	9.74E+13	8.25	3.01E-12	293.07	2.39E+12
SUPERHAWK INFRARED DETECTOR	3.7 μm - 4.95 μm f/2.8	2.68E+14	4.68	1.92E-12	516.45	5.88E+12
HEXABLU 6	3.4 μm - 4.8 μm f/2.3	2.47E+14	9.05	1.08E-12	266.94	4.68E+12
C615M MWIR MCT COOLED FPA DETECTOR RS046	3.7 μm - 4.8 μm f/2.0	4.41E+13	8.09	6.77E-12	298.64	1.32E+12
XCO 640 SERIES	3.7 μm – 4.8 μm f/2.0	4.41E+13	8.09	6.77E-12	298.64	1.32E+12
PELICAN-D	1 μm – 5.4 μm f/1.5	1.19E+13	30.02	6.77E-12	80.49	3.57E+11
HERCULES 1280	1 μm – 5.4 μm f/2.0	1.92E+13	18.58	6.77E-12	130.09	5.77E+11
BLACKBIRD 1920	3.6 μm – 4.9 μm f/3	1.64E+14	4.89	3.01E-12	494.47	4.03E+12
HOT PELICAN-D 640	3.6 μm - 4.2 μm f/1.5	5.94E+13	6.01	6.77E-12	401.90	1.78E+12
HOT Neutrino Swap C	3.4 μm – 5.0 μm f/2.5	4.27E+13	8.36	6.77E-12	289.08	1.28E+12
Bird 640	3 μm - 14 μm f/1.0	3.67E+12	75.69	8.69E-12	31.93	1.17E+11
VO_x Imager BB	3 μm - 14 μm f/1.9	1.33E+13	20.97	8.69E-12	115.25	4.23E+11

Table A.3 – Results of the performance of the detectors at 370 K.

Detector Name	**Wave length range & f-number**	**Detectivity (W^{-1})**	**NEDT (mK)**	**Power per pixel (W)**	**SNR**	**Specific Detectivity ()**
DAPHNIS-HD MW RM2/K563	3.7 μm - 4.8 μm f/2.0	1.09E+14	0.24	7.51E-10	8.20E+04	2.68E+12
HiPIR-Engine HOT	3.4 μm - 4.8 μm f/2.2	9.74E+13	0.27	7.51E-10	7.31E+04	2.39E+12
SUPERHAWK INFRARED DETECTOR	3.7 μm - 4.95 μm f/2.8	2.68E+14	0.15	4.80E-10	1.29E+05	5.88E+12
HEXABLU 6	3.4 μm - 4.8 μm f/2.3	2.47E+14	0.29	2.70E-10	6.66E+04	4.68E+12
C615M MWIR MCT COOLED FPA DETECTOR RS046	3.7 μm - 4.8 μm f/2.0	4.41E+13	0.26	1.69E-09	7.45E+04	1.32E+12
XCO 640 SERIES	3.7 μm – 4.8 μm f/2.0	4.41E+13	0.26	1.69E-09	7.45E+04	1.32E+12
PELICAN-D	1 μm – 5.4 μm f/1.5	1.19E+13	0.97	1.69E-09	2.01E+04	3.57E+11
HERCULES 1280	1 μm – 5.4 μm f/2.0	1.92E+13	0.60	1.69E-09	3.25E+04	5.77E+11
BLACKBIRD 1920	3.6 μm – 4.9 μm f/3	1.64E+14	0.16	7.51E-10	1.23E+05	4.03E+12
HOT PELICAN-D 640	3.6 μm - 4.2 μm f/1.5	5.94E+13	0.19	1.69E-09	1.00E+05	1.78E+12
HOT Neutrino Swap C	3.4 μm – 5.0 μm f/2.5	4.27E+13	0.27	1.69E-09	7.21E+04	1.28E+12
Bird 640	3 μm - 14 μm f/1.0	3.67E+12	2.45	2.17E-09	7.97E+03	1.17E+11
VO_x Imager BB	3 μm - 14 μm f/1.9	1.33E+13	0.68	2.17E-09	2.88E+04	4.23E+11

Table A.4 – Results of the performance of the detectors at 1000 K.

B Matlab Code

Listing 1 – MWIR parametric study code.

```
%% MWIR
clear all;
close all;
clear clc;

%% Parameters
wav_initial=4.4e-6; %m
wav_end=4.8e-6;       %m
wav_interval=wav_initial:0.1e-6:wav_end; %m  Wavelength
Te_interval=270:10:310;  %K  Temperature of the Earth as a BB
soil=9;  %Type of soil (9=cropland by default)
H=500; %km  Height of the orbit
parameter.transmittance_optics=0.9;  %Transmission coefficient of the
    optics
ff=0.75; %Fill factor
%% Constants
constant.C=1.20173e6; %A/(m^2*K^2) Richardson constant
constant.c=299792458; %m/s Speed of light
constant.k = 1.38064852e-23;  %J/K=m^2*kg*s^(-2)*K^(-1) Boltzmann's
   constant
constant.h = 6.6260704e-34;  %J*s=kg*m^2/s Planck's constant
constant.mu=398600.4418; %km^3/s^2 Gravitational parameter
constant.Qe=1.6021766208e-19; %C Electron electric charge
constant.R_earth=6378; %km Earth radius
constant.w_earth=7.2921159e-5; %rad/s Angular velocity of the Earth

%% OPTICS & DETECTOR CHARACTERISTICS
% Pixel size
Px=10e-6; %m  Pixel size
NETD_gr=20e-3; %K
% Parameters earth-satellite
GSD=linspace(10,500,101);  %m
Te_ground_netd= 300; %K
wav_initial_gr= 3.7e-6; %m
wav_end_gr=5e-6; %m
Ad=(ff*Px)^2;  %m^2  Detective area
f_number = 2;
f_number_space = linspace(1,2,6);

%% INTEGRATION TIME
% Orbital period
a=H+constant.R_earth; %km
T0=2*pi*sqrt(a^3/constant.mu); %s
% Spacecraft velocity
Vsat=(2*pi/T0-constant.w_earth)*a; %km/s
% Integration time
```

```
for i=1:numel(GSD)
ti(i)=GSD(i)/(1000*Vsat); %s
end
t_i_1=20/(1000*Vsat);

for i=1:numel(f_number_space)

[detectivity_double,Power_ground_double(i,:)] = NETD_space(constant,
    parameter,...
wav_initial,wav_end,Te_interval,H,NETD_gr,GSD,f_number,f_number_space
    (i) ...
,wav_initial_gr,wav_end_gr,Te_ground_netd,Ad,soil);

end

for i=1:numel(f_number_space)

%Space
%4.4-5.4
Te_dL_dT = 270:10:310;
dL_dT=differentiate_L_respect_T_44_54(Te_dL_dT,soil);
NETD_space(i,:) = (4*(f_number_space(i)^2))./(Ad*dL_dT.*pi*0.9*...
     detectivity_double*parameter.transmittance_optics);
plot1= figure(1);
txt1 = ['f/',num2str(f_number_space(i))];
plot(Te_dL_dT,NETD_space(i,:),'-diamond','DisplayName',txt1);
xlabel('Ground Temperature [K]','Fontsize',16);
ylabel('NETD space [K]','Fontsize',16);
title('NETD vs Ground temperature for different f-number');
grid on;
hold on;
legend;

% SNR = Power_ground*detectivity;
plot2= figure(2);
txt2 = ['f/',num2str(f_number_space(i))];
plot(Te_interval,Power_ground_double(i,:)*detectivity_double,'
    DisplayName',txt2)
xlabel('Ground Temperature [K]','Fontsize',16);
ylabel('SNR','Fontsize',16);
title('SNR vs Ground temperature for different f-number');
grid on;
hold on;
legend;

end

hold off

response_time = figure(3);
plot(GSD,ti);
```

```
yline(0.048,'-.','Response time Worst case');
yline(0.021,'-.','Response time Best case');
yline(0.036,'b-.','Response time VOx Bolometer');
yline(0.042,'b-.','Response time Bird 640');
xlabel('GSD [m]','Fontsize',16);
ylabel('Integration time [s]','Fontsize',16);
title('Integration time vs GSD');
grid on;
hold on;
```

Listing 2 – NETD space function.

```
function [detectivity_double,Power_ground_double] = NETD_space(
    constant,parameter,wav_initial,wav_end ...
     ,Te_interval,H,NETD_gr,GSD,f_number,f_number_space ...
     ,wav_initial_gr,wav_end_gr,Te_ground_netd,Ad,soil)
% This function computes the NETD for a infrared detector

% Constants
c=constant.c; %m/s Speed of light
k = constant.k; %J/K=m^2*kg*s^(-2)*K^(-1) Boltzmann's constant
h = constant.h; %J*s=kg*m^2/s Planck's constant
mu= constant.mu; %km^3/s^2 Gravitational parameter
R_earth=constant.R_earth; %km Earth radius
w_earth=constant.w_earth; %rad/s Angular velocity of the Earth

% Parameters
transmittance_optics = parameter.transmittance_optics;

% Maximum wavelength
sa_optics=pi/4*1/f_number_space^2; %sr
etendue=vpa(Ad*sa_optics); %sr*m^2
%% INTEGRATION TIME
% Orbital period
a=H+R_earth; %km
T0=2*pi*sqrt(a^3/mu); %s
% Spacecraft velocity
Vsat=(2*pi/T0-w_earth)*a; %km/s
% Integration time
ti=GSD/(1000*Vsat); %s
%% SIGNAL
% RADIANT FLUX FOR 1 PIXEL
% Ground
for index_Te=1:numel(Te_interval)
    Te=Te_interval(index_Te);
Power_ground(index_Te)=Integral_ground_emittance_W(Te,soil,
    wav_initial,wav_end)*etendue*transmittance_optics; %W
Power_ground_double(index_Te)= double(Power_ground(index_Te));
end

%% OBTAINING THE NETD
```

```
% Ground
syms L_s T wav
L_s = 2*h*c^2/(wav^5*(exp(h*c/(wav*k*T))-1)); %W/(sr*m^3)
%Differentiate with respect to the temperature
dLs_dT=diff(L_s,T); %W/(sr*m^3*K)
%Integrate with respect to the wavelength
dL_dT=int(dLs_dT,wav,wav_initial_gr,wav_end_gr); %W/(sr*m^2*K)
dL_dT=(subs(dL_dT,T,Te_ground_netd));
f_number_ground = f_number;
detectivity = vpa((4*(f_number_ground^2))/(Ad*dL_dT*pi*0.9*NETD_gr));
detectivity_double = double(detectivity);

end
```

Listing 3 – Function to differentiate particular ranges of wavelength.

```
function dL_dT=differentiate_L_respect_T_44_54(Te_dL_dT,soil)
% Defining the wavelength in meters for MWIR band
wav_initial=4.4e-6; %m
wav_end=4.8e-6; %m
% Constants
h = 6.62607004e-34;  %J*s=kg*m^2/s Planck's constant
c = 299792458; %m/s Speed of light
k = 1.38064852e-23;  %J/K=m^2*kg*s^(-2)*K^(-1) Boltzmann's constant
syms Te wav
% Atmospheric transmittance
TR=0.614;
% Emissivity of the Earth
% Obtain Ground emissivity for that soil
load Table_ground_emissivity_MWIR.txt
    GE=Table_ground_emissivity_MWIR(2,soil);
%% SOLUTION
% Obtain the spectral radiance emitted by Earth
Ls_earth=2*h*c^2/(wav^5*(exp(h*c/(wav*k*Te))-1)); %W/(sr*m^2*micron)
% Spectral radiance emitted by Earth throughout the atmosphere
Ls_out_earth=Ls_earth*GE*TR; %W/(sr*m^2*micron)
%Differentiate with respect to the temperature
dLs_dT=diff(Ls_out_earth,Te); %W/(sr*m^3*K)
dLs_dT=vpa(subs(dLs_dT,Te,Te_dL_dT));
%Integrate with respecto to the wavelength
dL_dT=int(dLs_dT,wav,wav_initial,wav_end); %W/(sr*m^2*K)
dL_dT=vpa(dL_dT);
dL_dT=double(dL_dT);
```

Listing 4 – Script to compare the sizes of the different detectors.

```
%% Presizing
clear all;
close all;
clear clc;
```

```
%% Parameters
wav_0=4.4; %[micrometer]
wav_max=4.8;       %[micrometer]
max_diameter=linspace(50,350,100); %[mm]
f_number=1.4;
Px = 10; %Pixel size [micrometer]
width = 1280; %[pixels]
H = 500; % Altitude [km]

for j=1:numel(f_number)
for i=1:numel(max_diameter)
%% Optics
max_aperture(i)=max_diameter(i)*0.75; %[mm]
EFL(i) = max_aperture(i)*f_number; %[mm]
max_length(i)=EFL(i)*1.3; %[mm]
estimated_room(i) = 400-max_length(i); %[mm]
diffraction_limit_down = 2*1.22*wav_0*f_number; %[micrometer]
diffraction_limit_up = 2*1.22*wav_max*f_number; %[micrometer]

if diffraction_limit_down(j) > Px
    flag_Ok(j) = false;
else
    flag_Ok(j) = true;
end

%% Field of view
tan_iFoV(i) = (Px/EFL(i))/1000;
iFoV(i) = rad2deg(atan(tan_iFoV(i))); %[deg]
tan_full_FoV(i) = tan_iFoV(i)*width;
full_FoV(i) = iFoV(i)*width;

%% GSD & Swath
GSD(i)= (H*Px)/EFL(i);
Swath(i) = GSD(i)*width;
end
end

plot1= figure(1);
plot(82,123.5,'-diamond','MarkerSize',10,'DisplayName','DAPHNIS');
hold on
plot(50,60,'-diamond','MarkerSize',10,'DisplayName','HiPIR');
plot(70,118,'-diamond','MarkerSize',10,'DisplayName','SUPERHAWK');
plot(61,68.58,'-diamond','MarkerSize',10,'DisplayName','HEXABLU');
plot(81,124,'-diamond','MarkerSize',10,'DisplayName','C615M');
plot(100,160,'-diamond','MarkerSize',10,'DisplayName','XCO_640_SERIES
    ');
plot(80,130,'-diamond','MarkerSize',10,'DisplayName','PELICAN_D-640')
    ;
plot(80,148.5,'-diamond','MarkerSize',10,'DisplayName','HERCULES_1280
    ');
```

```
plot(80,150,'-diamond','MarkerSize',10,'DisplayName','BLACKBIRD 1920');
plot(80,102.5,'-diamond','MarkerSize',10,'DisplayName','HOT PELICAN-D');
plot(61,74,'-diamond','MarkerSize',10,'DisplayName','HOT Neutrino');
plot(23,26,'-diamond','MarkerSize',10,'DisplayName','BIRD 640');
plot(31,31,'-diamond','MarkerSize',10,'DisplayName','VOx IMAGER BB');

xline(100,'r-.','1U');
yline(200,'r-.','2U');
yline(100,'r-.','1U');
xlabel('H [mm]','Fontsize',16);
ylabel('L [mm]','Fontsize',16);
xlim([0 150])
ylim([0 250])
grid on;
title('Size for each detector','Fontsize',16);
legend;

for i=1:numel(max_diameter)
 if 82-max_diameter(i) <0
     d_1(i) = abs(82-max_diameter(i));
 else
     d_1(i) = 0;
 end
 D_1(i)=82+d_1(i);
 if 70-max_diameter(i) <0
     d_2(i) = abs(70-max_diameter(i));
 else
     d_2(i) = 0;
 end
  D_2(i)=70+d_1(i);
 if 61-max_diameter(i) <0
     d_3(i) = abs(61-max_diameter(i));
 else
     d_3(i) = 0;
 end
  D_3(i)=61+d_3(i);
 if 81-max_diameter(i) <0
     d_4(i) = abs(81-max_diameter(i));
 else
     d_4(i) = 0;
 end
  D_4(i)=81+d_4(i);
 if 100-max_diameter(i) <0
     d_5(i) = abs(100-max_diameter(i));
 else
     d_5(i) = 0;
 end
   D_5(i)=100+d_5(i);
 if 80-max_diameter(i) <0
```

```
        d_6(i) = abs(80-max_diameter(i));
    else
        d_6(i) = 0;
    end
      D_6(i)=80+d_6(i);
    if 80-max_diameter(i) <0
        d_7(i) = abs(80-max_diameter(i));
    else
        d_7(i) = 0;
    end
    D_7(i)=80+d_7(i);
    if 80-max_diameter(i) <0
        d_8(i) = abs(80-max_diameter(i));
    else
        d_8(i) = 0;
    end
    D_8(i)=80+d_8(i);
    if 31-max_diameter(i) <0
        d_9(i) = abs(31-max_diameter(i));
    else
        d_9(i) = 0;
    end
    D_9(i)=31+d_9(i);
    if 50-max_diameter(i) <0
        d_10(i) = abs(50-max_diameter(i));
    else
        d_10(i) = 0;
    end
     D_10(i)=50+d_10(i);

    if 61-max_diameter(i) <0
        d_11(i) = abs(61-max_diameter(i));
    else
        d_11(i) = 0;
     end
     D_11(i)=61+d_11(i);

    if 23-max_diameter(i) <0
        d_12(i) = abs(23-max_diameter(i));
    else
        d_12(i) = 0;
     end
     D_12(i)=23+d_12(i);

       if 80-max_diameter(i) <0
        d_13(i) = abs(80-max_diameter(i));
    else
        d_13(i) = 0;
    end
    D_13(i)=80+d_13(i);
end
```

```
plot2= figure(2);
set(gcf,'DefaultAxesLineStyleOrder',{'-','--'});
plot(82+D_1,123.5+max_length,'MarkerSize',10,'DisplayName','DAPHNIS')
hold on
plot(50+D_10,60+max_length,'MarkerSize',10,'DisplayName','HiPIR');
plot(70+D_2,118+max_length,'MarkerSize',10,'DisplayName','SUPERHAWK')
    ;
plot(61+D_3,68.58+max_length,'MarkerSize',10,'DisplayName','HEXABLU')
    ;
plot(81+D_4,124+max_length,'MarkerSize',10,'DisplayName','C615M');
plot(100+D_5,160+max_length,'MarkerSize',10,'DisplayName','XCO_640_
    SERIES');
plot(80+D_6,130+max_length,'MarkerSize',10,'DisplayName','PELICAN_D
    -640');
plot(80+D_7,148.5+max_length,'MarkerSize',10,'DisplayName','HERCULES_
    1280');
plot(80+D_8,150+max_length,'MarkerSize',10,'DisplayName','BLACKBIRD_
    1920');
plot(80+D_13,102.5+max_length,'MarkerSize',10,'DisplayName','HOT_
    PELICAN-D');
plot(61+D_11,74+max_length,'MarkerSize',10,'DisplayName','HOT_
    Neutrino');
plot(23+D_9,26+max_length,'MarkerSize',10,'DisplayName','BIRD_640');
plot(31+D_9,31+max_length,'MarkerSize',10,'DisplayName','VOx_IMAGER_
    BB');

xline(200,'r-.','2U');
xline(300,'r-.','3U');
xline(100,'r-.','1U');
yline(100,'r-.','1U');
yline(200,'r-.','2U');
yline(300,'r-.','3U');
yline(400,'r-.','4U');
yline(500,'r-.','5U');
xlabel('H_[mm]','Fontsize',16);
ylabel('L_[mm]','Fontsize',16);
set(gca, 'YScale', 'log')
title('Size_for_each_detector_adding_up_the_optics_measures','
    Fontsize',16);
grid on;
xlim([0  500])
legend;

hold off
```

Listing 5 – Script to perform the pre-sizing parametric study.

```
%% Presizing parametric study
clear all;
close all;
```

```
clear clc;

%% Parameters
wav_0=4.4; %[micrometer]
wav_max=4.8;       %[micrometer]
max_diameter=linspace(50,350,100); %[mm]
f_number=linspace(1,2,6);
Px = 10; %Pixel size [micrometer]
width = 640; %[pixels]
H = 500; % Altitude [km]

for j=1:numel(f_number)
for i=1:numel(max_diameter)
%% Optics
max_aperture(i)=max_diameter(i)*0.75; %[mm]
EFL(i,j) = max_aperture(i)*f_number(j); %[mm]
max_length(i,j)=EFL(i,j)*1.3; %[mm]
estimated_room(i,j) = 400-max_length(i,j); %[mm]
diffraction_limit_down(j) = 2*1.22*wav_0*f_number(j); %[micrometer]
diffraction_limit_up(j) = 2*1.22*wav_max*f_number(j); %[micrometer]

if diffraction_limit_down(j) > Px
    flag_Ok(j) = false;
else
    flag_Ok(j) = true;
end

%% Field of view
tan_iFoV(i,j) = (Px/EFL(i,j))/1000;
iFoV(i,j) = rad2deg(atan(tan_iFoV(i,j))); %[deg]
tan_full_FoV(i,j) = tan_iFoV(i,j)*width;
full_FoV(i,j) = iFoV(i,j)*width;

%% GSD & Swath
GSD(i,j)= (H*Px)/EFL(i,j);
Swath(i,j) = (GSD(i,j)*width)/1000;
end
end

for i=1:numel(f_number)

plot1=figure(1);
txt1 = ['f/',num2str(f_number(i))];
plot(max_diameter,GSD(:,i),'DisplayName',txt1)
xlabel('Max diameter [mm]','Fontsize',16);
ylabel(' GSD [m]','Fontsize',16);
title('GSD vs Max diameter for different f-numbers');
grid on;
hold on;
legend;
```

```
plot2= figure(2);
txt2 = ['f/',num2str(f_number(i))];
plot(max_diameter,max_length(:,i),'DisplayName',txt2)
xlabel('Max diameter [mm]','Fontsize',16);
ylabel('Max length [mm]','Fontsize',16);
title('Max length vs Max diameter for different f-numbers');
grid on;
hold on;
legend;

plot3= figure(3);
txt3 = ['f/',num2str(f_number(i))];
plot(max_diameter,Swath(:,i),'DisplayName',txt2)
xlabel('Max diameter [mm]','Fontsize',16);
ylabel('Swath [km]','Fontsize',16);
title('Swath vs Max diameter for different f-numbers');
grid on;
hold on;
legend;

end

hold off
```

Listing 6 – Script to perform the power per pixel simulation.

```
%% Power per pixel
clear all;
close all;
clc;
%% Defining the wavelength for MWIR band
wav_initial=3e-6; %m
wav_end=5e-6; %m
wav_i_LWIR=8e-6; %m
wav_e_LWIR=12e-6; %m
wav=linspace(wav_initial,wav_end,20);
% wav=wav_initial:0.005e-6:wav_end; %m
%% EXTERNAL FLUXES %%
%%FLUX DUE TO THE EARTH AS A BLACK BODY
% Introduce the type of soil
    %evergreen forest=1
    %deciduous forest=2
    %mixed forest=3
    %closed shrubland=4
    %open shrubland=5
    %savanna=6
    %grassland=7
    %permanent wetland=8
    %cropland=9
    %natural mosaic=10
    %snow=11
```

```
    %barren=12
    %water=13
    %tundra=14
    %urban=15
soil=9;
% Define range of temperatures for the Earth
Te1=200; %K
Te2=1000; %K
Te=linspace(Te1,Te2,1000);
% Obtain the spectral radiance emitted by Earth

%% OPTICS
% Pixel size
Px=10e-6; %m
% Parameters earth-satellite
GSD=20;  %m
H=600000; %m
theta=atan(GSD/H);
% Calculating the optics
syms f D f_number
eqn1 = f_number == Px/(2.44*wav_end); %<
eqn2 = f == Px/tan(theta);
eqn3 = D == f/f_number;
sol = solve([eqn1, eqn2, eqn3], [f, D, f_number]);
f=vpa(sol.f);
D=vpa(sol.D);
f_number=vpa(sol.f_number);
%fprintf('D = %s;\n',D);
%fprintf('f = %s;\n',f);
%fprintf('f_number = %s;\n',f_number);
% Obtaining the etendue
f_number=1.4;
sa_optics=pi/4*1/f_number^2; %sr
etendue=vpa(Px^2*sa_optics); %sr*m^2
transmittance_optics=0.9;

for i=1:numel(Te)
% Ground
Power_ground(i)=Integral_ground_emittance_W_(Te(i),soil,wav_initial,
    wav_end)*etendue*transmittance_optics; %W
% Amount of power that reaches 1 pixel
Power_ground_LWIR(i)=Integral_ground_emittance_LWIR_W(Te(i),soil,
    wav_i_LWIR,wav_e_LWIR)*etendue*transmittance_optics; %W
end

%%Plot total power per 1 pixel
Total_Power_For_1_pixel = figure(1);
plot(Te,Power_ground,'y')
hold on
plot(Te,Power_ground_LWIR,'b')
  %  legend show
```

```
xlabel('Ground Temperature [K]');
ylabel('Power on each pixel [W]');
set(gca, 'YScale', 'log')
title('Power per pixel vs Ground Temperature');
grid on;
hold on;
legend('MWIR','LWIR')
```

References

[1] "Infrared". Wikipedia. Accessed: April 2021. [Online]. Available: https://en.wikipedia.org/wiki/Infrared

[2] A. Rogalski, *Infrared detectors and Terahertz Detectors*, 3rd ed. FL, USA: CRC Press, Taylor & Francis Group, 2019, ISBN: 978-1-4200-7671-4.

[3] Z. Jaki, *Micro and Nanophotonics for Semiconductor Infrared Detectors*, 1st ed. Cham: Springer International Publishing, 2014, ISBN: 978-3-319-09673-5 978-3-319-09674-2.

[4] D. T. Nguyen, "Design, modeling, and characterization of innovative terahertz detectors," Ph.D. dissertation, Université de Grenoble, France, 2012. [Online]. Available: https://tel.archives-ouvertes.fr/tel-00773019.

[5] A. Daniels, *Field guide to infrared systems*, detectors, and FPAs, 2nd ed. ser.SPIE Field guides. Bellingham , Wash: SPIE Press, 2010, ISBN: 978-0-8194-8080-4.

[6] F. Tint Garcia-Moreno, G. Fargant, F. Guerin, C. Israbian, J. C. Mathieu,J. Michaud, A. Bardoux, O. Hagolle, and J. P. Lagouarde, "MISTIGRI instrumental concept for high-resolution thermal infrared imaging," M. Strojnik, Ed., San Diego, CA, Aug. 2009, doi: 10.1117/12.825637.

[7] Y. Hang, "Time-Delay-Integration CMOS Image Sensor Design For Space Applications," Ph.D. dissertation, Nanyang Technological University, School of Electrical and Electronic Engineering. [Online]. Available: http://www.ntu.edu.sg/home/eechenss/Papers/Thesis-2016_Time-Delay-Integration%20CMOS%20Image%20Sensor%20Design%20For%20Space%20Applications.pdf.

[8] A. Dueñas Herrero, "Study of a CubeSat dual-band infrared imager for hydric stress observation from space." 2019, University of Liège.

[9] J. Vilaboa Pérez, "Multi-band Infrared Sensor For Earth Observation" 2019, University of Liège.

[10] S. Habraken, "Coherent and incoherent optics. Instrumental optics," Lectures from the University of Liège.

[11] "An introduction to CCD operation" Mullard Space Science Laboratory, Accessed: April 2021. [Online]. Available: http://www.mssl.ucl.ac.uk/www_detector/ccdgroup/optheory/ccdoperation.html

[12] McEwen, Alfred , Eliason, Eric , Bergstrom, James , Bridges, Nathan , Hansen, Candice , Delamere, William , Grant, John , Gulick, Virginia , Herkenhoff, K. , Keszthelyi, Laszlo , Kirk, Randolph , Mellon, Michael , Squyres, Steven , Thomas, Nicolas , Weitz, Catherine. "Mars Reconnaissance Orbiter's High Resolution Imaging Science Experiment (HiRISE)", 2007. Journal of Geophysical Research (Planets). 112. 5. doi: 10.1029/2005JE002605.

[13] Daneshgar, Saba. "Remote sensing observations for monitoring coastal zones, Volturno River mouth case study". 2015 doi: 10.13140/RG.2.1.3806.9209.

[14] A. Rogalski, M. Kopytko, and P. Martyniuk, *Antimonide-based Infrared Detectors: A New Perspective*, 1st ed. SPIE, Apr. 2018, ISBN: 978-1-5106-1140-5.

[15] "AeroCube-11R3". ESA Earth Observation Portal. Accessed: May 2021. [Online]. Available: https://directory.eoportal.org/web/eoportal/satellite-missions/a/aerocube-11r3#ops

[16] "Products". SCD Semi Conductor Devices. Accessed: May 2021. [Online]. Available: https://www.scd.co.il/products/

[17] "WIDEST RANGE OF ADVANCED INFRARED DETECTORS". Lynred by Sofradir & Ulis. Accessed: May 2021. [Online]. Available: https://www.lynred.com/products

[18] "AIM Products for Space Application". AIM. Accessed: May 2021. [Online]. Available: https://www.aim-ir.com/en/applications-products/space.html

[19] "SuperHawk". Leonardo. Accessed: May 2021. [Online]. Available: https://www.leonardocompany.com/en/products/superhawk

[20] "INFRARED CAMERA MODULES & DETECTORS". Leonardo DRS. Accessed: May 2021. [Online]. Available: https://www.leonardodrs.com/commercial-infrared/products/

[21] "Products". GST Global Sensor Technology. Accessed: May 2021. [Online]. Available: http://gsten.gst-ir.com/product/index/mid/3.html

[22] "Mid-wave Infrared Imagers". Xenics Infrared Solutions. Accessed: May 2021. [Online]. Available: https://www.xenics.com/mid-wave-infrared-imagers/

[23] "Neutrino SWaP+C Series". Teledyne FLIR. Accessed: May 2021. [Online]. Available: https://www.flir.com/products/neutrino-swapc-series/

[24] "IR Transmission Spectra". Gemini Observatory. Accessed: May 2021. [Online]. Available: https://www.gemini.edu/observing/telescopes-and-sites/sites#Transmission.

[25] J. R. Howell, M. P. Menguc, and R. Siegel, *Thermal radiation heat transfer*, 6th ed. FL, USA: CRC Press, Taylor & Francis Group, 2015, ISBN: 978-1-4665-9326-8.

[26] K. N. Tiwari, C. Chatterjee "Lesson 14 Microwave Remote Sensing". Dept. of Agricultural and Food Engg., IIT, Kharagpur. Accessed: May 2021. [Online]. Available: http://ecoursesonline.iasri.res.in/mod/page/view.php?id=2067.

[27] "Earth Fact Sheet". NASA Goddard Space Flight Center. Accessed: May 2021. [Online]. Available: https://nssdc.gsfc.nasa.gov/planetary/factsheet/ earthfact.html.

[28] "Sun Fact Sheet". NASA Goddard Space Flight Center. Accessed: May 2021. [Online]. Available: https://nssdc.gsfc.nasa.gov/planetary/factsheet/ sunfact.html.

[29] M. Vollmer and K.-P. Möllmann, *Infrared thermal imaging: fundamentals, research and applications*, 2n ed. NJ, USA: John Wiley & Sons, 2017, ISBN: 978-3-5276-9329-0.

[30] S. D. Lord "A new software tool for computing Earth's atmospheric transmission of near- and far-infrared radiation". NASA Ames Research Center Moffett Field, 1992. Accessed: May 2021. [Online]. Available: https://nssdc.gsfc.nasa.gov/planetary/factsheet/ earthfact.html.

[31] A.M. Baldridge, S.J. Hook, C.I. Grove, G. Rivera, "The ASTER spectral library version 2.0",Remote Sensing of Environment,Volume 113, Issue 4,2009,Pages 711-715,ISSN 0034-4257, https://doi.org/10.1016/j.rse.2008.11.007.

[32] D. Grodent, "Atmosphere of the Earth and Space Environment" Lectures from the University of Liège.

[33] A. Bulis, "The Atmosphere: Getting a Handle on Carbon Dioxide" NASA's Jet Propulsion Laboratory.[Online]. Available: https://climate.nasa.gov/news/2915/the-atmosphere-getting-a-handle-on-carbon-dioxide/.

[34] P. Austin"Solid angle and radiance". Department of Earth, Ocean and Atmospheric Sciences, University of British Columbia. Accessed: May 2021. [Online]. Available: https://clouds.eos.ubc.ca/∼phil/courses/atsc301/sensors.html.

[35] "Climate Data CERES: IGBP LAND CLASSIFICATION". NATIONAL CENTER FOR ATMOSPHERIC RESEARCH . Accessed: May 2021. [Online]. Available: https://climatedataguide.ucar.edu/climate-data/ceres-igbp-land-classification.

[36] S. Shah, T. Grübler, L. Krempel, S. Ernst, F. Mauracher, s. Contractor. "Real-Time Wildfire Detection from Space – A Trade-Off Between Sensor Quality, Physical Limitations and Payload Size". ISPRS - International Archives of the Photogrammetry, Remote Sensing and Spatial Information Sciences.2019 XLII-2/W16. 209-213. 10.5194/isprs-archives-XLII-2-W16-209-2019.

[37] C. Horch, N. Schnelle, M. Gulde, E. Watson, M. Schimmerohn, F. Schäfer. "An MWIR payload with FPGA-based data processing for a 12U nanosatellite". 2017.

[38] "QB50". E-USOC, Spanish User Support and Operations Centre . Accessed: May 2021. [Online]. Available: https://www.eusoc.upm.es/qb50/.

[39] "QBITO, el primer CubeSat de la UPM, camino de la Estación Espacial Internacional". UNIVERSIDAD POLITÉCNICA DE MADRID . Accessed: May 2021. [Online]. Available: https://www.upm.es/?id=f20e2a058bafa510VgnVCM10000009c7648a____&prefmt=articulo&fmt=detail.

[40] "Arkyd-6". ESA Earth Observation Portal. Accessed: May 2021. [Online]. Available: https://directory.eoportal.org/web/eoportal/satellite-missions/a/arkyd-6.

[41] "LunIR (SkyFire)". Gunter's Space Page. Accessed: May 2021. [Online]. Available: https://space.skyrocket.de/doc_sdat/lunir.htm.

[42] "Nanosatellites DataBase". NanoSats DataBase. Accessed: May 2021. [Online]. Available: http://www.trbimg.com/img-57aa16be/turbine/os-nasa-lockheed-martin-cubesat-20160809.

[43] T. Pagano. "CubeSat infrared atmospheric sounder (CIRAS) NASA InVEST technology demonstration".(2017). 101770K. 10.1117/12.2266282.

[44] "SpaceTech Event June 2019 - ESTEC". ISIS Space - Innovative Solutions In Space. Accessed: May 2021. [Online]. Available: https://www.tugraz.at/fileadmin/user_upload/tugrazInternal/Studium/Studienangebot/Universitaere_Weiterbildung/SpaceTech/Jeroen-Rotteveel-ISIS-Innovative-Solutions-in-Space.pdf.